Fall 2022

Histomechanical Compatibility of Coronary Artery Bypass Grafts

Colton J. Kostelnik

HISTOMECHANICAL COMPATIBILITY OF CORONARY ARTERY BYPASS GRAFTS

by

Colton J. Kostelnik

Bachelor of Science
University of South Carolina, 2018

Submitted in Partial Fulfillment of the Requirements

For the Degree of Doctor of Philosophy in

Biomedical Engineering

College of Engineering and Computing

University of South Carolina

2022

Accepted by:

John F. Eberth, Major Professor

Wayne Carver, Committee Member

Tarek Shazly, Committee Member

Cameron G. McCarthy, Committee Member

Cheryl L. Addy, Interim Vice Provost and Dean of the Graduate School

DEDICATION

I would like to dedicate this work to my father, Kevin, my mother, Lori, and my sister, Sam, whose continued support has helped me remain persistent in my pursuits throughout both my undergraduate and graduate degrees at UofSC. Without their guidance and unconditional support, I might have never accomplished my academic and research goals.

ACKNOWLEDGMENTS

First of all, I would like to acknowledge my advisor, Dr. John F. Eberth, for his steadfast guidance and constant support throughout my studies. Since the start of my graduate career, he has helped me grow from a student into a strong, independent researcher. I would also like to acknowledge my committee members – Dr. Wayne Carver, Dr. Tarek Shazly, and Dr. Cameron G. McCarthy – who have all been a knowledgeable and reliable resource throughout the execution of my research objectives. They have all supported my efforts and offered insightful perspectives during our discussions. Additionally, I would like to thank Dr. Susan Lessner for allowing me to use her Bose BioDynamic device and epifluorescence microscope, which my research findings were contingent upon. Next, I would like to thank my friends and colleagues Brittany Watson, Candice Cheung, Brooks Lane, Nazli Gharraee, Liya Du, and Breanna Pederson for their comradery and advice that inspired me through the hardships of graduate school. Lastly, I would like to thank all of the faculty and staff of the Biomedical Engineering Program, Cell Biology and Anatomy Department at the School of Medicine, and the Instrumentation Resource Facility for their active training and supporting roles throughout my graduate research initiatives.

ABSTRACT

Coronary artery disease is a localized form of atherosclerosis that can severely restrict blood flow to the heart often requiring a surgical intervention known as coronary artery bypass grafting (CABG) to reestablish perfusion to this essential circulation. To some extent, the selection of the autograft tissue is at the surgeon's discretion with factors such as stenosis location and the existing tissue's pathological state contributing to a choice that could be deterministic in surgical outcomes. Many post-operative complications and premature graft failures originate from graft-target tissue incompatibilities and altered blood flow patterns. We hypothesize that mechanical mismatching between the graft material and the host tissue contributes to the loss of patency following CABG - even when using internal thoracic arteries (ITA), the clinical benchmark for autologous bypass grafting. To that end we have quantified the spatially heterogeneous mechanical properties of left (L) and right (R) ITAs using a porcine surrogate for the human vasculature. Biaxial mechanical testing revealed significantly larger circumferential stresses and lumen area compliances in the proximal region of LITAs, while the distal region of RITAs exhibited significantly larger axial stresses. In addition, we captured significant histological differences in the elastin-collagen aspect ratio throughout both arteries. The relative amounts of these load-bearing constituents are known to influence the local mechanical behavior and therefore our histological observations support the captured biaxial mechanical data. We then performed a similar tissue characterization study to quantify the properties of four distinct coronary arteries that are common targets for CABG procedures.

Our findings indicate that these blood vessels are classified as muscular arteries, and they possess distinctly different histological features and a unique mechanical behavior.

Patients that require secondary CABG surgery do not always have suitable autologous vessels available to serve as grafts. Decellularized vascular grafts (DCVGs) have emerged as a functional alternative to autologous bypass grafting. Despite the inherent advantage of removing immunogenic materials to mitigate host rejection, thrombosis, restenosis, and aneurysm formation limit the widespread usage of DCVGs. However, surgical dependence on autologous grafts presents a need for the effective preservation of unused or excised graft vessels that can be implanted in CABG surgeries. Likewise, cryopreservation techniques have been developed to circumvent unwanted biological and physical consequences through controlled media exchange and regulated freezing conditions. These techniques can be modified to aid in the development of graft tissue banks that can be used to alleviate graft shortages. However, the consequences of decellularization and cryopreservation techniques on elastomuscular artery mechanical properties and microarchitecture warrant further investigation since extracellular matrix proteins and water content contribute to the gross properties of all soft-biological tissues.

Thus, this dissertation offers quantified data of the distinctly different histomechanical metrics that exist along the length of the superior CABG candidate, the ITA. Our finite element models of the end-to-end anastomoses reveal that these different regions produce varying hemodynamic and solid mechanical stress magnitudes. These findings offer predictions of mechanobiological complications and grafting outcomes, thereby contributing fundamental evidence to the fields of experimental and computational vascular biomechanics. Lastly, the work presented in this dissertation provides quantified

evidence of different decellularization and cryopreservation methods that minimize biochemical and biomechanical consequences. Overall, these findings contribute to the fields of tissue engineering and vascular mechanics by exploring strategies and techniques that produce optimal decellularization or cryopreservation outcomes.

TABLE OF CONTENTS

DEDICATION iii

ACKNOWLEDGMENTS iv

ABSTRACT v

TABLE OF CONTENTS viii

LIST OF TABLES ix

LIST OF FIGURES x

CHAPTER 1: INTRODUCTION – CABG HISTOMECHANICS 1

CHAPTER 2: LONGITUDINAL HISTOMECHANICAL HETEROGENEITY OF THE INTERNAL THORACIC ARTERY 15

CHAPTER 3: THE ACUTE MECHANICAL CONSEQUENCES OF SEGMENT-SPECIFIC CORONARY ARTERY BYPASS 47

CHAPTER 4: SMALL-DIAMETER ARTERY DECELLULARIZATION: EFFECTS OF ANIONIC DETERGENT CONCENTRATION AND TREATMENT DURATION ON PORCINE INTERNAL THORACIC ARTERIES 76

CHAPTER 5: COMPARISON OF ELASTOMUSCULAR ARTERY CRYOPRESERVATION STRATEGIES 108

CHAPTER 6: CONCLUSIONS 130

REFERENCES 134

APPENDIX A: JOURNAL PERMISSION FOR USE OF MANUSCRIPT 157

LIST OF TABLES

Table 2.1 - Segment selection of left and right internal thoracic arteries 35

Table 2.2 - Vessel geometry in the unloaded configuration 35

Table 2.3 - HGO model material parameters of the averaged data for segment-specific left and right internal thoracic arteries..... 36

Table 3.1 - HGO model material parameters for specific coronary arteries..... 65

Table 3.2 - Vessel geometry of the unloaded configurations 65

Table 3.3 - Summary of peak simulation outputs from the solid-fluid models of all anastomosis configurations. Maximum values in each group are highlighted in red and minimum values for each group are highlighted in blue. The gray box indicates a computational model that did not converge..... 66

Table 3.4 - Results of the normalized objective function for all anastomosis combinations. Solid-fluid simulation outputs were normalized to basal coronary mechanical and fluid dynamic values and averaged. For each coronary artery, the anastomosis configuration that resulted in the most significant deviation is shown in red, while the smallest is shown in blue..... 67

LIST OF FIGURES

Figure 1.1 - End-to-end sham anastomosis of a female porcine ITA sample secured using nonpenetrating vascular clips and mounted within a culture chamber. 12

Figure 1.2- Parallel *ex vivo* pulsatile perfusion bioreactors assembled within an incubator. Inlet and outlet pressure gauges sandwich the culture chambers that house the arteries. The outlet tubing passes a clamp which provides the downstream resistance to pressurize the arteries. The outlet tubing leads to a media reservoir, and then the tubing leads out of the incubator and connects to a Masterflex L/S digital drive connected to four Masterflex Easy Load pump heads equipped with four stainless steel rollers to provide physiological pulsatile flow of media (not pictured). 13

Figure 1.2- Immunohistochemistry images of [A] control and [B] anastomosed ITAs after being cultured under pulsatile conditions for 24 hours. These cross-sections show nuclei (blue), elastin (green), and vWF (red), while the white bracket indicates neointimal thickening. 14

Figure 2.1- Full length porcine left (LITA) and right (RITA) internal thoracic arteries with sections labeled that approximate the (1) Proximal, (2) Submuscularis, (3) Middle, (4) Distal. All segments were taken from the same relative distance from the subclavian artery and distal bifurcation. 37

Figure 2.2 - Movat's Pentachrome stain of LITA [A-D] and RITA [E-H] comparing the vascular wall composition across the proximal [A & E], submuscular [B & F], middle [C & G], and distal [D & H] segments. 38

Figure 2.3 - Constituent area fraction of collagen, elastin, smooth muscle cells (SMCs), and glycosaminoglycans (GAGs) determined by thresholding Movat's Pentachrome stained cross-sections for the four anatomical locations along the LITA and RITA. Statistical significance is denoted as (*) when $p<0.05$, (**) at $p<0.01$, and (***) at $p<0.001$. Mean ± SD, n=5 for each group. 39

Figure 2.4 - Morphometric analysis of ITA wall composition. Intima, media, and adventitia thicknesses measured from Movat's Pentachrome stained cross-sections and normalized to relative ITA complete wall

thickness. Statistical significance is denoted as (*) when $p<0.05$, (**) at $p<0.01$, and (***) at $p<0.001$. Mean ± SD, n=6 for each group. 40

Figure 2.5 - Propidium Iodide nucleic acid stain and elastin autofluorescence LITA [A-D] and RITA [E-H] comparing the medial smooth muscle cell count and elastic lamellar count of the proximal [A & E], submuscular [B & F], middle [C & G], and distal [D & H] segments. 41

Figure 2.6 - [A] Medial smooth muscle cell density and [B] elastic lamellae count measured from the propidium iodide and elastin autofluorescence cross-sections along the LITA and RITA. Statistical significance is denoted as (*) when $p<0.05$, (**) at $p<0.01$, and (***) at $p<0.001$. Mean ± SD, n=3 for each group. 42

Figure 2.7 - Biaxial mechanical data for LITA [A, C, E, G] and RITA [B, D, F, H]. Pressure-outer diameter [A & B], axial force-pressure [C & D], circumferential stress-stretch [E & F] were all plotted at $\lambda_z = 1.55$. All vessels were tested at axial stretch ratios above and below the one shown but these data were omitted for clarity. 43

Figure 2.8 - Biaxial mechanical data of LITA [A, C, E, G] and RITA [B, D, F, H] plotted at common loading conditions of 100 mmHg and $\lambda_z = 1.55$. Inner radius [A & B], circumferential stress [C & D], axial stress [E & F], and area compliance [G & H] were plotted at the four anatomical segments for each vessel. Statistical significance is denoted as (*) when $p<0.05$, (**) at $p<0.01$, and (***) at $p<0.001$. Statistical significance between the LITA and RITA segments is denoted as (#) at $p<0.05$. Mean ± SD, n=6 for each group. 44

Figure 2.9 - Results of the best fit parameters using the 4-fiber family HGO model (solid lines) to average (n=5-6) experimental pressure-force data (symbols) for the LITA [top] and RITA [bottom] at the three axial stretch ratios. The proximal, submuscularis, middle, and distal segments are shown [left-to-right]. 45

Figure 2.10 - Average strain energy contours (kPa) for the LITA [top] and RITA [bottom] proximal, submuscularis, middle, and distal segments [left-to-right]. Open circles represent approximate *in vivo* values of strain energy at 100 mmHg. Statistical significance is indicated by (*) when found between a given segment and its proximal section, (‡) when found between sequential segments, and (#) when found between the corresponding left and right segments. 46

Figure 3.1 - Porcine heart from the anterior and superior view with distinct structures labeled to discern relative sizes and locations of the four coronary arteries of interest. PLAD- proximal left anterior descending artery; DLAD- distal left anterior descending artery; LCX- left

circumflex artery; RCA- right coronary artery; RA- right atrium; LA- left atrium; PV- pulmonary vein 68

Figure 3.2 - Biaxial mechanical data of the four porcine coronary arteries. The leftmost plots are pressure 69

Figure 3.3 - Biaxial mechanical data of porcine coronary arteries and the third LITA segment plotted at common loading conditions of 100 mmHg and at the force-invariant stretch. [A] Inner radius, [B] area compliance, [C] circumferential stress, [D] axial stress. Statistical significance between different coronary arteries is indicated by (**) and (***) at $p<0.01$ and $p<0.001$, respectively. Statistical significance between a coronary artery and LITA is indicated by (#) at $p<0.05$. Mean ± SD, n=4 for each group..... 70

Figure 3.5 - Picrosirius Red stained cross-sections imaged through polarized light microscopy. [A] PLAD, [B] DLAD, [C] RCA, [D] LCX, and [E] the third LITA segment. [F] Quantified area fractions medial and adventitial collagen birefringence. Statistical significance between the adventitial collagen of a coronary vessel and LITA is denoted as (#) at $p<0.05$. Mean ± SD, n=5 for each vessel..... 72

Figure 3.6 - Computational analysis of PLAD-$LITA_3$ end-to-end anastomosis. [A] Colorimetric illustration of first principal stress (σ_1) after inflation from 0 mmHg to 100 mmHg. [B] Colorimetric illustration of fluid shear stress (τ_w) at the inflated configuration. Red arrows depict the contact region representing the anastomosis..... 73

Figure 3.7 - Plots of the first principal stress (σ_1) along the anastomosis for all coronary artery and ITA combinations. The vertical line represents the anastomosis between the two vessels, while the left region of the plot represents the ITA-end, and the right region represents the coronary-end..... 74

Figure 3.8 - Plots of the maximum fluid shear stress (τ_w) along the anastomosis for all coronary-ITA combinations. The vertical line represents the anastomosis, while the left region of the plot represents the ITA-end, and the right region represents the coronary-end 75

Figure 4.1 - DAPI nuclear stain and quantification of DNA content following [A] 24 hours and [B] 72 hours of anionic detergent treatment. The insets are representative images of DAPI-stained sections of control, 6% detergent-treated, and 1% detergent-treated tissues at respective time points. Area fraction quantification of DAPI positive pixels for [C] 24 hours and [D] 72 hours. Quantified DNA concentrations from the PicoGreen assays for [E] 24 hours and [F] 72 hours. Statistical significance between detergent concentrations relative to untreated

controls was determined by one-way ANOVA and is indicated by (*) at $p<0.05$. Mean ± SD, n=4 for each group 98

Figure 4.2 - Western blot analysis of representative cytoplasmic (α-smooth muscle actin), cell surface (β1 integrin), and basement membrane (laminin) proteins. Representative images of western blots illustrating the effects of anionic detergent concentration and treatment duration. Lanes 1 – 6 are untreated control, 0% detergent, 1% detergent, 2% detergent, 3% detergent and 6% detergent, respectively 99

Figure 4.3 - Representative scanning electron microscopic images of the [A, C] 72-hour control sample at low and high power [B, D] 1% detergent for 72 hours at low and high power. Quantification of the total porosity in tissues after [E] 24 hours and [F] 72 hours for all anionic detergents was performed on high-powered images. Statistical significance between detergent concentrations relative to untreated controls was determined by one-way ANOVA and is indicated by (*) at $p<0.05$. Mean ± SD, n=3 for each group..... 100

Figure 4.4 - Quantification of hydroxyproline concentrations after [A] 24 hours and [B] 72 hours of anionic detergent treatment. Collagen percent volume quantified by image thresholding of picrosirius red-stained tissue sections after treatment of [C] 24 hours and [D] 72 hours. No statistically significant differences were found following ANOVA analysis. Mean ± SD, n=5 for each group 101

Figure 4.5 - Quantitative analysis of elastic fibers following anionic detergent treatment. Representative microscopic images of control samples, 6% detergent, and 1% detergent for [A] 24 hours and [B] 72 hours, respectively. Elastic fiber area fraction was quantified from Verhoeff-Van Gieson-stained tissue following anionic detergent treatment for [C] 24 hours and [D] 72 hours. No statistically significant differences were found following ANOVA analysis. Mean ± SD, n=5 for each group 102

Figure 4.6 - Analysis of dimethylmethylene blue (DMMB) concentrations of all anionic detergent concentrations following [A] 24 and [B] 72 hours of treatment. DMMB concentration was indicative of the glycosaminoglycan concentration present in all tissue samples. Statistical significance between detergent concentrations relative to untreated controls was determined by one-way ANOVA and is indicated by (*) at $p<0.05$. Mean ± SD, n=5 for each group 103

Figure 4.7 - Biaxial mechanical data for all decellularization groups and fresh porcine ITA tissue. [A] Pressure-outer diameter, [B] axial force-pressure, [C] circumferential stress-stretch all plotted at $\lambda_z = 1.45$. [D] Axial stress-stretch at 100 mmHg. Mean ± SEM, n=4 for each group..... 104

Figure 4.8 - Biaxial mechanical data of decellularized porcine ITAs plotted at common loading conditions of 100 mmHg and λ_z = 1.45. [A] Inner radius, [B] thickness, [C] circumferential stress, [D] axial stress, [E] circumferential stretch, and [F] area compliance. Statistical significance between different decellularized treatments is indicated by (*) at $p<0.05$. Statistical significance between a decellularized ITA group and the control or fresh tissue is indicated by (#) and (**), respectively. Mean ± SD, n=4 for each group 105

Figure 4.9 - Unloaded conditions of decellularized and fresh porcine ITAs. [A] Average unloaded wall thickness and [B] opening angle. Statistical significance between a decellularized ITA group and the fresh tissue group is indicated by (**) at $p<0.05$. Mean ± SD, n=4 for each group 106

Supplemental Figure 4.10 - Quantified PicoGreen DNA concentrations for [A] 24-hour and (B) 72-hour samples treated with DNAse (+DNase) before or after detergents or when DNase was omitted from the protocol (-DNase). Statistical significance given by (*, **,***) at $p<0.05$, $p<0.01$, and $p<0.001$ respectively. Mean ± STD, n=8-12. 107

Figure 5.1 - Biaxial mechanical data for all fresh and groups of porcine ITA tissue. [A] Pressure-inner radii, [B] axial force-pressure, [C] circumferential stress-stretch all plotted at the force-invariant axial stretch and 100 mmHg. [D] Axial stress-stretch at 100 mmHg. Mean ± SEM, n=5 for each group. 123

Figure 5.2 - Biaxial mechanical data of porcine ITAs frozen with or without cryoprotection at different freezing rates plotted at common loading conditions of 100 mmHg and the force-invariant axial stretch. [A] Inner radius, [B] loaded thickness, [C] circumferential stress, [D] axial stress, [E] area compliance, and [F] ring sector opening angle. Mean ± SD, n=5 for each group. 124

Figure 5.3 – Plots of the difference between the final and initial experimental trials of [A] circumferential and [B] axial stresses between at common loading of 100 mmHg and force-invariant axial stretch for all fresh and frozen groups Statistical significance between a frozen ITA group and the fresh tissue group is indicated by (* and ***) at $p<0.05$ and $p<0.001$, respectively. Mean ± SD, n=5 for each group. 125

Figure 5.4 - Scanning electron microscopy images of [A] fresh, [E] 24 hours at 4°C control, [B-D] cryoprotected, and [F-H] non-cryoprotected ITA cross-sections. Cross-sectional images grouped by freezing rates illustrate [B] & [F] slow frozen ITAs held at -20°C, [C] & [G] controlled frozen ITAs held at -196°C, and [D] & [H] flash frozen ITAs held at -196°C. Tears within the vascular wall from ice crystal damage are indicated by red arrows. 126

Figure 5.5 –MTT colorimetric metabolic activity representative images of [A] fresh, [E] 24 hours at 4°C control, [B-D] cryoprotected, and [F-H] non-cryoprotected ITA cross-sections. Cross-sectional images grouped by freezing rates illustrate [B] & [F] slow frozen ITAs held at -20°C, [C] & [G] controlled frozen ITAs held at -196°C, and [D] & [H] flash frozen ITAs held at -196°C. Purple hues are indicative of metabolically active tissue. 127

Figure 5.6 - Biaxial mechanical data plotted at common loading conditions of 100 mmHg and the force-invariant axial stretch for fresh control ITAs, 24 hours at 4°C control ITAs, and ITAs frozen with or without cryoprotection at a controlled freezing rate and held for over 6 months. [A] Inner radius, [B] loaded thickness, [C] circumferential stress, [D] axial stress, [E] area compliance, and [F] ring sector opening angle. Mean ± SD, n=5 for each group..... 128

Figure 5.7 – Representative images of the MTT assay and SEM of [A] &[C] non-cryoprotected and [B] &[D] cryoprotected porcine ITAs frozen at -1°C/min and held at -196°C for over 6 months. 129

Figure A.1 – Permission from Journal of Mechanical Behavior of Biomedical Materials to include published manuscript in this dissertation (Chapter 2). 157

Figure A.2 – Permission from Journal of Biomedical Materials Research Part B: Applied Biomaterials to include published manuscript in this dissertation (Chapter 4). 158

CHAPTER 1

INTRODUCTION – CABG HISTOMECHANICS

1.1 CORONARY ARTERY BYPASS SURGERY

Coronary artery disease (CAD) is characterized by the incidence of atherosclerosis within the vascular network of the heart, which restricts the flow of oxygenated blood to the myocardium and can result in morbidity and mortality. The most effective surgical intervention for late stage CAD is the implantation of a vascular graft(s) to restore myocardial perfusion beyond the stenosis [1, 2]. Advancements in medical equipment and development of clinical guidelines for these coronary artery bypass grafts (CABGs) has helped decrease the total number of inpatient discharges from 683,000 to 371,000 within the United States of America between 1997 and 2014 [2–4]. Even though these advancements have helped mitigate CAD prevalence, it is known that patients still have an elevated risk of recurrence.

1.2 ARTERIAL HISTOMECHANICS

1.2.1 Coronary Vasculature

The left and right coronary arteries (CoAs) originate in the aortic root just distal to the aortic valve before branching into progressively smaller vessels that supply blood flow to different regions of the heart. The larger coronary vessels lie in the epicardium with smaller branches penetrating the myocardium. With the high metabolic demand of the heart requiring a constant supply of oxygen and nutrients, occlusion of the larger coronary

arteries require surgical intervention. The most common sites for CABG include the proximal and distal left anterior descending (PLAD & DLAD), right coronary (RCA), and left circumflex (LCX) arteries. Amongst all CoAs, the left anterior descending (LAD) exhibits the highest incidence of CAD [5, 6]. This artery is most the frequently targeted CoA for CABG revascularization because carries almost 50% of blood within the coronary vasculature and supplies oxygenated blood to the anterior interventricular septum [7]. This artery is highly branched and the formation of stenoses are often found near the apex of the heart [7].

In general, the media of arteries is often composed of concentric layers of smooth muscle cells (SMCs), elastin lamellar units, and collagen fibrils that are all important for responding to normal mechanical loading (i.e., intraluminal pressure and fluid shear stress) [8]. The CoAs are considered muscular arteries because they contain a majority of smooth muscle with dispersed elastin lamellar units [8, 9]. However, histological findings have shown that the CoAs exhibit elastomuscular characteristics with the total amount of elastin decreasing as the distance from the aortic branch increases [10]. Other tissue characterization studies have shown that most CoAs possess a large amount of loosely packed adventitial collagen to help resist the compressive and pulsatile forces of the heart [11]. The mechanical properties of these arteries have been widely investigated, but comprehensive data of the biaxial loading and histological composition of the CoAs is needed to provide a complete view of their innate material parameters [8, 12].

1.2.2 Autograft Considerations

The choice of conduit is a key surgical parameter that can influence the short and long-term patency of a bypass graft. Invariably, the use of autologous tissue sources

(autografts) is preferred over synthetic grafts for CABG surgeries [10, 13–15]. The implantation of these autografts is dependent upon the location and number of stenoses and the availability of patent graft tissue. The modern CABG procedure dates back to 1968 when Dr. George Green from Saint Luke's Hospital successfully performed the first left internal thoracic (also known as internal mammary) artery (ITA) to LAD anastomosis [16]. Since then, long-term clinical observations of graft patency have revealed the differential performances of the autograft candidates and identified that the superior choice remains to be the left ITA [3, 6, 17, 18]. The ITA has been shown to successfully revascularize the two main coronary arteries and their subdivisions with an overall first-year patency rate of ~96% and a ten-year patency rate of ~90% [3, 15, 18, 19]. The other common autograft candidates such as the radial artery (RA) and great saphenous vein (GSV) exhibit 92%:89% and 81%:60% patency rates, respectively [18–20]. Regarding surgical considerations, the ITA is the most frequently implanted autograft because of its available length, proximity to the anterior coronary vasculature allowing for revascularization with a single anastomosis, and its innate atheroprotective properties.

Small diameter arteries (<6mm in humans) such as the ITA and RA possess unique amounts of cellular and extracellular structures that form depending on the perivascular environment, relative distance from the heart, local hemodynamic conditions, and global physiological role [21–23]. The unique microstructural composition of blood vessels influences their distinct mechanical behavior, and the ratio between key load-bearing constituents within the vascular wall warrants further consideration when selecting a proper autograft. Elastin, for example, is a critical structural constituent responsible for enabling large deformations in vessels near the heart in response to pulsatile pressure. Elastin and

its supporting microfibrillar network, engages at low strains and exhibits an isotropic response to loading. The unique cross-links within this protein provides an intrinsic ability to stretch up to 150% of its original length [24]. Collagen is the key load-bearing constituent at high strains and endows blood vessels with a rigid ECM protein network that protects from blood pressure-induced overexpansion. The SMCs maintain local hemodynamic conditions and peripheral resistance by regulating the inner diameter via contraction/relaxation. For CABG surgeries, an autograft with a large amount of smooth muscle should be avoided due to the high degree contractility and vasospastic characteristics diminishing the postoperative patency [25–27]. Another important vascular wall constituent that plays a role in local wall mechanics is glycosaminoglycans (GAGs). These are hydrophilic molecules that retain water and contribute to the viscous mechanical response [28]. The aspect ratio between all of these load-bearing constituents can substantially influence the gross mechanical behavior of arteries, and should be considered when selecting a CABG [27, 29]. Theoretically, an autograft should possess a similar aspect ratio to that of the target tissue to minimize material and mechanical discrepancies. The ITA exhibits a histoarchitecture and local mechanical behavior similar to that of CoAs, and therefore, is considered the best autograft choice in terms of these qualities [10, 15]. However, it should be noted that graft failure develops from a myriad of physical and biological factors.

1.3 GRAFT FAILURE

Investigations into the long-term patency of ITA and GSV grafts have determined that if a graft is patent at 1 week after surgery then there is a 88% and 68% likelihood of the graft remaining patent at 10 years, respectively [18, 19]. When extrapolated to 25

postoperative years, the need for surgical reintervention increases to nearly ~50% of patients [30, 31]. The likelihood of reintervention varies based on patient characteristics, but operative factors such as conduit choice, suture material, and anastomotic closure technique also present risks that may lead to early reintervention [4, 31, 32].

A variety of biological, mechanical, geometric, and fluidic consequences contribute to CABG failure and are likely to arise along the anastomotic interface, where the graft and target arteries are surgically attached [33]. Figure 1.1 shows an example of an idealized end-to-end anastomosis using vascular clips. Early graft failure is linked to endothelial dysfunction, commonly found near sites of hemodynamic flow disturbances, or surgically-induced endothelial damage, which initiates prothrombotic and proinflammatory pathways and leads to neointimal formation. For example, porcine ITAs that we cultured under pulsatile conditions for 24 hours in a custom-built bioreactor (Figure 1.2) revealed neointimal thickening at the anastomotic interface in comparison to the control (Figure 1.3). Significant changes to the mRNA expression levels of remodeling genes (i.e., SERPINE1, TGFB1, COL3A1) were found in the ITA after 6 hours of pulsatile perfusion [34]. Note that these studies were performed *in vitro*, thus irrespective of a systemic immune response. Late graft failure has been linked to atherosclerotic plaque formation and rupture caused by systemic biological factors and pathological fluid shear stresses leading to a (mal)adaptive mechanotransducive response [19, 35]. Another potential cause of graft failure along the anastomotic interface is the mismatch of mechanical properties (e.g., stress state, compliance, strain) between the graft and target vessels [36]. The difference in mechanical behavior promotes unequal diametral expansion leading to an increase in suture-line stress magnitudes along the surgical interface, and development of

local pathological flow patterns [36]. Pathological flow (i.e., low/high wall shear stresses, flow separation, or recirculation) persists at sites of sudden changes in geometry (e.g., points of curvature, bifurcations, or stenoses) [37–39].

ECs and SMCs are mechanosensitive cells that play a large role in the vascular remodeling process because they are capable of sensing mechanical and hemodynamic gradients and respond by increasing ECM protein deposition and initiating prothrombotic and proinflammatory signaling [40–42]. The expression of proinflammatory endothelial receptors (e.g., vascular adhesion molecule-1 [VCAM-1]) and prothrombotic surface receptors (e.g., von Willebrand Factor [vWF]) are sensitive to local flow disturbances [43]. For example, Figure 1.3 displays immunohistochemistry cross-sectional images of an end-to-end sham anastomosis (ITA-ITA) where the red signal is representative of vWF. These images show that vWF is highly expressed at the anastomotic interface in comparison to the control vessel (Figure 1.3).

Overall, the mechanobiological basis for graft-host diseases along surgical interfaces (i.e., the intrinsic link to thrombosis, fibrosis, and inflammation) based on mechanical incompatibility is difficult to discern from those of the fundamental anastomosis procedure. For instance, mechanobiological consequences are known to persist depending on the grafting configuration and anastomotic closure system thereby influencing graft tissue resilience [4, 37]. Therefore, selection of an appropriate grafting conduit that minimizes mechanical, geometric, and hemodynamic gradients is important for maximizing CABG outcomes [15].

1.4 STRATEGIES TO ALLEVIATE GRAFT SHORTAGES

Although autologous tissue sources are the preferred option for CABG procedures, autografts present a major clinical and logistical challenge of tissue availability. Many of the 400,000 CABG procedures necessitate revascularization for multiple coronary arteries. Clinical assessments of graft patency has shown that more extensive grafting networks like that seen in the bilateral ITA configurations result in greater patency than single ITA grafts but require more grafting tissue [44, 45]. The limited supply of adequate graft resources necessitates the development of an appropriate "off-the-shelf" CABG options, or, at the very least, a means of effectively preserving excess autologous tissue during the initiating surgical procedure. The use of acellular xenogenic conduits and vascular cryopreservation, for example, are some of the emerging alternative strategies that can aid in addressing the high surgical demand of patent CABGs.

1.4.1 Xenogenic Tissue Sources

The use of tissue-engineered blood vessels (TEBVs) is being explored to alleviate graft tissue shortages [46, 47]. Xenogenic tissue (i.e., harvested from another species) present several advantages to alleviating graft shortages. For instance, the preferred autograft option, the ITA, can be harvested from a pig, for example, and implanted in CABG procedures. The major consequence of immediate implantation is the need for the patient to remain on immunosuppressors for the rest of their life. One promising technique to circumvent this issue is decellularization of xenogenic tissue sources [48].

The process of decellularization involves the complete removal of cellular and nuclear material from the vessel while maintaining the native extracellular matrix (ECM) of the tissue [49]. Decellularization has proven to be an effective laboratory technique that

can enhance the *in vivo* performance of vascular conduits, but there are several challenges involved in their clinical implantation [50]. For example, acellular conduits lack an endothelium and the exposure of the collagen basement membrane to circulating blood would initiate pro-thrombotic pathways that present a considerable risk of platelet aggregation and TEBV failure [50, 51]. Despite the inherent advantage of removing immunogenic materials to mitigate host rejection, the wide-spread use of acellular grafts is limited by thrombosis, restenosis, and aneurysm formation.

Decellularization can be achieved through physical, chemical, or enzymatic agent that effectively remove all cellular and nuclear material from a xenogenic sample [52–55]. Several studies have shown that although multiple freeze-thaw cycles are effective at creating an acellular scaffold, it severely disrupts the scaffold's ECM microarchitecture and weakens the scaffold's mechanical behavior [48]. Additional chemical agents such as cryoprotectants or osmotic buffers are necessary to mitigate intracellular fluid exchange and minimize adverse freezing artifacts using freeze-thaw decellularization [48, 51]. Chemical agents (e.g., ionic, non-ionic, zwitterionic detergents) are more efficient decellularization methods. Ionic detergents such as sodium dodecyl sulfate (SDS), sodium deoxycholate (SDC), and Triton X-100 effectively decellularize biological tissues by solubilizing cell membranes [48, 56]. Unfortunately, these agents have been shown to effectively remove GAGs and denature ECM proteins like collagen thereby significantly altering the tissue's mechanical properties [48, 57]. Furthermore, the polarity of these ionic detergent make it difficult to wash them out after decellularization, and the retention of cytotoxic agents diminish the recellularization efficacy [48, 51]. Decellularization with enzymes that target and degrade nuclear material such as deoxyribonuclease (DNase I) are

often used in conjunction with other methods to effectively remove cellular waste. The use of supercritical carbon dioxide has emerged as a promising decellularization method that effectively disrupts cellular membranes while preserve ECM structures and the tissue's gross mechanical properties [58]. Future tissue engineering investigations can employ a combinative approach to decellularization with multiple methods or individual agents is the best way to achieve an acellular scaffold with minimized biochemical and biomechanical consequences [48, 51, 57]

1.4.2 Arterial Cryopreservation

The development of tissue banks for autografts, allografts, or xenografts could help address the graft shortages observed in secondary CABG surgeries [59, 60]. The window for preserving the tissue's properties for research and clinical purposes is narrow with concerns over enzymatic degradation of ECM structures quickly altering innate biomechanical and biochemical properties [61]. Preservation of biological materials and tissues can be achieved by placing samples in hypothermic storage conditions to minimize all genomic and proteomic activity thereby allowing the cells to enter a state of dormancy [62]. Therefore, appropriate freezing and preservation strategies for the storage or transportation of arteries are necessary to mitigate adverse biological and mechanical consequences [63]. Cryopreservation is the process of freezing biological materials in a way to retain cell and tissue structure and functionality upon thawing [64, 65]. Although seldom addressed in the literature, the rapid exchange of liquid media and temperature-dependent conformational changes in protein structure, the chosen cryopreservation technique can significantly alter tissue behavior and function. Such changes would affect

any cross-institutional investigations or clinical implementation that requires transportation or long-term storage [62].

A major obstacle to cryopreservation is the formation of unwanted intracellular ice crystals that damage cell membranes and ECM materials [62]. Damage-limiting cryopreservation techniques such as the use of cryoprotecting agents (CPAs) are effective at facilitating fluid exchange and minimizing ice-crystal formation. The choice of CPA is dependent upon the targeted protection of intra- and/or extracellular structures [62]. Dimethyl sulfoxide (DMSO) is the most commonly used CPA because it can penetrate through cell membranes to replace intracellular water thereby lowering the solvent freezing temperature [62, 66]. Concentrations of DMSO ranging from 5-12% are necessary to create amorphous ice structures that lack the molecular lattice seen in damage-forming ice crystals [62]. However, prolonged exposure to these agents can lead to cryoprotectant cytotoxic effects, and therefore, the choice of CPA and the concentration used warrant consideration [66]. Other technical factors, such as the freezing and thawing rates, can also mitigate the exchange of fluids and influence the viability of cells and tissues [67]. A controlled freezing rate of -1°C/min, for example, has been shown to maintain membrane integrity throughout, while a rapid thawing rate minimizes ice recrystallization [66]. Likewise, the most effective method to maintain membrane integrity and protein functionality for long periods of time is storing at a temperature of -196°C [66–68]. While the inclusion of these agents and methods are widely implemented for isolated cells, little work has been done on optimizing these freezing strategies for the preservation of elastomuscular arteries. In comparison to other tissues, the requisite dual protection for the native elastin and collagen structure from extracellular ice crystal damage and SMC

membranes from intracellular ice nucleation present new challenges [66]. Overall, the preservation of donor elastomuscular arteries (i.e., allografts or xenografts) could aid in the development of a biobank housing reliable CABG alternatives.

1.5 SUMMARY

The native loads, mechanical properties, and wall microstructure of graft vessels such as the ITA differs based on anatomical location. Likewise, vessels of the coronary vasculature possess unique histomechanical properties well-suited for the myocardium. In this dissertation, we aim to describe the distinct properties and anastomotic behavior of different ITA-based CABGs through the material and mechanical characterization of the left and right ITAs along their lengths (Chapter 2) and the *in silico* quantification of mural and hemodynamic stress concentrations at the anastomotic junction using distinct ITA grafting regions and several common, and clinically relevant, coronary target vessels (Chapter 3). We then improve upon two strategies aimed at alleviating graft shortages through the quantification of the biochemical and biomechanical consequences of detergent-based xenograft decellularization (Chapter 4) and then through optimizing the biomechanical, microstructural, and metabolic consequences of cryopreservation (Chapter 5). Through extensive biomechanical analysis that has been motivated by emerging mechanobiology, this work contributes to strategies for improving CABG outcomes.

1.6 FIGURES

Figure 1.1 - End-to-end sham anastomosis of a female porcine ITA sample secured using nonpenetrating vascular clips and mounted within a culture chamber.

Figure 1.2- Parallel *ex vivo* pulsatile perfusion bioreactors assembled within an incubator. Inlet and outlet pressure gauges sandwich the culture chambers that house the arteries. The outlet tubing passes a clamp which provides the downstream resistance to pressurize the arteries. The outlet tubing leads to a media reservoir, and then the tubing leads out of the incubator and connects to a Masterflex L/S digital drive connected to four Masterflex Easy Load pump heads equipped with four stainless steel rollers to provide physiological pulsatile flow of media (not pictured).

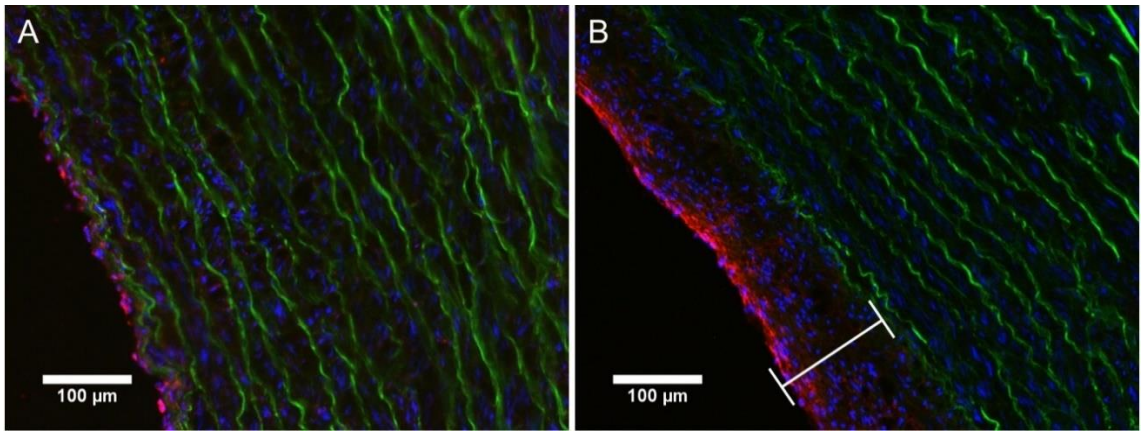

Figure 1.2- Immunohistochemistry images of [A] control and [B] anastomosed ITAs after being cultured under pulsatile conditions for 24 hours. These cross-sections show nuclei (blue), elastin (green), and vWF (red), while the white bracket indicates neointimal thickening.

CHAPTER 2

LONGITUDINAL HISTOMECHANICAL HETEROGENEITY OF THE INTERNAL THORACIC ARTERY [1,^]

[1] Kostelnik, C. J., Crouse, K. J., Carver, W., Eberth J. F. (2021). *Journal of the Mechanical Behavior of Biomedical Materials*, *116*, 104314. doi.org/10.1016/j.jmbbm.2021.104314

Reprinted here with permission of publisher (Appendix A.1)

[^] Corrigendum to Kostelnik et al. (2021) approved August 2022.

2.1 ABSTRACT

The internal thoracic artery (ITA) is the principal choice for coronary artery bypass grafting (CABG) due to its mechanical compatibility, histological composition, anti-thrombogenic lumen, and single anastomotic junction. Originating at the subclavian artery, traversing the thoracic cavity, and terminating at the superior epigastric and musculophrenic bifurcation, bilateral ITAs follow a protracted circuitous pathway. The physiological hemodynamics, anatomical configuration, and perivascular changes that occur throughout this length influence the tissue's microstructure and gross mechanical properties. Since histomechanics play a major role in premature graft failure we tested the regional material and biaxial mechanical properties at four distinct locations along the left (L) and right (R) ITA and fit the results to a structurally-motivated constitutive model. Our comparative analysis of 44 vessel segments revealed a significant increase in the amount of collagen but not smooth muscle and a significant decrease in elastin and elastic lamellae present with distance from the heart. A subsequent decrease in the total deformation energy and isotropic contribution to the strain energy was present in the LITA but not RITA. Circumferential stress and compliance generally decreased along the length of the LITA while axial stress increased in the RITA. When comparing RITAs to LITAs, some morphological and histological differences were found in proximal sections while distal sections revealed differences predominantly in compliance and axial stress. Overall, this information can be used to better guide graft selection, graft preparation, and xenograft-based tissue-engineering strategies for CABG.

2.2 INTRODUCTION

Contemporary coronary artery bypass grafting (CABGs) utilizes autologous tissue sources to reestablish blood flow around occluded coronary arteries [53]. Currently, the most frequently used autograft conduits include the left (L) and right (R) internal thoracic arteries (ITA) (also known as internal mammary), radial artery, great saphenous vein, and to a lesser extent, the gastroepiploic and inferior epigastric arteries [10, 13, 14]. The histoarchitecture of these, and other blood vessels, have been shown to have a strong dependency on the local hemodynamic conditions, perivascular environment, and overall biological function [21, 69]. These distinct characteristics have contributed to their differential performance in studies that highlighted the role of tissue-specific material, mechanical, and morphometric parameters have on graft patency [10, 13, 20, 21, 70]. From these, the ITA has been identified as a superior candidate for autograft CABG configurations due predominantly, to its anatomical location, coronary-like material parameters, and low risk for atherosclerosis [10, 13, 23, 71].

The ITA originates from the subclavian artery and traverses the thoracic cavity terminating at the superior epigastric and musculophrenic artery bifurcation near the sixth intercostal space [72]. The proximal region of the ITA, between the origin and the first intercostal branch, is located within the thoracic cavity. Notably, the ITA experiences a shift in perivascular surroundings near the first intercostal space, where it penetrates the transverse muscle of the thorax [72]. Due to this dramatic change, the ITA has been described by the relative distance from the heart to have three histological patterns, namely elastic, elastomuscular, and muscular [23, 73].

An anatomical characteristic that facilitates the use of the ITA in CABG configurations is its relative proximity to the anterior side of the heart. This allows for the origin to remain intact and requires only one anastomosis for most anterior CABG configurations [37, 71, 74]. Likewise, the orientation of appropriate CABG configurations to achieve reperfusion is dependent upon the location and number of stenoses [26, 75, 76]. In cases of distal stenoses, for example, surgeons may employ the distal region of the ITA and/or its subdivisions to revascularize the myocardial tissue [76]. However, care must be taken when grafting distal regions of the ITA because they exhibit a high degree of contractility and pharmacological sensitivity that may lead to vasospasm and decreased patency rates [19, 25, 76]. Likewise, mechanical mismatching appears to be important in long-term graft patency [10, 13, 75]. Mismatched tissues are at an increased risk for inflammation and atherosclerotic plaque formation especially around the anastomotic junction [21, 25, 75].

The variable patency rates associated with autografts are complex. In this study, we investigated the spatial material and mechanical characteristics of porcine ITAs to elucidate differences that exist in regions of this prominent bypass graft material. The porcine ITA was selected due to its commercial availability, similarity to the human configuration, and as a potential engineering biomaterial with broad-reaching applications. To this end, we quantified histological, morphological, and mechanical metrics of the porcine LITA and RITA at four anatomically distinct regions along its path. The data was fit to constitutive models within a continuum mechanics framework to facilitate translation of the results.

2.3 MATERIALS AND METHODS

2.3.1 Tissue Acquisition and Segment Selection

Left and right ITAs were acquired at a local abattoir from 2-year-old American Yorkshire sows weighing approximately 200 kg. All tissues were dissected under sterile conditions within 30 minutes of slaughter and transported in 1% phosphate-buffered saline (PBS) with heparin sodium (20 units/mL) to the lab. There, vessels were dissected into four distinct anatomical segments for histological and mechanical evaluation (Figure 2.1). For both LITAs and RITAs, these segments include, (1) a proximal segment comprising the region nearest to the subclavian artery, (2) the submuscular segment where the ITA penetrates the muscle of the anterior chest wall, (3) the middle segment between intercostal branches, and (4) the distal segment is the region nearest to the superior epigastric and musculophrenic bifurcation. The absolute and relative distances from the distal bifurcations were recorded for each segment (Table 2.1). All segments were refrigerated at 4°C until mechanical testing at body temperature or histological evaluation could be performed. Testing was always completed within 48 hours of animal sacrifice.

2.3.2 Histological Analyses

ITA segments were fixed in 4% paraformaldehyde and embedded in paraffin wax. Sections were cut at 5 μm and stained with Movat's Pentachrome. Tissue segments from the same vessel were processed together to facilitate a uniform histological comparison at different locations along the ITA. Images were then obtained using a Nikon E600 microscope with a CCD camera and computer interface with QCapture (QImaging). Each section was imaged at eight different locations around the circumference of the vessel. Area fractions of elastin, smooth muscle cells (SMCs), collagen, and glycosaminoglycans

(GAGs) were found using ImageJ software (NIH) with the "Threshold_Colour" plugin, to estimate the pixel-to-pixel ratio of deep red/brown, red, yellow, and blue pixels to total tissue for each constituent, respectively [10]. To ensure consistency across samples, the standard threshold values were fixed at specified brightness, saturation, and hue ranges. Deep red/Brown pixels were quantified using a bandpass from brightness 26-115 and saturation 42-162, and a bandstop filter hue 21-228; red pixels were quantified using a bandpass filter from brightness 123-190 and saturation 0-72, and a bandstop filter hue 24-228; yellow pixels were quantified using a bandpass filter from brightness 123-190, saturation 0-159, and hue 28-90; and blue pixels were quantified using a bandpass filter from brightness 46-211, saturation 0-159, and hue 115-211. The sums of these areas were then normalized to 100% for each sample. Mean and standard deviations for each group were found from a sample size of n=5.

Morphometric analysis was performed on the Movat's Pentachrome stained ITA sections to gain insight on alterations in vascular wall composition along its length. Tunica intima, media, and adventitial thicknesses were measured at five different locations of each segment. Specifically, intima thickness was measured from the lumen to the internal elastic lamellae (IEL), media thickness was measured from IEL to external elastic lamellae (EEL), and adventitia thickness was measured from the EEL to the edge of adventitia.

2.3.3 Immunohistochemistry and Elastin Autofluorescence

ITA sections were stained with propidium iodide (500 nM) to visualize the cell nuclei and elastin autofluorescence used to visualize elastic lamellae. Images were captured on a fluorescent microscope (Axio Imager.A1, Zeiss) attached to a camera (AxioCam MRc5, Zeiss), and analyzed using ImageJ software (NIH). ITA segments were imaged at

eight different locations to provide an accurate representation of the total wall structure within that segment. Assuming SMCs constitute the predominant cell type of the medial layer, the SMC count was performed by thresholding the propidium iodide signal in the Rhodamine channel. A region of interest (ROI) was generated for each image from the IEL to EEL. Size and circularity restrictions were imposed on all images to ensure consistency and reproducibility. The number of elastic lamellae found within each segment of the LITA and RITA was recorded.

2.3.4 Biaxial Mechanical Testing

Passive inflation-extension testing was carried out using a Bose BioDynamic 5270 biaxial mechanical testing device. All ITA segments were cut into approximately 3 cm sections and mounted onto two luer fittings with 3-0 braided sutures. Vessels were then immersed in and perfused with, 1% PBS and sodium nitroprusside (10^{-5} M) to elicit a fully relaxed state of SMCs. Initial measurements of the unloaded length were recorded for the calculation of axial stretch ratios. Sample sizes of n=5 to 6 were included for each group with a total of 44 samples used in this study.

Each vessel underwent five cycles of axial extension and inflation preconditioning to minimize viscous dissipation and to ensure reproducible results. Throughout mechanical testing, the pressure was increased from 0 to 200 mmHg in increments of 20 mmHg, while the pressure-outer diameter and pressure-axial force data were recorded. The so-called "*in vivo* axial stretch ratio" was found at the axial displacement that yielded an invariant axial force in response to increasing pressure. Data collection was completed at the approximate *in vivo* axial stretch ratio as well as 10% above and below that specified stretch ratio.

Between tests, the axial displacement was increased at a rate of 0.03 mm/s. Each test was completed in triplicate and the average of these tests used to form group averages.

Immediately following biaxial mechanical testing, a 1 mm thick ring segment from the middle region of each vessel was excised and imaged and then a radial cut introduced to relieve residual stress from the tissue. Opened sectors were equilibrated for 30 min in sterile PBS and imaged using a Canon EOS 60d camera. ImageJ software was then used to measure the cross-sectional area A, inner arc length L_i, and outer arc length L_o. From these measurements we used

$$H = \frac{2A}{L_i + L_o} \text{ and } \Phi = \pi - \frac{L_o - L_i}{2H} \tag{1}$$

to calculate the stress-free thickness H and opening angle Φ.

2.3.5 Biaxial Data Analysis

Vessels were assumed to be thin, cylindrical, incompressible tubes that experience finite elastic deformation under inflation and extension. Throughout inflation-extension testing, the luminal pressure P and axial displacement were controlled, while the deformed outer radius r_o and axial force F were recorded. Under the assumption of tissue incompressibility, the inner radius r_i was calculated from

$$r_i = \sqrt{r_o^2 - \frac{A}{\pi \lambda_z}} \tag{2}$$

These measurements were then used to calculate the mean circumferential σ_θ, and axial stresses σ_z,

$$\sigma_\theta = \frac{P r_i}{h} \text{ and } \sigma_z = \frac{F}{\pi \left(r_o^2 - r_i^2 \right)}, \tag{3}$$

where $h = r_o - r_i$ is the deformed wall thickness. The mid-wall circumferential λ_θ and axial stretches λ_z are calculated from,

$$\lambda_\theta = \frac{2\pi\left(r_i + r_o\right)}{L_i + L_o} \text{ and } \lambda_z = \frac{l}{L}, \tag{4}$$

with l and L, the deformed and undeformed lengths, respectively. The lumen area compliance is calculated using

$$C_A = \pi \frac{\Delta r_i^2}{\Delta P}, \tag{5}$$

where Δr_i is the change in radius for a given change in pressure, ΔP. In our study, this value was taken around a 100 ± 20 mmHg operating point.

2.3.6 Theoretical Framework

A structurally-motivated constitutive model initially proposed by Holzapfel, Gasser, and Ogden (HGO), and later modified to include four fiber families of collagen [77, 78] was utilized so that the strain energy function takes the following form,

$$W\left(\mathbf{C}, \mathbf{M}^k\right) = \frac{c}{2}\left(I_C - 3\right) + \sum_{k=1}^{4} \frac{c_1^k}{4c_2^k}\left\{\exp\left[c_2^k\left(IV_C^k - 1\right)^2\right] - 1\right\}, \tag{6}$$

where $\mathbf{C} = \mathbf{F}^{\mathbf{T}}\mathbf{F}$ is the right Cauchy-Green deformation tensor with $\mathbf{F} = diag\left(\lambda_\theta, \lambda_z, \lambda_r\right)$ the deformation gradient tensor, and I_C and IV_C^k, the first and fourth principal invariants of $\mathbf{C}$, respectively. These invariants are defined as

$$I_C = tr(\mathbf{C}) = \lambda_\theta^2 + \lambda_z^2 + 1/\left(\lambda_\theta\lambda_z\right)^2 \text{ and } IV_C^k = \mathbf{M}^k \cdot \mathbf{C}\mathbf{M}^k = \lambda_\theta^2 \sin\alpha^k + \lambda_z^2 \cos\alpha^k, \tag{7}$$

with $\mathbf{M}^k = \left(0, \sin\alpha^k, \cos\alpha^k\right)$ a unit vector oriented in the direction of the k^{th} fiber at an angle relative to the axial direction. Here c is a material parameter representing the

isotropic contribution to the total strain energy while c_1^k and c_2^k are parameters for each of the k^{th} fiber families. We further let $\alpha^1 = 0$ represent a family of axially oriented fibers, $\alpha^2 = \pi/2$ the circumferentially oriented fibers, and $\alpha^3 = -\alpha^4$, $c_1^3 = c_1^4$, $c_2^3 = c_2^4$, and $c_2^3 = c_2^4$, symmetric and diagonal fibers.

To reduce the problem to plane stress, we assume that radial stress is much less than the axial or circumferential stress so that the Cauchy stress is given as,

$$t_{\theta\theta} = \lambda_\theta \frac{\partial W}{\partial \lambda_\theta} - \lambda_r \frac{\partial W}{\partial \lambda_r}, \; t_{zz} = \lambda_z \frac{\partial W}{\partial \lambda_z} - \lambda_r \frac{\partial W}{\partial \lambda_r}, \tag{8}$$

with pressure and force as

$$P = \frac{h}{r_i}\left[\lambda_\theta \frac{\partial W}{\partial \lambda_\theta} - \lambda_r \frac{\partial W}{\partial \lambda_r}\right] \text{ and } F = \pi h\left(2r_i + h\right)\left[2\lambda_z \frac{\partial \hat{W}}{\partial \lambda_z} - \lambda_\theta \frac{\partial \hat{W}}{\partial \lambda_\theta}\right]. \tag{9}$$

Modeling parameters are found by minimizing the objective function between the experimentally measured (exp) and modeled (mod) pressure and force

$$e = \sum_{j=1}^{n}\left[\left(\frac{P^{mod} - P^{exp}}{\bar{P}^{exp}}\right)_j^2 + \left(\frac{F^{mod} - F^{exp}}{\bar{F}^{exp}}\right)_j^2\right], \tag{10}$$

with the total of observations and the over-bar denoting the mean value. Multivariate regression analysis was performed using MATLAB's optimization toolbox (MathWorks; Natick, MA) function lsqnonlin. Initial values were generated randomly, and bounds were assigned so that all parameters were greater than zero and $0 < \alpha < \pi/2$. Prior work using bootstrapping has revealed that pointwise estimates provide reasonable estimates without constituting a local minimum [79, 80]. Therefore, optimization was performed a total of 6

times with values reported that represent the minimal root-square-error of the mean for averaged data.

2.3.7 Statistics

GraphPad Prism 9.0 was used to investigate comparisons of the material and mechanical properties between and within the LITA and RITA groups. The Shapiro-Wilk normality test was performed to determine if all data sets were normally distributed. Data sets were analyzed with one and two-way ANOVAs in conjunction with Tukey's post-hoc test. Significant relationships between vessel locations are denoted with (*) at $p<0.05$, (**) at $p<0.01$, and (***) at $p<0.001$, while (#) denotes differences between the LITA and RITA vessels at $p<0.05$.

2.4 RESULTS

2.4.1 Microarchitecture and morphometric analysis

From thresholding analysis of Movat's Pentachrome stained cross-sections, elastin was found to be the dominant constituent in proximal ITA sections (Figure 2.2 & 2.3). The elastin area fraction of L1 (0.384 ± 0.032) segments was greater than L2 (0.339 ± 0.023, $p = 0.016$) or L4 (0.278 ± 0.041, $p = 0.003$). These changes corresponded with an increase in collagen area fraction from the L1 (0.248 ± 0.027) segment to the L2 (0.305 ± 0.015, $p = 0.007$) and L4 (0.337 ± 0.022, $p < 0.001$) locations. Likewise, elastin content in R1 segments (0.371 ± 0.024) was significantly greater than in R4 (0.264 ± 0.073, $p = 0.033$). Similar to the LITA, there was an increase in collagen content in the R4 (0.346 ± 0.027,) segment compared to the R1 (0.261 ± 0.032, $p = 0.003$). Smooth muscle and GAG area fraction, however, remained relatively consistent with no significant alterations throughout or between contralaterals. In both the L4 and R4 segments, the SMC and collagen

collectively contributed more to the vascular wall composition than elastin, with the latter forming a thicker adventitial layer (Figures 2.2-2.4). Overall, the effect of segmental distance from the heart had a stronger influence over histoarchitecture than comparisons made between contralateral vessels with the only notable exception found in the L2 segment which had a higher collagen content compared to the R2 ($p = 0.001$).

Our morphometric study revealed that the contribution of the individual layers to the total vascular wall composition varied, and these differences were most pronounced in the RITA (Figure 2.4) with a medial thickness that significantly decreased between the R1 (0.531 ± 0.074 mm) and R4 (0.385 ± 0.085 mm, $p < 0.001$) segments and an adventitial thickness that significantly increased between the R2 (0.051 ± 0.017 mm) and R4 (0.101 ± 0.049, $p = 0.033$) segments. The overall thickness of the LITA, but not RITA, was conserved. When comparing LITAs to RITAs, the only major difference noted was the L1 medial thickness (0.437 ± 0.057 mm) which was significantly less than the R1 medial thickness (0.531 ± 0.074 mm, $p = 0.002$). Quantitative results also revealed a significant decrease in the number of elastic lamellae present in the media between the L2 (17.6 ± 0.87 lamellae) and L3 (14.6 ± 1.71 lamellae, $p = 0.030$) segments, L3 and L4 (9.2 ± 1.59 lamellae, $p = 0.060$) segments, and between the R2 (17.8 ± 1.10 lamellae) and R3 (13.1 ± 1.67 lamellae, $p = 0.006$) segments (Figures 2.5 & 2.6). Like Movat's staining, propidium iodide revealed relatively consistent cellularity, in terms of nuclei area density, across the ITA segments with no significant differences observed between matched LITA or RITA segments (Figure 2.6A).

2.4.2 Biaxial Mechanics

Data taken from stress-free ring sectors revealed no statistically significant differences between groups except that the L2, R2, and R3 opening angles were each significantly less than L1 (Table 2.2). The *in vivo* axial stretch ratio was highest for the L1 (1.52 ± 0.04) and lowest for the L4 (1.45 ± 0.01) with a downward but statistically insignificant trend with distance from the heart (not shown). Figure 2.7 reports the averaged biaxial data at the approximate *in vivo* axial stretch ratio for continuous testing. The middle and distal segments of the LITA and RITA exhibited a qualitatively reduced outer diameter over the entire pressure range than the proximal and submuscular segments (Figures 2.7A & 2.7B). All vessels exhibited increasingly nonlinear pressure-diameter behavior at physiological and supraphysiological pressures, but none of these showed the inflection points common to smaller arteries. The proximal and submuscular segments of the LITA and RITA display similar axial force-pressure relationships at a common axial stretch ratio (Figures 2.7C & 2.7D). The middle and distal LITA axial force values were similar to those seen in the RITA and did not exhibit a location dependency (Figure 2.7C). When the continuous circumferential stress-stretch data was plotted (Figures 2.7E & 2.7F), a qualitatively stiffer behavior was demonstrated in terms of the increase in stress for a given change in stretch ratio, in the R1, R3, and R4 segments at high circumferential stretches compared to other segments from this same vessel. The axial stress-stretch plots (Figures 2.7G & 2.7H) revealed a close association amongst the LITA segments while the RITA changed with distance from the heart.

When compared at common loading conditions (i.e., 100 mmHg, 1.55 axial stretch ratio) some significant differences emerged in geometric and mechanical metrics

throughout the LITA and RITA segments (Figure 8). Axial stress for example, significantly increased between the L2 (115.5 ± 27.8 kPa) and L3 (227.1 ± 103.2 kPa, $p = 0.044$) segments, and the R4 axial stress value (260.4 ± 62.2 kPa) was significantly greater than R1 (113.2 ± 50.2 kPa, $p = 0.003$) or R2 (122.2 ± 34.5 kPa, $p = 0.004$). Likewise, when comparing contralateral vessels, the L4 axial stress value was found to be significantly less than R4 ($p = 0.049$). There was also a significant decrease in the circumferential stress values between the L1 (221.8 ± 52.7 kPa) segment and the other LITA segments ($p \leq 0.026$). No differences, however, were related to the circumferential stretch ratio for any groups. Lumen area compliance calculated between distension pressures of 80 and 120 mmHg revealed a significant decrease between the L1 (0.237 ± 0.053 mm2/mmHg) segment and L2 (0.148 ± 0.027 mm2/mmHg; $p = 0.004$), L3 (0.153 ± 0.029 mm2/mmHg; $p = 0.006$), and L4 (0.098 ± 0.033 mm2/mmHg; $p < 0.0001$) segments (Fig 8G & 8H). No other differences in compliance were found between groups or when comparing segment-matched LITAs to RITAs.

By plotting the experimental and modeled force-pressure relationship for three axial stretch ratios the constitutive modeling revealed a set of best-fit parameters that demonstrated an excellent fit to the experimental data (Figure 2.9; Table 2.3) with an average root mean square error (RMSE) of 0.213 across all samples. Although care is taken not to over-interpret the results of parameter estimation, we observed that the isotropic parameter c (often associated with medial elastin), largely demonstrated a decrease in distal sections. LITA and RITA samples demonstrated moderately anisotropic behavior in terms of strain energy contours (Figure 2.10) with higher isotropy present in proximal sections of the LITA (not shown) and most sections of the RITA performed similarly to the

proximal LITA. However, at axial and circumferential stretch ratios approximating the *in vivo* conditions at 100 mmHg, the energy due to deformation was greater in the L1 (53.5 ± 8.52 kPa) than the L2 (33.48 ± 3.33 kPa, $p = 0.016$) or L4 (27.06 ± 9.17 kPa, $p = 0.001$) segments while little change in energy was observed across the RITA (open circles Figure 2.10).

2.5 DISCUSSION

Current CABG procedures rely on autologous tissues to achieve sufficient myocardial revascularization. Tissue-engineered blood vessels, such as those modeled on decellularized porcine xenografts, could eventually be used to increase long-term graft patency due, in part, to the accurate matching of biochemical and mechanical properties [81, 82]. In the meantime, however, the ITA serves as a natural and appropriate bypass graft material due to its anatomical location, the requirement for a single anastomosis, bilateral configuration, and overall length [37, 74, 83]. Since inadequately matched graft tissues have poor long-term patency rates, it is important to understand how the material properties vary along the length of the vessel [10, 69]. This is especially true for distal coronary occlusions requiring bypass configurations that use either the distal ITA, or other vessel subdivisions, bilateral autograft configurations, or coronary-coronary grafting configurations [37, 73, 76, 83]. The purposes of this study were to characterize the material properties of the American Yorkshire porcine ITA as an engineering biomaterial and to suggest potential spatial heterogeneities that may exist in human tissues. Our high-volume study presents the first biaxial mechanical data of its kind revealing how the observed differences in vascular wall composition have influenced the local mechanical behavior of the LITA and RITA.

Others have described the ITA as having material characteristics of a small but elastic-type of artery [73]. This unusual classification is supported by our work with notable regional differences that were found through histological quantification. We specifically noticed changes in the primary load-bearing constituents; namely elastin and collagen, with little effect on glycosaminoglycans. These results further validated previous claims that spatial heterogeneity exists throughout the ITA but with only minor differences present between contralaterals [71, 73, 74, 84]. Notably, the distal portions of the ITA exhibit histological features that are less akin to an elastic artery and more closely resemble a transitionary type [23, 73, 76]. This change, however, was not due to an increase in smooth muscle, per se. The overall pattern was supported by the mechanical and constitutive modeling results from the LITA but was less pronounced in RITA specimens. Moreover, the lamellae that were found and counted in the distal segments of our study were less organized and more fragmented. This particular finding agrees with Marx et al. (2001) as well as Sahar et al. (2015) who found that the number of elastic lamellae within the ITA wall decreases distally, whereas the collagen and smooth muscle content increases. Although prior studies have identified the uniaxial mechanical behavior of ITA segments (i.e., ring tests), such tests cannot mimic *in vivo* loading conditions, neglect the contribution of axial loads and residual stresses, and have severe bending around the fixtures [85]. Therefore, we used biaxial techniques with the results fit to contemporary constitutive models that increase experimental rigor and to enhance the translation of the results.

Vascular smooth muscle cells play important regulatory roles in maintaining local hemodynamic conditions and global peripheral resistance by altering the vessel's diameter via contraction/relaxation pathways. In a clinical setting, a greater presence of SMCs

within the grafting tissue (i.e. muscular-type arteries) presents an increased risk of vasospasm and has a direct impact on the postoperative patency of the graft [23, 25]. In general, the ITA exhibits an overall low-level of vasocontractility in comparison to other autograft sources [25]. However, others have observed that the distal ITA exhibits a muscular-type of phenotype and therefore contains a higher degree of vasoreactivity [76, 86]. Our Movat's Pentachrome quantification did not confirm those results. Instead, our tissues demonstrated similar SMC content across the ITA and its subdivisions and would therefore likely be uniformly reactive to spasmogenic agents. Differences in quantification between ours and other studies could be attributed to alterations in assessment techniques. For example, our histological approach normalized SMCs to the medial cross-sectional area and did not seek to identify SMC phenotype. To that point, our biaxial mechanical tests were all performed under a passivated state with minimal contribution of smooth muscle to the overall response. Further studies into the level of smooth muscle contractility using passive-active biaxial testing would be necessary to expand this hypothesis [87].

Collagen type I is the most abundant subset of collagen in the vascular adventitia, whereas type III is the primary collagen found within the medial layer [11]. The observed increase in adventitial thickness, axial stress, and axial stiffness within distal segments can be attributed to the significant increase in the collagen area fraction at these locations. It is well known that the amount of collagen present in vascular tissue has a direct impact on mechanical behavior and that fibrous collagen contributes significantly to anisotropy. This behavior is well-illustrated through biaxial mechanical testing and implementation of the HGO four-fiber model. Moreover, it's been hypothesized that an overall increase in the collagen-to-elastin ratio decreases the *in vivo* axial stretch thereby increasing the arterial

stiffness [27, 29]. Others have shown that collagen type I and type III are engaged at different strains that depend on orientation [69]. The biaxial mechanical results of our study illustrate that the axial stress, measured at common loading conditions, significantly increased with relative distance from the heart. The increased adventitial thickness and collagen content within the distal ITA justify the high axial stress value given that discrete comparisons were made at a common axial stretch ratio.

In addition to the presence of small diverting branches, hemodynamic pulsatility is dampened and the physiological blood flow demands altered throughout the length of the ITA coinciding with distance from the pulse-generating heart [88]. The fractional composition of constituents of the aorta, especially in terms of elastin composition, have been well documented and are believed to be responsive to hemodynamic demands throughout development [29, 89]. The amount of collagen in the aorta, on the other hand, is thought to remain relatively constant with distance from the heart [29, 90]. This was not the case in our study, but perivascular factors may also be playing an important role here. For example, in our prior work, we illustrated that the perivascular environment influences the composition of the adventitia of porcine vertebral arteries that experience intra- and extraosseous pathways [22]. In the current study, we defined segments L2 and R2 at an anatomical location whereas the ITA penetrates the muscle of the anterior chest wall, and thus its perivascular environment is dramatically altered at that point. Such changes are reflected in terms of significant histomechanical differences present between these and other segments even though they are in close physical proximity. Regardless, evidence suggests that an overall form-and-function relationship exists for vessels of the body with the ITA possessing characteristics optimized to its native environment.

Despite the implementation of modern techniques in the field of vascular biomechanics, our study on the spatial heterogeneity of ITAs has limitations that warrant further consideration. First, this investigation focused only on the passive mechanics of potential graft tissue with histological analysis of SMC content allowing for inferences to be made on the degree of contractility within ITA segments [87]. To facilitate cross-specimen comparisons at similar loading conditions (Figure 2.8) we used a common axial prestretch which was not the same as the *in vivo* axial stretch value for each specimen. That value trended downward with distance from the heart and is consistent with the reports by Humphrey et al. (2009) showing this value to be inversely related to the collagen-to-elastin ratio. Additionally, all arterial tissue samples were harvested from older sows with unknown nutritional metrics and health status. This particular tissue source was chosen based on widespread availability, to mimic variations in human populations, and to serve as a potential source for xenografts. Other studies and our preliminary histological analysis from our lab (unpublished) have shown that porcine central arteries have many properties similar to those of human vasculature [81, 82, 91] with normalized mechanical properties preserved across species [92]. Lastly, the complex loading and boundary conditions present due to the grafting procedure are not recapitulated in our current study and are the subject of ongoing work. Despite these limitations, our comprehensive approach to spatial ITA histomechanics provides key insights into the importance of autograft tissue selection and foundational knowledge for the further investigation of porcine ITAs as a decellularized xenograft tissue source.

2.6 CONCLUSIONS

Regional differences in material, morphological, and mechanical characteristics were found from 44 left and right porcine internal thoracic artery segments through a combination of histology, anatomical segmentation, immunohistochemistry, biaxial mechanical testing, and constitutive modeling. These differences could be used to design preferred graft configurations and may contribute to altered clinical outcomes.

2.7 FUNDING

This research was supported by NSF EPSCoR OIA-1655740, NSF CMMI-1760906, and NIH R21 EB022131.

2.8 ACKNOWLEDGEMENTS

The authors would like to acknowledge the imaging and histology assistance of Dr. Bob Price and Sharon Cooper, the equipment assistance of Dr. Susan Lessner, and the technical assistance of David Prim, Nazli Gharraee, Liya Du, and Brooks Lane.

2.9 TABLES

Table 2.1 - Segment selection of left and right internal thoracic arteries

ITA Segment	*Distance from distal bifurcation (cm)*	*Total vessel length (cm)*
Left		
L1	17 ± 1.5 – 18.6 ± 0.7	19 ± 4
L2	12 ± 1.3 – 14 ± 0.7	
L3	6 ± 1 – 8 ± 1.4	
L4	0.6 ± 1.4 – 2.5 ± 1.7	
Right		
R1	17 ± 1.2 – 19 ± 0.4	19 ± 2
R2	12 ± 2 – 14 ± 1.7	
R3	5 ± 2 – 8 ± 1.5	
R4	0.2 ± 0.1 – 2.2 ± 1.5	

Table 2.2 - Vessel geometry in the unloaded configuration

ITA Segment	Thickness [H] (mm)	Inner arc length [L_i] (mm)	Outer arc length [L_o] (mm)	Opening Angle [Φ] (°)
Left				
L1	0.46 ± 0.08	15.8 ± 1.69	18.2 ± 1.67	46.5 ± 34.7
L2	0.61 ± 0.06	17.0 ± 1.62	17.7 ± 1.95	145.9 ± 27.8*
L3	0.51 ± 0.07	14.3 ± 2.07	16.4 ± 2.51	66.5 ± 49.9
L4	0.64 ± 0.22	16.4 ± 5.29	17.1 ± 4.75	109.3 ± 59.9
Right				
R1	0.60 ± 0.09	17.0 ± 2.95	19.0 ± 3.38	84.8 ± 46.1
R2	0.61 ± 0.10	15.1 ± 2.62	16.1 ± 2.26	132.9 ± 38.9*
R3	0.58 ± 0.10	16.1 ± 5.45	17.0 ± 5.40	130.4 ± 37.9*
R4	0.48 ± 0.10	13.2 ± 1.91	14.7 ± 1.53	93.9 ± 51.7
* Signifies statistical significance between matched LITA and RITA segments and L1 using one-way ANOVA at $p<0.05$.				

Table 2.3 - HGO model material parameters of the averaged data for segment-specific left and right internal thoracic arteries

ITA Segment	c (kPa)	c_1^1 (kPa)	c_2^1	c_1^2 (kPa)	c_2^2	$c_1^{3,4}$ (kPa)	$c_2^{3,4}$	$\propto$ (rad)	RMSE
Left									
L1	11.92	16.17	0.323	52.61	0.015	16.50	0.779	0.792	0.211
L2	12.78	6.210	0.637	31.75	0.059	6.993	1.292	0.848	0.216
L3	11.79	7.89	0.867	38.37	0.018	4.545	1.638	0.769	0.164
L4	0.720	13.32	0.498	26.82	0.205	6.466	1.427	0.814	0.271
Right									
R1	9.538	15.06	0.198	29.18	0.036	10.43	0.692	0.805	0.173
R2	9.169	8.266	0.373	26.04	0.022	11.39	0.686	0.744	0.221
R3	9.390	9.125	0.686	30.75	0.009	4.652	1.304	0.776	0.202
R4	4.631	15.74	0.560	40.79	0.203	9.226	1.123	0.689	0.249

2.10 FIGURES

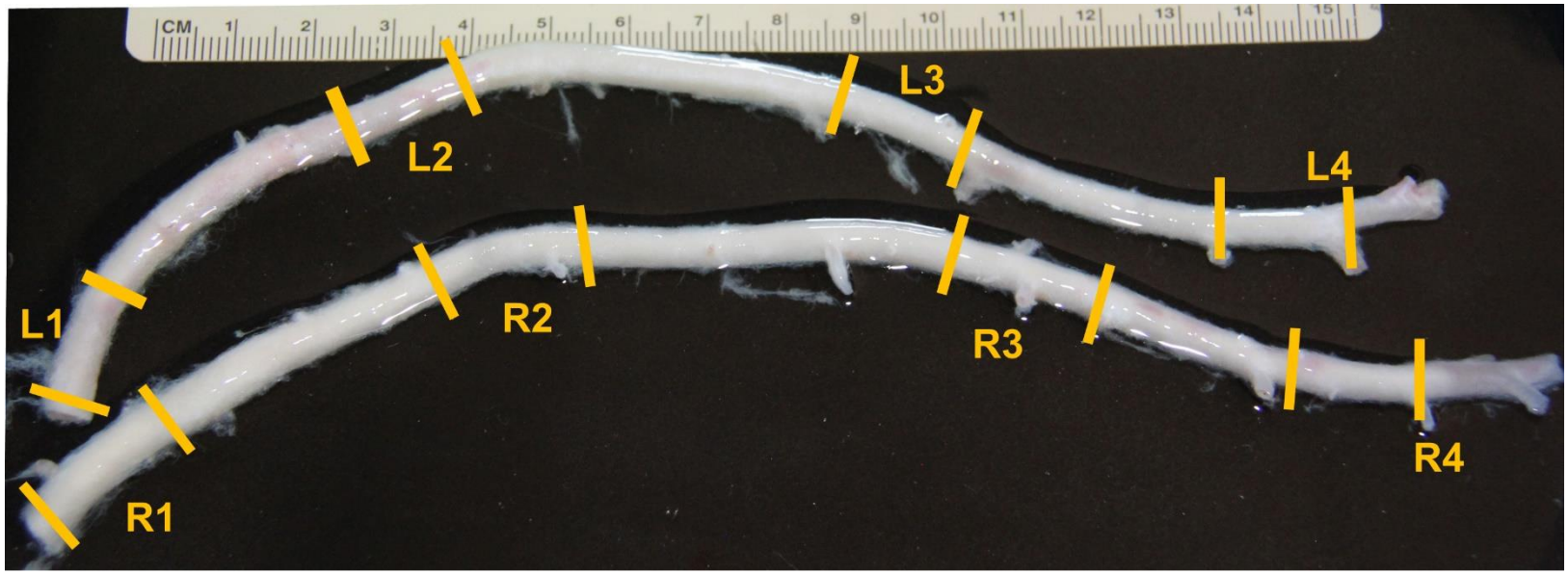

Figure 2.1- Full length porcine left (LITA) and right (RITA) internal thoracic arteries with sections labeled that approximate the (1) Proximal, (2) Submuscularis, (3) Middle, (4) Distal. All segments were taken from the same relative distance from the subclavian artery and distal bifurcation.

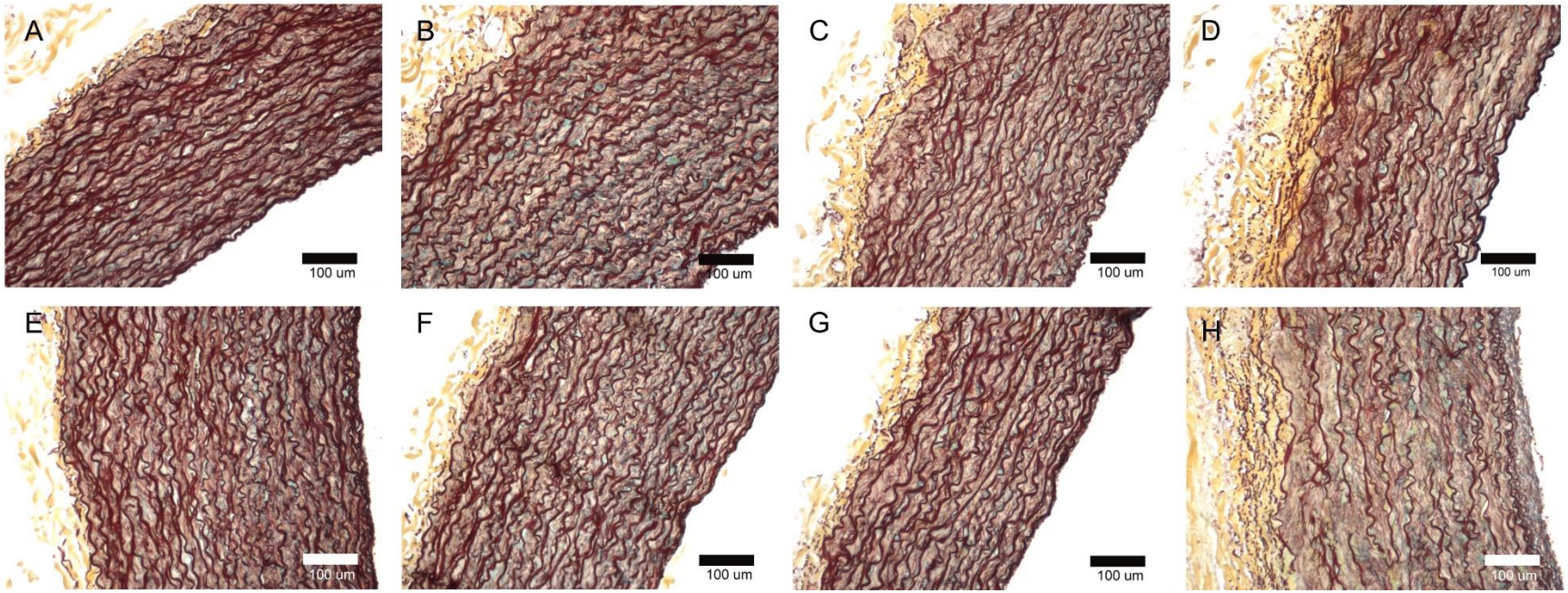

Figure 2.2 - Movat's Pentachrome stain of LITA [A-D] and RITA [E-H] comparing the vascular wall composition across the proximal [A & E], submuscular [B & F], middle [C & G], and distal [D & H] segments.

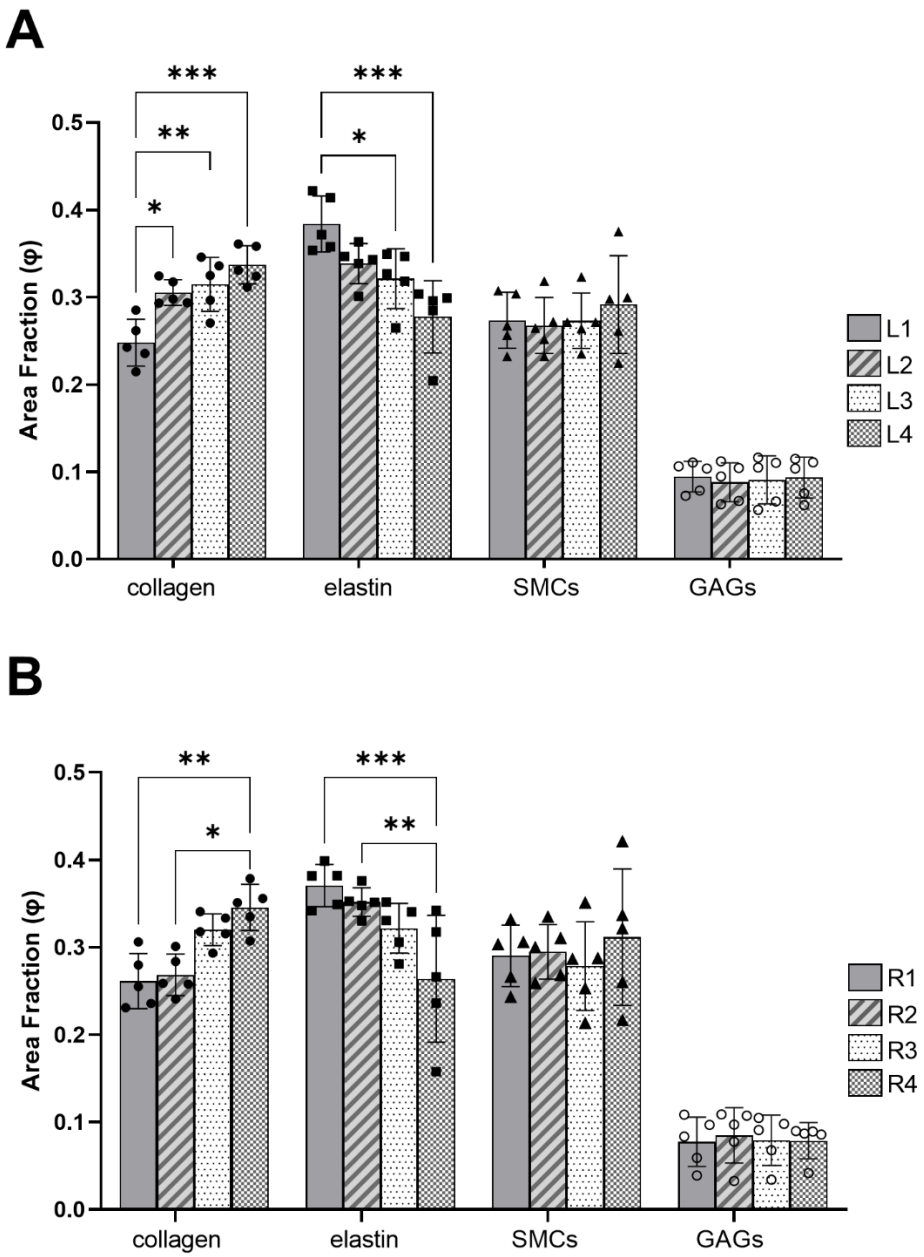

Figure 2.3 - Constituent area fraction of collagen, elastin, smooth muscle cells (SMCs), and glycosaminoglycans (GAGs) determined by thresholding Movat's Pentachrome stained cross-sections for the four anatomical locations along the LITA and RITA. Statistical significance is denoted as (*) when $p<0.05$, (**) at $p<0.01$, and (***) at $p<0.001$. Mean ± SD, n=5 for each group.

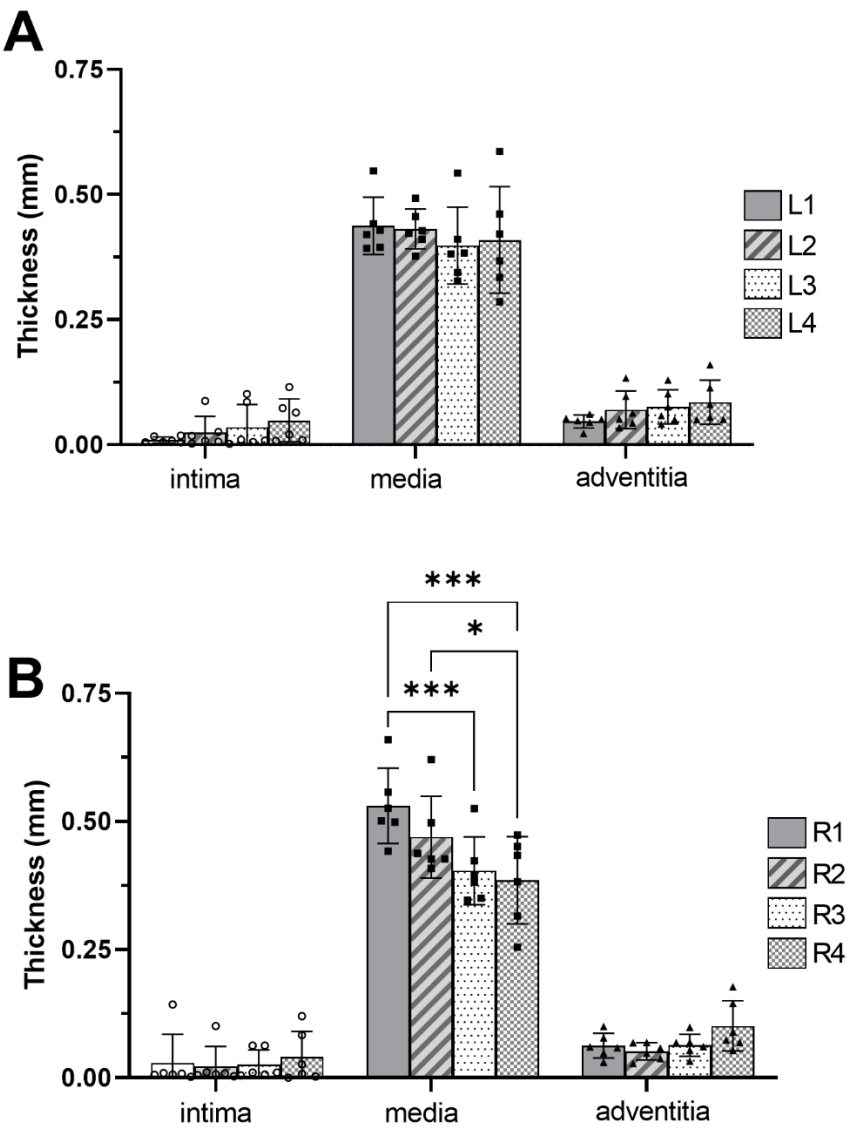

Figure 2.4 - Morphometric analysis of ITA wall composition. Intima, media, and adventitia thicknesses measured from Movat's Pentachrome stained cross-sections and normalized to relative ITA complete wall thickness. Statistical significance is denoted as (*) when $p<0.05$, (**) at $p<0.01$, and (***) at $p<0.001$. Mean ± SD, n=6 for each group.

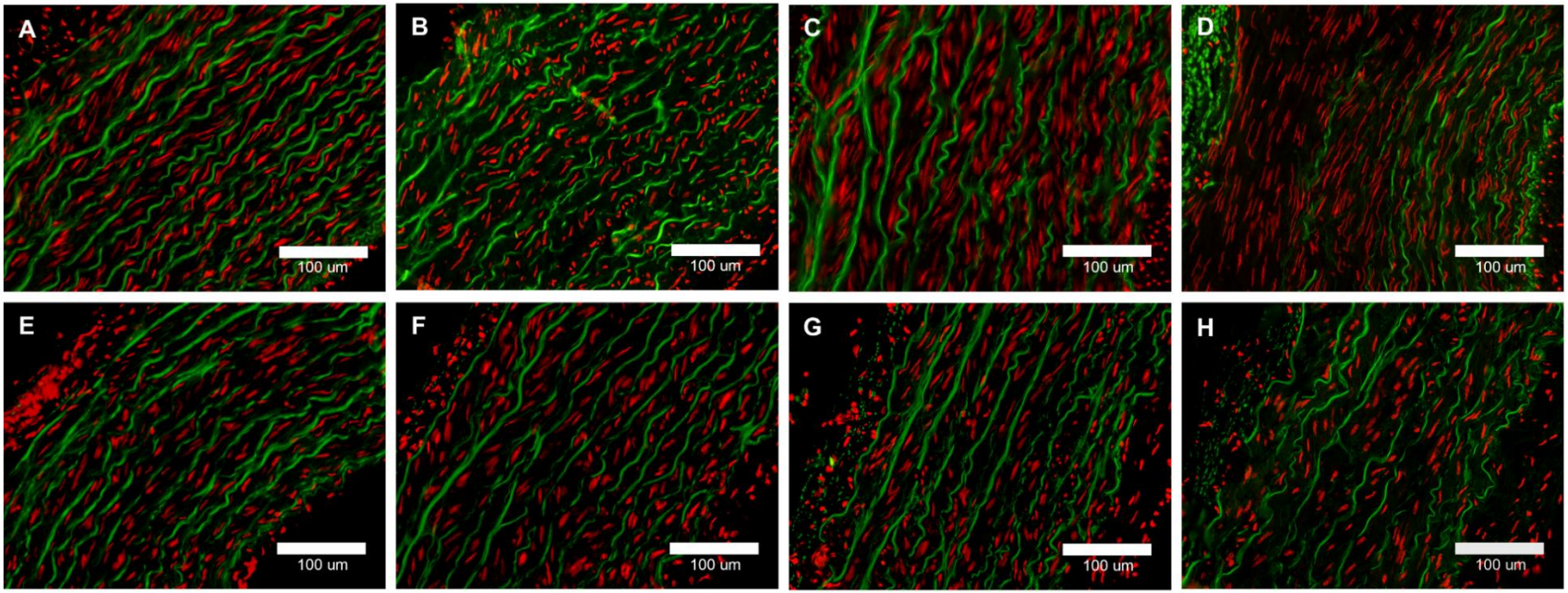

Figure 2.5 - Propidium Iodide nucleic acid stain and elastin autofluorescence LITA [A-D] and RITA [E-H] comparing the medial smooth muscle cell count and elastic lamellar count of the proximal [A & E], submuscular [B & F], middle [C & G], and distal [D & H] segments.

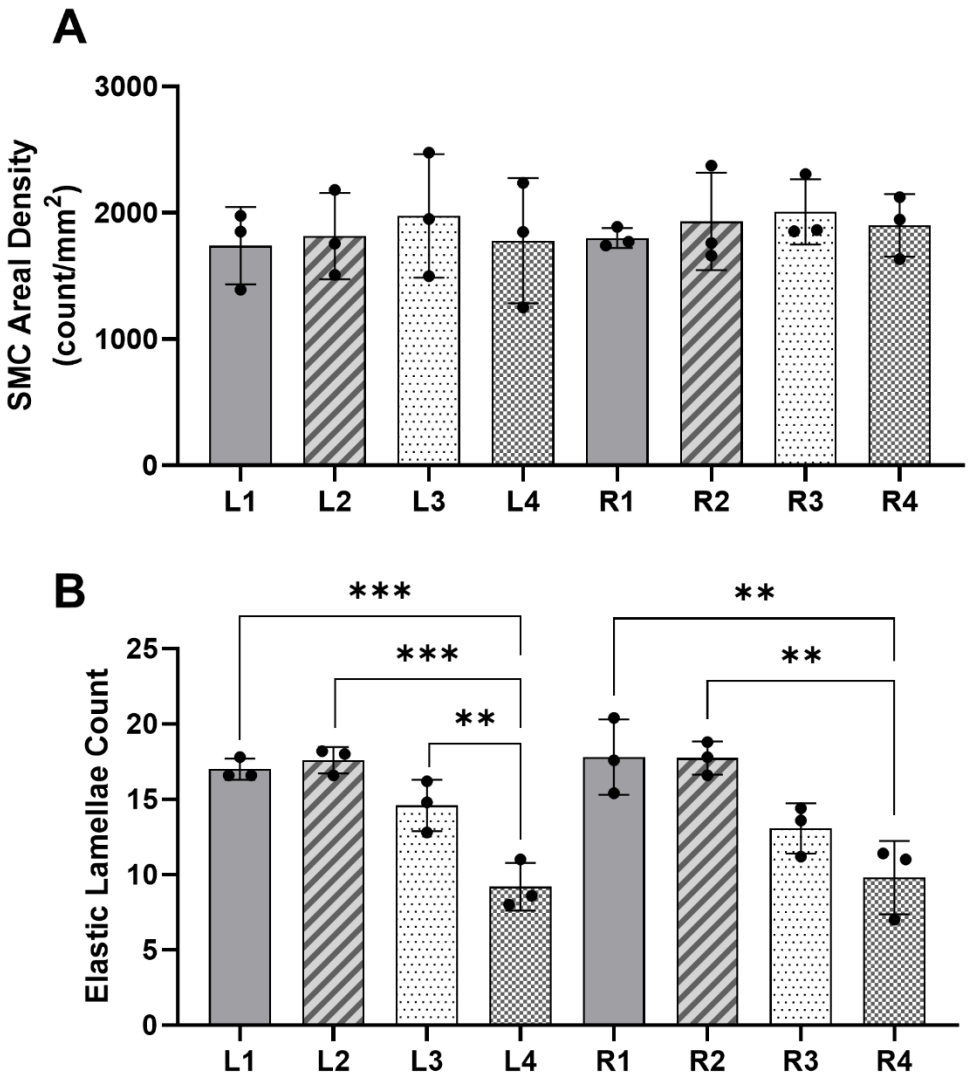

Figure 2.6 - [A] Medial smooth muscle cell density and [B] elastic lamellae count measured from the propidium iodide and elastin autofluorescence cross-sections along the LITA and RITA. Statistical significance is denoted as (*) when $p<0.05$, (**) at $p<0.01$, and (***) at $p<0.001$. Mean ± SD, n=3 for each group.

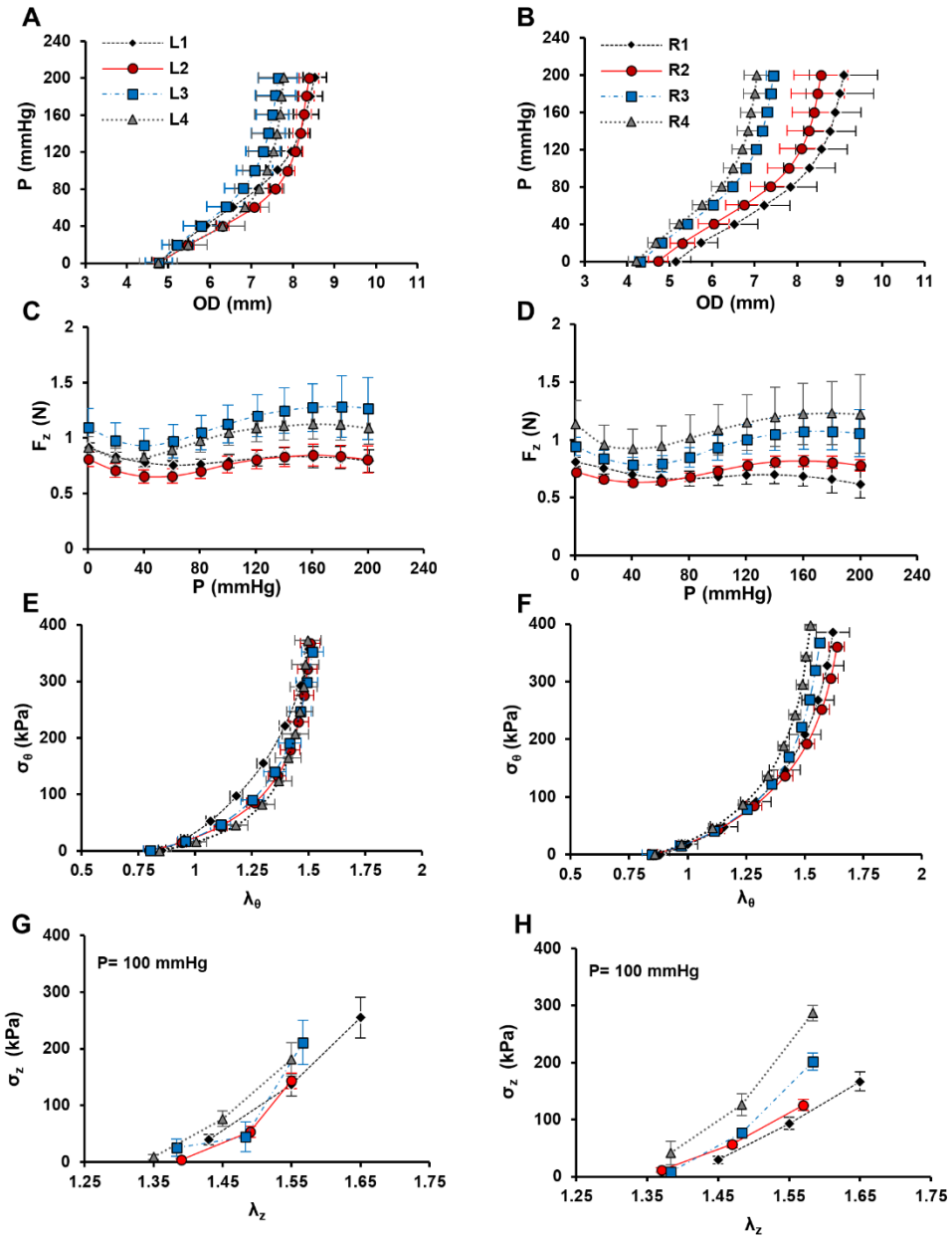

Figure 2.7 - Biaxial mechanical data for LITA [A, C, E, G] and RITA [B, D, F, H]. Pressure-outer diameter [A & B], axial force-pressure [C & D], circumferential stress-stretch [E & F] were all plotted at $\lambda_z = 1.55$. All vessels were tested at axial stretch ratios above and below the one shown but these data were omitted for clarity.

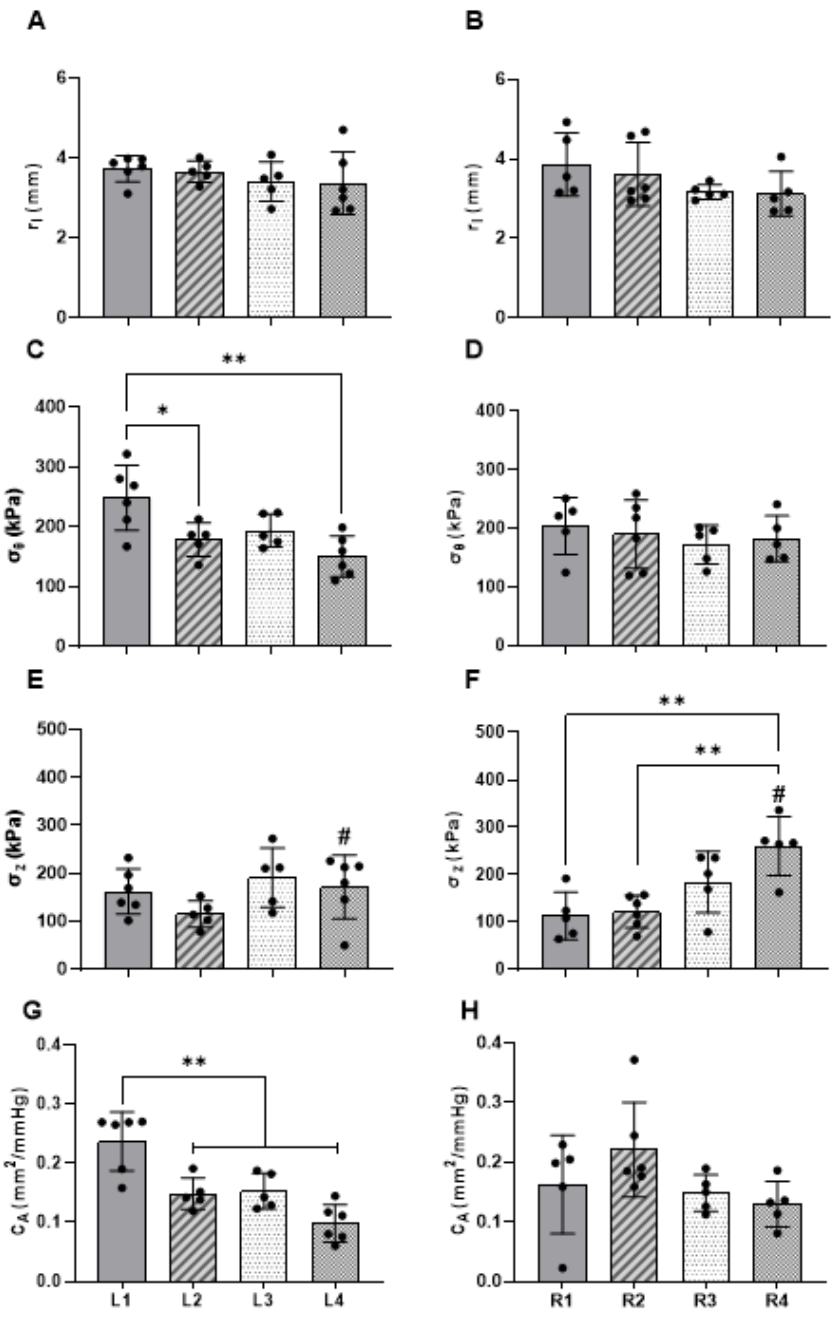

Figure 2.8 - Biaxial mechanical data of LITA [A, C, E, G] and RITA [B, D, F, H] plotted at common loading conditions of 100 mmHg and λ_z = 1.55. Inner radius [A & B], circumferential stress [C & D], axial stress [E & F], and area compliance [G & H] were plotted at the four anatomical segments for each vessel. Statistical significance is denoted as (*) when $p<0.05$, (**) at $p<0.01$, and (***) at $p<0.001$. Statistical significance between the LITA and RITA segments is denoted as (#) at $p<0.05$. Mean ± SD, n=6 for each group.

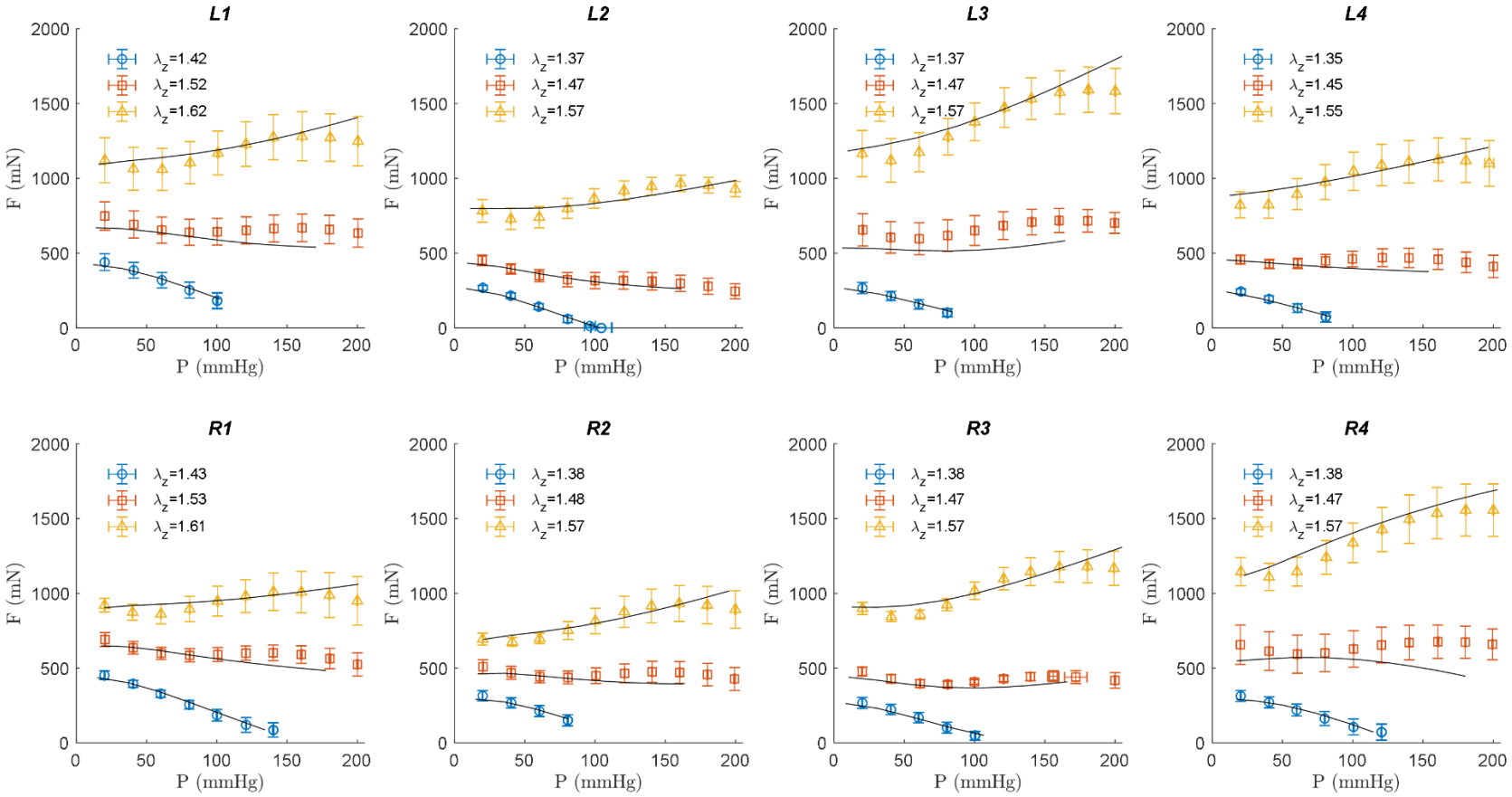

Figure 2.9 - Results of the best fit parameters using the 4-fiber family HGO model (solid lines) to average (n=5-6) experimental pressure-force data (symbols) for the LITA [top] and RITA [bottom] at the three axial stretch ratios. The proximal, submuscularis, middle, and distal segments are shown [left-to-right].

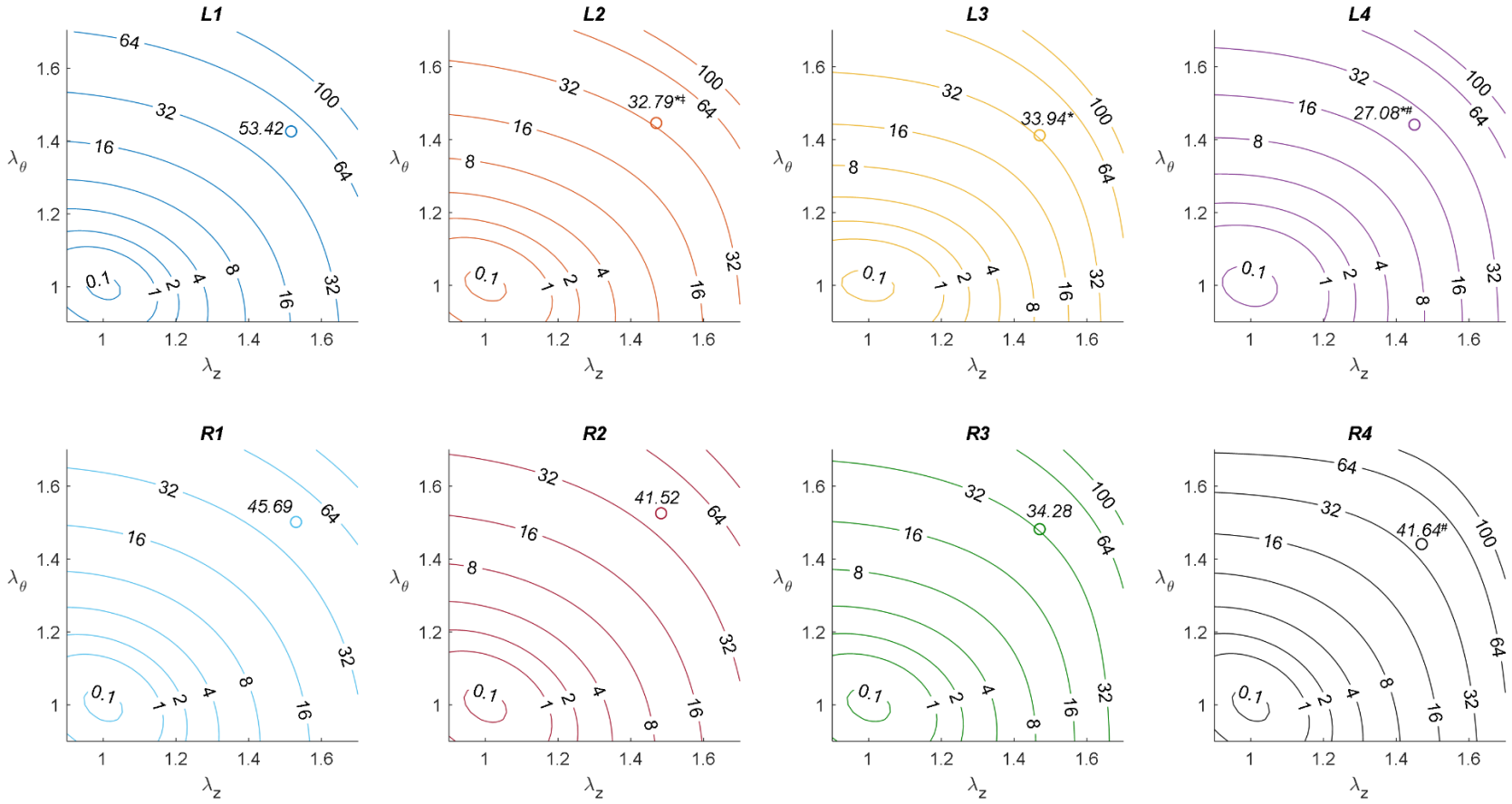

Figure 2.10 - Average strain energy contours (kPa) for the LITA [top] and RITA [bottom] proximal, submuscularis, middle, and distal segments [left-to-right]. Open circles represent approximate *in vivo* values of strain energy at 100 mmHg. Statistical significance is indicated by (*) when found between a given segment and its proximal section, (‡) when found between sequential segments, and (#) when found between the corresponding left and right segments.

46

CHAPTER 3

THE ACUTE MECHANICAL CONSEQUENCES OF SEGMENT-SPECIFIC CORONARY ARTERY BYPASS [2]

[2] Kostelnik, C. J., Gale, M. K., Crouse, K. J., Shazly, T., Eberth J. F.
Under review in *Cardiovascular Engineering and Technology*, 09/01/2022

3.1 ABSTRACT

Premature coronary artery bypass graft (CABG) failure has been linked to geometric, mechanical, and compositional discrepancies between host and graft tissues. Acute hemodynamic disturbances and the introduction of wall stress gradients trigger a myriad of mechanobiological processes at the anastomosis that can be associated with restenosis and graft failure. Although the origins of coronary artery disease dictate the anastomotic target, an opportunity exists for graft-vessel optimization through rationale graft selection. Here we explored the four distinct regions of the left (L) and right (R) ITA (1=proximal, 2=submuscular, 3=middle, 4=distal), and four common target vessels in the coronary circulation including the proximal and distal left anterior descending (PLAD & DLAD), right coronary (RCA), and left circumflex (LCX) arteries. Benchtop biaxial mechanical data was used to acquire constitutive model parameters of these tissues and enable vessel-specific computational models to elucidate the mechanical consequences of 32 unique graft-target combinations. Simulations revealed the maximum principal wall stresses for the PLAD, RCA, and LCX occurred when anastomosed with $LITA_1$, and the maximum flow-induced shear stress occurred with $LITA_4$. The DLAD, on the other hand, reached stress maximums when anastomosed to $LITA_4$. Using a normalized objective function of simulation output variables, we found $LITA_2$ to be the best graft choice for both LADs, $RITA_3$ for the RCA, and $LITA_3$ for the LCX. Although mechanical compatibility is just one of many factors determining bypass graft outcomes, our data suggests improvements can be made to the grafting process through vessel-specific regional optimization.

3.2 INTRODUCTION

Advanced coronary artery disease often requires surgical bypass using autologous vessels to reestablish adequate blood flow to the heart. Despite new surgical techniques, materials, and interventional criteria that have improved overall patency, the first-year failure rates for coronary artery bypass grafting (CABG) remain between 5% and 15% and are strongly dependent upon the source tissue [10, 37, 93]. Vein grafts, for example, suffer from progressive intimal-medial hyperplasia with only a 65% five-year patency rate [94]. Although the etiology of vein-graft disease is multifactorial, due partly to their mechanical composition and microstructure, it has been hypothesized that veins exposed to altered hemodynamic loading induce endothelial cell damage, thrombosis, and fibrosis [95, 96]. Concurrent with this is the concept of structural mechanical mismatching (compliance mismatching) at the anastomotic junction - a location of vulnerability in the grafting process [37, 76, 97, 98] - which is a consequence of both geometrical and mechanical differences between the host and graft tissues [4, 93, 99, 100]. The sudden change in deformed vessel geometry across the anastomotic junction can also cause atherogenic flow disturbances around contraction and expansion points [43, 101] triggering endothelial conformational and functional changes [102, 103]. Likewise, mechanosensitive mural cells that guide regulatory, remodeling, and migratory pathways, may experience altered wall stresses near the anastomotic junction and exhibit an unfavorable cellular response [80, 104, 105]. Overall, graft-host mechanical and geometric mismatching present a major risk of graft failure and restenosis [39, 106].

Arteries, especially the internal thoracic artery (ITA), have been used successfully in bypass grafting; thus, the pathology of artery graft failure has received less attention than

veins. The left (LITA) and right (RITA), for example, possess abundant histomechanical similarities to the left anterior descending artery (LAD), supporting its continued use as the superior autograft option [10, 14, 37, 107]. Moreover, the single anastomotic junction and native hemodynamic similarity improve overall patency. Our recent investigation revealed that the ITA exhibits multiple histological patterns depending on the distance from the heart (i.e., elastic, hybrid, muscular), and can be divided into four distinct anatomical grafting regions (1=proximal, 2=submuscular, 3=middle, 4=distal) [23, 73, 107, 108]. Likewise, coronary arteries and their branches possess distinct regional variations in geometry and microstructure that can change with sex, age, species, and disease conditions [109, 110].

In this study, we quantified the properties of four different coronary artery targets, namely the proximal and distal left anterior descending (PLAD & DLAD), right coronary artery (RCA), and left circumflex artery (LCX), using the American Yorkshire pig as a surrogate for the human central vasculature. Histomechanical results were directly compared to those of the middle LITA segment ($LITA_3$) to serve as a representative sample of ITA architecture [26, 76]. Biaxial mechanical data was used to estimate constitutive modeling parameters using a nonlinear, hyperplastic, structurally motivated material model within a continuum mechanics framework. Leveraging these data, idealized computational models of end-to-end anastomoses with 32 different graft-target (ITA-coronary) combinations were constructed [108]. Finite Element Analyses (FEA) were first used to simulate and perform a "virtual anastomosis" through alignment of the vessel's lumens and attachment of the two tissues. Finally, the resultant deformed geometry was fed into a Computational Fluid Dynamics (CFD) simulation to model fluid-flow behavior. Although

end-to-end anastomosis is not the preferred surgical configuration, computational models were designed to mimic ongoing mechanobiological laboratory experiments and provide an initial indication of source tissue performance. Given that the bypass region (e.g., PLAD, DLAD, RCA, LCX) is dictated by the clinically determined stenosis location, a normalized objective function, based on mechanical deviation from homeostatic stresses, was found for each graft-coronary combination so that the preferred ITA region could be selected for each coronary target.

3.3 MATERIALS AND METHODS

3.3.1 Tissue Acquisition

Porcine coronary arteries and ITAs were acquired from 2-year-old American Yorkshire sows from a local abattoir weighing approximately 200 kg. All arteries were dissected under sterile conditions within 1 hour of slaughter and transported in 1% phosphate-buffered saline (PBS) with heparin sodium (20 units/mL), cleaned, and separated into different groups for histological and mechanical characterization (Figure 3.1). The four coronary arteries included the proximal and distal left anterior descending artery (PLAD & DLAD), right coronary artery (RCA), and left circumflex artery (LCX). Where applicable, and for simplicity purposes, the discrete histological and mechanical data for all coronary arteries were compared to the third segment of the left ITA (LITA). Our previous work revealed this segment had the fewest notable differences from other segments of the left or right ITA [108].

3.3.2 Biaxial Mechanical Testing

All testing was performed on fresh arteries and completed within 48 hours of animal sacrifice. Before testing on our Bose BioDynamic biaxial mechanical testing device,

arteries were cut into 3 cm cylindrical sections, mounted onto two Luer fittings, and fixed in place with 3-0 braided sutures. An initial measurement of the unloaded length was recorded as the distance between sutures, which aided in calculating experimental axial stretch ratios. The tissue samples were submerged in the testing bath and perfused with 1% PBS and sodium nitroprusside (10^{-5} M) to elicit a fully passivated state. Vessels were inflated to pre-defined pressures by increasing the volumetric flow rate and the downstream resistance, per the design of the testing device. Every sample underwent five cycles of axial extension and inflation preconditioning to minimize viscous dissipation and ensure reproducible results. Inflation-extension testing was then conducted at 0-200 mmHg and at three axial stretch ratios, the *in vivo* stretch, and ±10%. The *in vivo* axial stretch ratio was assigned at a force-invariant displacement which yielded a constant axial force measurement during inflation. The luminal pressure and axial displacement were controlled while the deformed outer radius and axial force were recorded.

Following biaxial mechanical testing, a 1 mm thick ring segment was cut from the middle of the vessel and a cross-sectional image was captured. The residual strain in the vessel was removed by making a radial cut and allowing the tissue to equilibrate for 30 minutes in 1% PBS. An image of this zero-stress state was captured using a Canon EOS 60d DSLR camera mounted to a dissecting microscope using an adapter lens (Micro Tech Lab). ImageJ image analysis software (NIH) was used to measure the geometries of both images. The unloaded thickness and opening angle were calculated from

$$H = \frac{2A}{L_i + L_o} \text{ and } \Phi = \pi - \frac{L_o - L_i}{2H}, \tag{1-2}$$

where L_i and L_o are the inner and outer arc lengths, respectively, and A the cross-sectional area. Under the assumption of incompressibility, the inner radius at any deformed state could be calculated as

$$r_i = \sqrt{r_o^2 - \frac{A}{\pi \lambda_z}} \tag{3}$$

where λ_z is the axial stretch ratio. The circumferential and axial stretch ratios can be calculated from

$$\lambda_\theta = \frac{2\pi\left(r_i + r_o\right)}{L_i + L_o} \text{ and } \lambda_z = \frac{l}{L}, \tag{4-5}$$

where l and L are the deformed and undeformed lengths, respectively. Then the average circumferential stress, axial stress, and area compliance are calculated from

$$\sigma_\theta = \frac{P r_i}{r_o - r_i} \text{ , } \sigma_z = \frac{F}{\pi\left(r_o^2 - r_i^2\right)}, \; C_A = \pi \frac{\Delta r_i^2}{\Delta P}, \tag{6-8}$$

where F is the axial force and P the transmural pressure. For compliance, Δr_i is the change in inner radius per change in pressure ΔP calculated around a 100 ± 20 mmHg operating point.

3.3.3 Constitutive Modeling of Experimental Data

The constitutive modeling framework was identical to our previous investigation with extended details and procedures found therein [108]. Briefly, we used the four-fiber-family version of the structurally-motivated constitutive model proposed by Holzapfel, Gasser, and Ogden (HGO) [77, 78] to represent each coronary artery uniquely, so that

$$W\left(\mathbf{C}, \mathbf{M}^k\right) = \frac{c}{2}\left(I_C - 3\right) + \sum_{k=1}^{4} \frac{c_1^k}{4c_2^k}\left\{\exp\left[c_2^k\left(IV_C^k - 1\right)^2\right] - 1\right\}, \tag{9}$$

where $I_C = tr(\mathbf{C})$ and $IV_C^k = \mathbf{M}^k \cdot \mathbf{C}\mathbf{M}^k$ are the first and fourth principal invariants, respectively of the right Cauchy-Green deformation tensor, $\mathbf{C}$. $\mathbf{M}^k = [0, \sin(\alpha^k), \cos(\alpha^k)]$ is a unit vector oriented in the direction of the k^{th} fiber at an angle α^k relative to the axial direction with $\alpha^1 = \mathbf{O}$, $\alpha^2 = \pi/2$, and $\alpha^3 = -\alpha^4$. Assuming relatively small radial stresses, the problem is reduced to plane stress and the theoretical pressure and force calculated from

$$P' = \frac{h}{r_i}\left[\lambda_\theta \frac{\partial W}{\partial \lambda_\theta} - \lambda_r \frac{\partial W}{\partial \lambda_r}\right], \quad F' = \pi h\left(2r_i + h\right)\left[2\lambda_z \frac{\partial W}{\partial \lambda_z} - \lambda_\theta \frac{\partial W}{\partial \lambda_\theta}\right]. \quad (10\text{-}11)$$

The eight-independent positive modeling parameters were then found by least-squares minimization of an objective function between the experimentally measured (equations 6-8) and theoretically modeled (equations 10-11) values of pressure and force using MATLAB's optimization toolbox (MathWorks; Natick, MA).

3.3.4 Computational Modeling

To simulate outputs from both the solid and fluid domains, computational models of each possible grafting configuration were generated for all 32 coronary-ITA combinations in FEBio [111]. The experimentally determined material properties were represented using the available constitutive model for a solid mixture of anisotropic four fiber families embedded in an isotropic ground matrix [77, 112]. Conduit inner diameters were first matched by applying an equal but opposite direction pressure to the inner surface elements at the ends of the respective vessels until a continuous lumen was formed. Then a tied facet-on-facet contact was enforced between the two arteries to serve as a "virtual anastomosis" with approximated geometry. A fixed displacement boundary condition for the z-direction was applied to the non-anastomosed ends of both the graft and coronary

arteries. For simplicity, the virtually anastomosed tissues were studied under a single quasi-static inflation pressure of 100 mmHg. Thus, the previous step's stress history was not carried to the final simulation. The magnitude of the first principal stress (σ_1 – maximum normal stress in a plane oriented to be absent of shear) for each anastomosis was found and plotted versus location along the graft-coronary axis. The displacement tolerance, energy tolerance, and line search tolerance for this solid mechanical FEA model were set to 0.001, 0.01, and 0.9, respectively. The simulation results were deemed mesh-independent if mesh refinement led to less than a 0.5% change in the average first principal stress [113]. A total of 7,680 rectangular elements were required for mesh independence.

The lumen mesh was extracted to build a computational fluid dynamics (CFD) model to simulate steady blood flow through the different graft configurations. Blood was modeled as an incompressible non-Newtonian Carreau fluid (η_0 = 0.25 Pa·s; η_∞ = 0.0035 Pa·s; λ_b = 25; n = 0.25) with a fluid density of 1,060 kg/m3 and zero-slip fluid boundary conditions applied to the outer surface of the extracted geometry representing the interface between the fluid and artery wall [114, 115]. Additionally, a zero fluid dilation boundary condition was applied to the inlet and outlet surfaces. Because direct blood flow measurements were not feasible with abattoir-sourced pigs, published coronary blood flow data from young, healthy domestic swine were used to calculate the volumetric flow of each coronary artery using allometric scaling laws [116]. For simplicity, analyses were performed under steady flow conditions, so the effects of the fluid-solid interface and vessel wall motion were not analyzed. The tissues were then used to predict regional maximum fluid shear stress (τ_w – wall stress due to fluid friction acting opposite to the direction of blood flow) across the anastomoses in the *in vivo*-like loaded condition. The

fluid velocity tolerance, fluid dilatation tolerance, and energy tolerance within the CFD model were set to 0.001, 0.001, and 0.01, respectively. CFD simulation outputs were deemed mesh-independent if additional mesh refinement led to less than a 0.5% change in the average fluid shear stress [113]. A total of 155,159 triangular elements were required to reach mesh independence.

Since blood vessels have a preferred homeostatic or "basal" state of stress, [80, 105] the maximum σ_1 values from the solid mechanical model were normalized to basal coronary σ_1 values taken from biaxial mechanical data captured at the force-invariant axial stretch and 100 mmHg. Likewise, the maximum τw values from the fluid dynamic model were normalized to basal τ_w values. The basal coronary stresses were given a value of 0, and the maximum stresses from each model were given a value of 1 to scale the anastomosis configurations in terms of the most significant deviation from basal coronary stresses (GraphPad Prism).

3.3.5 Histological analysis

Fresh arteries were fixed in 4% paraformaldehyde and embedded in paraffin wax. Sections were cut at 5 μm and stained with Movat's Pentachrome Stain or Picrosirius Red (PSR) Stain. Tissue segments from the same heart were processed together to facilitate a uniform histological comparison of the different coronary arteries. Brightfield images were then obtained using a Nikon E600 microscope and computer interface with Q Capture (QImaging). The PSR stained sections were imaged through brightfield microscopy and polarized light microscopy using a Zeiss AxioCam MCr5. Each arterial cross-section was imaged at five different locations around the vessel's circumference.

Constituent area fractions were obtained using ImageJ software with the "Threshold_Colour" plugin. Movat's Pentachrome stained sections were used to estimate area fractions of elastin and smooth muscle cells (SMCs). On the other hand, the PSR-polarization staining method was used to gather an accurate area fraction of collagen birefringence. The standard threshold values were fixed at specified brightness, saturation, and hue ranges to ensure experimental consistency. Elastin was stained deep red/brown and was quantified using a bandpass filter from brightness 34-155 and saturation 60-255, and a bandstop filter from hue 4-130. SMCs were stained red/pink and were quantified using a bandpass filter from brightness 135-220, saturation 90-185, and hue 0-11. The sums of these areas were normalized to 1 for each sample. Polarized light microscopic analysis of collagen birefringence was quantified for the medial area and the total cross-sectional area. The medial region of interest (ROI) was confined to the inner and outer elastic lamellae area. Total birefringence signal was measured using a bandpass filter from brightness 30-255, saturation 0-255, and hue 0-255. This quantified layer-specific birefringence value accurately estimated the amount and bulk location of collagen for these two arterial tissues.

3.3.6 Statistical Analyses

Experimental data were analyzed using GraphPad Prism to identify statistical significance discrete metrics of $LITA_3$ and the coronary vasculature. Comparisons of the mechanical properties were conducted through a one-way ANOVA in conjunction with a two-tailed paired t-test of unequal variances to determine statistical differences across the arterial samples. The histological data were analyzed through a two-way ANOVA in conjunction with two-tailed paired t-tests of unequal variances to determine statistical

differences between the amounts of load-bearing constituents found within the arterial samples. Statistically significant differences were taken at confidence levels of $p<0.05$, $p<0.01$, and $p<0.001$.

3.4 RESULTS

Plots are displayed for all coronary arteries at their respective force-invariant stretch (middle) as well as ±10% stretch (low, high) (Figure 3.2). The axial force-pressure profiles revealed that the force-invariant stretch for the DLAD was the only artery that maintained a force reading above 0.5 N for the entire experimental pressure range. From this data, the structure-motivated constitutive model revealed a set of best-fit parameters that demonstrated an excellent fit to experimental data (Table 3.1) with an average root mean square error (RMSE) of 0.2405 across all coronary arteries.

Data captured from the stress-free configurations revealed that LITA has significant geometric differences from the coronary arteries (Table 3.2). The LITA outer arc length was significantly larger than the PLAD ($p = 0.039$), DLAD ($p < 0.001$), RCA ($p = 0.001$), and LCX ($p < 0.001$), while the LITA opening angle was significantly smaller than the PLAD ($p = 0.003$), DLAD ($p = 0.021$), RCA ($p = 0.005$), and LCX ($p = 0.004$). Comparing mechanical data at common loading conditions (i.e., 100 mmHg, force-invariant axial stretch) revealed that LITA has a significantly larger loaded inner radius than DLAD ($p = 0.010$), RCA ($p = 0.029$), and LCX ($p = 0.014$) (Figure 3.3A). Similarly, LITA exhibited a significantly larger area compliance ($p < 0.001$) and circumferential stress ($p \leq 0.005$) than all coronary arteries (Figure 3.3B & Figure 3.3C, respectively).

Image thresholding using Movat's Pentachrome stain revealed that the amount of elastin found within the LITA segment was significantly greater than that of all coronary

arteries; PLAD ($p < 0.001$), DLAD ($p < 0.001$), RCA (0.28 ± 0.04, $p < 0.001$), and LCX ($p < 0.001$) (Figure 3.4F). Inversely, the area fraction of smooth muscle cells within LITA was significantly less than that of all coronary arteries; PLAD ($p < 0.001$), DLAD ($p < 0.001$), RCA ($p < 0.001$), and LCX ($p < 0.001$) (Figure 3.4F). Image thresholding of the total and medial birefringence allowed dividing the collagen area fraction into layer-specific values. The adventitial collagen area fraction of the LITA was significantly less than that of all coronary arteries ($p < 0.001$) (Figure 3.5F).

Interestingly, comparisons of the mechanical properties between the coronary vessels revealed few differences. Notably, the circumferential stress of the PLAD was significantly greater than that of RCA ($p < 0.005$), while the DLAD experienced a significantly higher axial stress than the PLAD ($p = 0.001$), RCA ($p = 0.003$), and LCX ($p < 0.001$) (Figure 3.3C & Figure 3.3D). There were no significant histological differences found between any of the coronary vessels.

All tapering simulations converged except the RCA-$RITA_1$, which was omitted from the results. As a representative example, colorimetric FEA model illustrations of σ_1 and τ_w for the PLAD-$LITA_3$ combination are shown in Figure 3.6A and Figure 3.6B, respectively. The spatial plots of σ_1 across the anastomotic junction for all configurations are shown in Figure 3.7; likewise, τ_w is displayed in Figure 3.8. Maximum stresses for each simulation (i.e., the peak values of each curve in Figure 3.7 and Figure 3.8) are collated and reported in Table 3.3. The ITA graft segment that yielded the maximum and minimum stress values for each coronary vessel are highlighted in red and blue, respectively. Notably, for the PLAD, RCA, and LCX, the maximum σ_1 occurred while anastomosed with the $LITA_1$, while the DLAD, on the other hand, was highest when anastomosed to the

$LITA_4$. Likewise, for PLAD, DLAD, and LCX, the maximum τ_w occurred while anastomosed with $LITA_4$, while RCA maximum occurred when connected with $RITA_4$. Finally, the solid and fluid simulation outputs were normalized and averaged to create an objective function relative to the basal coronary stress values. Table 3.4 shows normalized values for each coronary artery in red and blue, respectively, inferring the greatest and slightest degree of deviation from the basal coronary stresses.

3.5 DISCUSSION

Anisodiametric and anisocompliant graft-target tissue combinations have been correlated to increased restenosis rates and premature graft failure [37, 98, 106]. Since the joining of distinctly different tissues creates nonlinearities at the interface with resultant geometries that are not easily solved using standard analytical approaches, we present a histomechanical and computationally-driven objective function to assess the biomechanical responses of the different ITA grafting regions for a given coronary target. Our study provides insight into the inherent differences between these tissues and illustrates the solid mechanical and fluid dynamic consequences that arise in an end-to-end CABG anastomosis configuration.

Not surprisingly, our computational analyses revealed the mechanical response across the anastomotic junction was unique for each ITA-coronary graft combination. Even though our simplified approach uses sutureless and idealized end-to-end anastomoses, the interface still experiences high-stress concentrations due to the abrupt change in geometry and material properties. Moreover, our simulations show the peak stress values occur predominantly on the coronary side of the anastomotic junction, a finding supported by the literature that depicts the suture line as a vulnerable site for the development of intimal

hyperplasia in response to mechanical mismatch with the graft artery [99, 117]. This evidence supports normalizing our solid mechanical simulation outputs to the basal levels of coronary stresses rather than those of the graft tissue. For vein grafts, intimal-medial thickening occurs within the graft tissue itself [94, 118]. However, when these vein grafts were analyzed spatially, 67% developed fibro-intimal thickening, and 33% had an atherosclerotic plaque on the proximal (aortic) side, while 96% showed fibro-intimal thickening and only 4% had an atherosclerotic plaque on the distal (coronary) side [119]. Indeed, several factors play a role in the etiology of regional graft failure, but compatibility with the anastomosing tissue is likely paramount to this process. Still, more attention needs to be given to the spatial pathology of arterio-graft disease.

Although experimental and computational tools of biomechanical analyses (i.e., how biological bodies respond to applied forces or displacements) were used in this study to predict localized stress gradients, the underlying motivation for our work was one of mechanobiology (i.e., how physical loads affect the biological output of cells). That said, the vascular wall cells are accustomed to basal levels or "homeostatic" stresses with chronic perturbations in loading, leading to a restoration of long-term stress [80, 104, 105, 120]. Cellular and tissue level stresses are not zero with resident vascular cells exposed to healthy multi-directional periodic loading *in vivo*. Moreover, emerging evidence supports the idea that the cells of the graft tissue are gradually replaced by the host [121]. For these reasons, basal values of homeostatic coronary vessel stresses were chosen as a baseline for normalization rather than values of the graft tissue. Likewise, regions of low shear are known for atherosclerotic plaque localization and progression, but high shear regions have also been linked to plaque progression/transformation, necrotic core progression, and

increased apoptosis rates [37, 38, 122]. Interestingly, the fluid and solid stress levels found from our computational analysis were an order of magnitude lower in the LAD than the RCA and LCX anastomoses and may be responsible, in part, for the enhanced pathological outcomes in this region [30]. Still, further study into regional pathologies is needed to draw a more robust conclusion.

Even though end-to-end anastomoses are rarely implemented clinically, this configuration demonstrates an axisymmetric stress field, permits clear comparisons of compliance mismatching, and enables direct interpretation of ongoing mechanobiologically-driven experimental assessments such as immunohistochemistry, ELISAs, qPCR, and Western blot analyses. An unfortunate disadvantage is that significant size discrepancies between the graft and host tissues limit potential configurations experimentally and computationally. For example, our tapered computational geometries and facet-on-facet contact restrictions could not be implemented for the RCA-$RITA_1$ combination. End-to-side, spatulated, or even fish-mouth surgical techniques could be performed to circumvent such limitations [33, 106]. These are important for translating the current work into clinical investigations and are part of our ongoing studies. Another notable limitation was the idealized nature of the virtual anastomotic junction. In addition, there was no stress history carried over from the virtual anastomosing process to elucidate local stress gradients that arise solely from intraluminal pressurization. As a common site for surgically-induced vascular injury, the exclusion of sutures or other surgical materials (e.g., vascular clips) from our models allowed for quantification of the solid mechanical and hemodynamic stress gradients that arise solely from the gross biomechanical differences between the graft and target tissues rather than the stress concentrations around

sutures [4, 99, 123]. In fact, suture compliance matching may be as important as tissue compliance matching [4].

Our study depicts the ITA as histomechanically dissimilar from these common bypass coronary targets. The significantly different material and mechanical properties observed within these common bypass graft and target arteries have contributed to para-anastomotic compliance gradients within *in vivo* models [97]. The histomechanical and computational findings from our study depict the proximal and distal portions of the ITA as the worst grafting regions.

3.6 CONCLUSION

Using a porcine surrogate for the human central vasculature our experimental and computational analyses helped provide insight into the importance of graft tissue selection by quantifying the mechanical consequences of an idealized virtual coronary-grafting anastomosis. Based on an objective function used to stratify these tissue combinations for all converged solutions, we found the best ITA graft region for the RCA and LCX was $RITA_3$, and $LITA_3$, respectively, while the best grafting region for both PLAD and DLAD was the $LITA_2$. Vice-versa, the worst ITA grafting region for the PLAD, RCA, and LCX was $LITA_1$, while the worst region for the DLAD was $LITA_4$. This information provides the foundational knowledge necessary for the ongoing investigations of matched and mismatched tissue combinations that will be used to establish a link between mechanobiologically-driven inflammation and thrombosis within mismatched graft-target tissues.

3.7 FUNDING

This research was supported by REU 1852331, CMMI 1760906, and EPSCoR OIA-1655740.

3.8 ACKNOWLEDGMENTS

The authors would like to acknowledge Susan Lessner for access to the Bose mechanical testing device, histological and imaging assistance of the Instrumentation Resource Facility (IRF) at USC School of Medicine, and the computational assistance of Dr. Steve Maas and Dr. Gerard Ateshian.

3.9 TABLES

Table 3.1 - HGO model material parameters for specific coronary arteries

Coronary Artery	c (kPa)	c_1^1 (kPa)	c_2^1	c_1^2 (kPa)	c_2^2	$c_1^{3,4}$ (kPa)	$c_2^{3,4}$	$\propto$ (rad)	RMSE
PLAD	14.702	8.122	1.696	1.564	1.955	1.451	3.025	0.707	0.280
DLAD	10.796	47.867	1.197	1.215	2.231	3.395	2.849	0.666	0.099
RCA	1.278	5.372	1.883	2.905	1.675	4.177	2.310	0.644	0.276
LCX	4.966	4.762	2.605	1.306	2.067	5.493	2.315	0.653	0.307

Table 3.2 - Vessel geometry of the unloaded configurations

Blood Vessel	Unloaded Thickness [H] (mm)	Inner arc length [L_i] (mm)	Outer arc length [L_o] (mm)	Opening Angle [Φ] (°)
PLAD	0.595 ± 0.080	13.026 ± 1.209	12.355 ± 1.112*	218.775 ± 14.058*
DLAD	0.502 ± 0.097	9.750 ± 1.208*	9.599 ± 1.024*	183.756 ± 44.088*
RCA	0.636 ± 0.123	10.866 ± 2.944	10.257 ± 2.365*	204.207 ± 51.170*
LCX	0.504 ± 0.022	9.731 ± 1.141*	9.210 ± 1.192*	216.877 ± 12.129*
LITA	0.512 ± 0.091	14.344 ± 1.385	16.193 ± 2.213	78.931 ± 59.350
* Signifies statistical significance between coronary arteries and $LITA_3$ using one-way ANOVA at $p<0.05$.				

Table 3.3 - Summary of peak simulation outputs from the solid-fluid models of all anastomosis configurations. Maximum values in each group are highlighted in red and minimum values for each group are highlighted in blue. The gray box indicates a computational model that did not converge

Maximum first principal stress [σ_1] (kPa)								
	$LITA_1$	$LITA_2$	$LITA_3$	$LITA_4$	$RITA_1$	$RITA_2$	$RITA_3$	$RITA_4$
PLAD	355.40	185.37	230.64	231.71	181.02	181.45	220.07	293.52
DLAD	403.61	277.01	350.98	441.10	297.39	329.83	340.39	399.78
RCA	1041.24	774.71	714.83	746.61		753.51	655.09	725.84
LCX	892.61	864.45	541.99	632.61	758.23	864.45	507.53	539.10
Maximum wall shear stress [τ_w] (Pa)								
	$LITA_1$	$LITA_2$	$LITA_3$	$LITA_4$	$RITA_1$	$RITA_2$	$RITA_3$	$RITA_4$
PLAD	1.79	1.50	1.58	1.93	1.69	1.63	1.50	1.69
DLAD	2.34	2.31	2.34	2.74	2.45	2.33	2.59	2.59
RCA	10.63	9.71	9.24	10.54		10.84	9.43	11.40
LCX	8.44	8.10	8.07	8.89	8.27	7.76	8.41	7.74

Table 3.4 - Results of the normalized objective function for all anastomosis combinations. Solid-fluid simulation outputs were normalized to basal coronary mechanical and fluid dynamic values and averaged. For each coronary artery, the anastomosis configuration that resulted in the most significant deviation is shown in red, while the smallest is shown in blue

	$LITA_1$	$LITA_2$	$LITA_3$	$LITA_4$	$RITA_1$	$RITA_2$	$RITA_3$	$RITA_4$
PLAD	0.926	0.387	0.529	0.723	0.477	0.447	0.463	0.732
DLAD	0.738	0.460	0.628	1	0.568	0.581	0.719	0.844
RCA	0.952	0.755	0.694	0.792		0.814	0.675	0.834
LCX	0.954	0.862	0.692	0.833	0.869	0.867	0.705	0.657

3.10 FIGURES

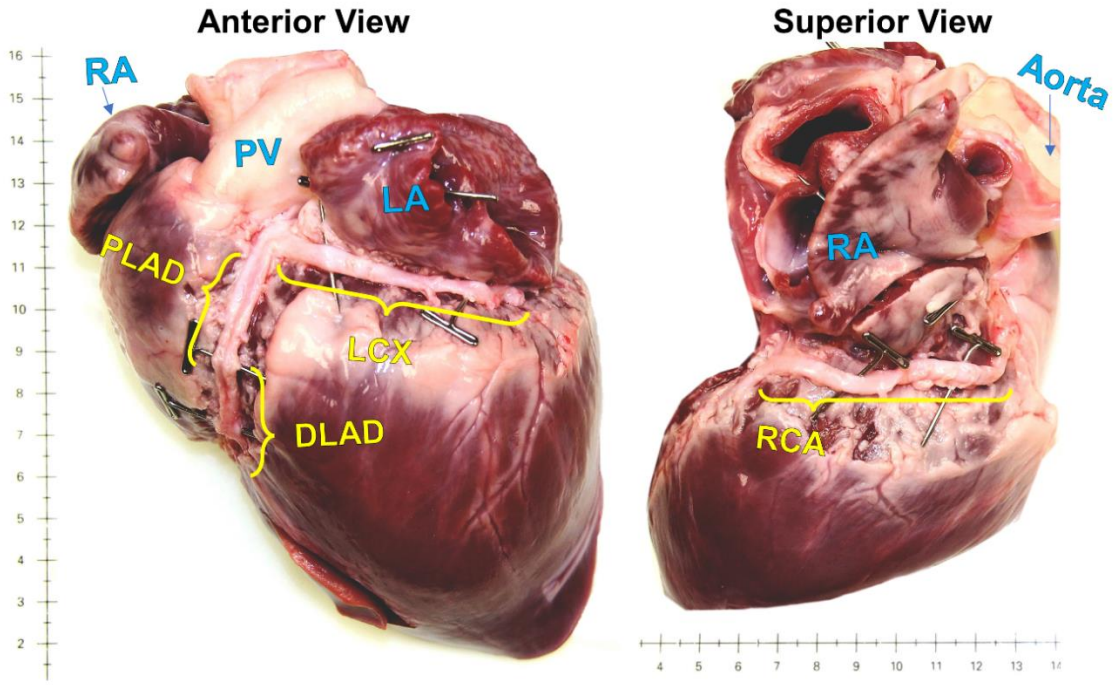

Figure 3.1 - Porcine heart from the anterior and superior view with distinct structures labeled to discern relative sizes and locations of the four coronary arteries of interest. PLAD- proximal left anterior descending artery; DLAD- distal left anterior descending artery; LCX- left circumflex artery; RCA- right coronary artery; RA- right atrium; LA- left atrium; PV- pulmonary vein.

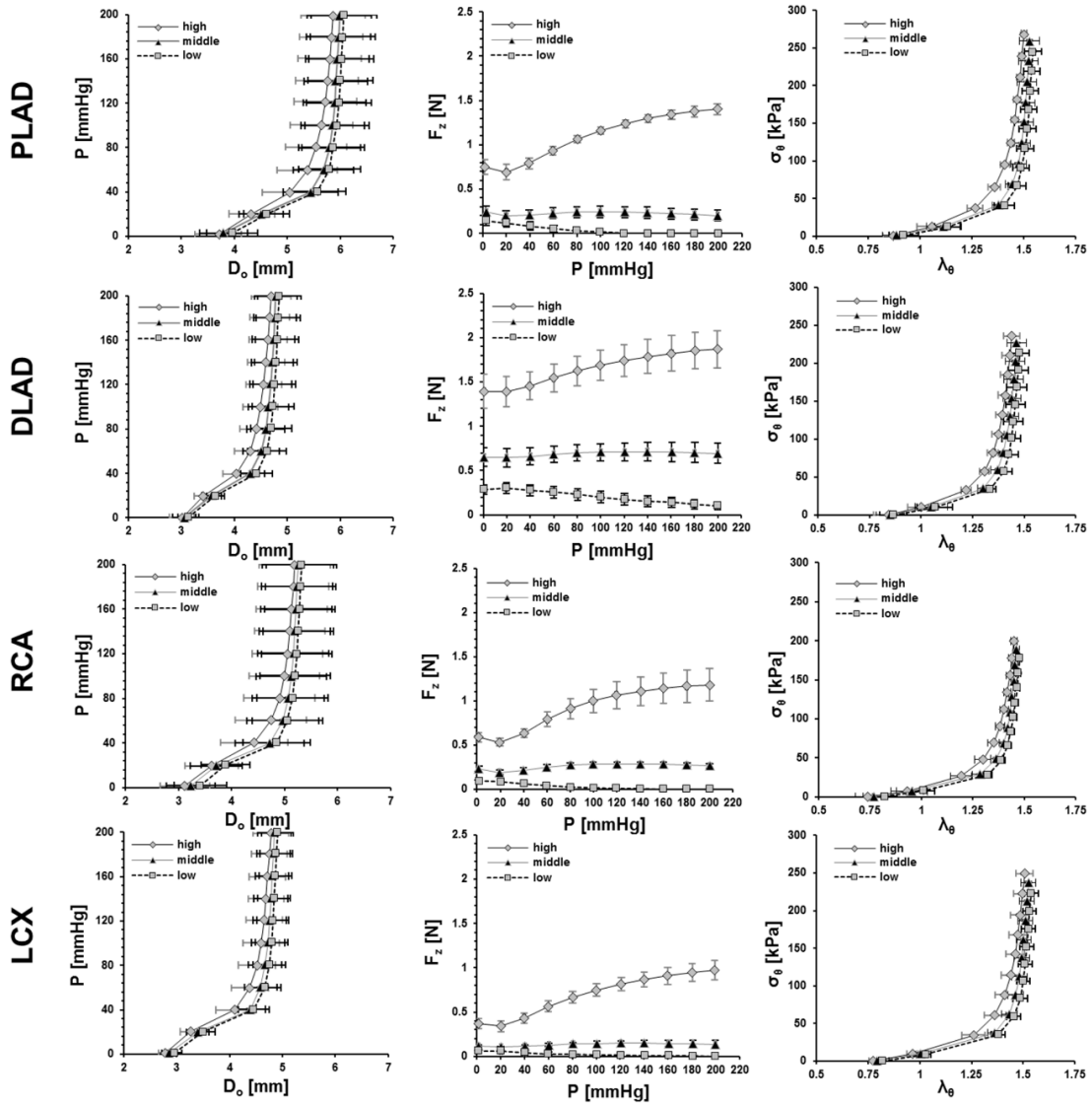

Figure 3.2 - Biaxial mechanical data of the four porcine coronary arteries. The leftmost plots are pressure–outer diameter data, the center plots are axial force–pressure data, and the rightmost plots are mean circumferential stress–mid-wall circumferential stretch data. Data was collected at three distinct stretch ratios, the force-invariant stretch (middle) as well as ±10% strain (low, high). Mean ± SEM, n=4 for each vessel.

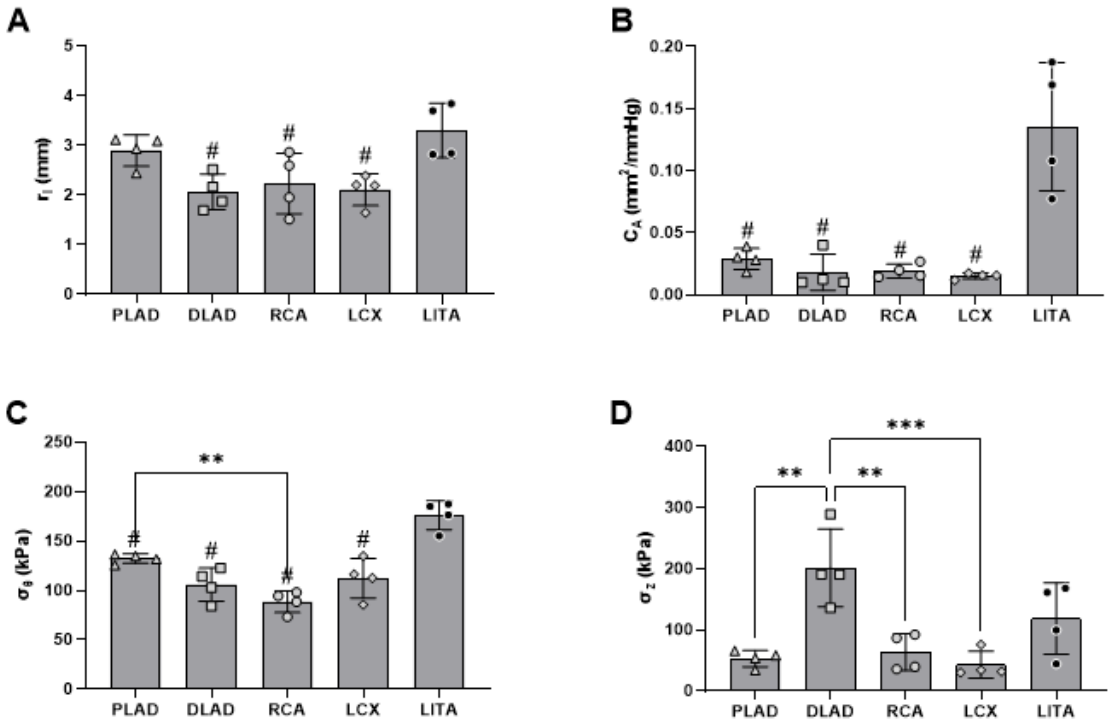

Figure 3.3 - Biaxial mechanical data of porcine coronary arteries and the third LITA segment plotted at common loading conditions of 100 mmHg and at the force-invariant stretch. [A] Inner radius, [B] area compliance, [C] circumferential stress, [D] axial stress. Statistical significance between different coronary arteries is indicated by (**) and (***) at $p<0.01$ and $p<0.001$, respectively. Statistical significance between a coronary artery and LITA is indicated by (#) at $p<0.05$. Mean ± SD, n=4 for each group.

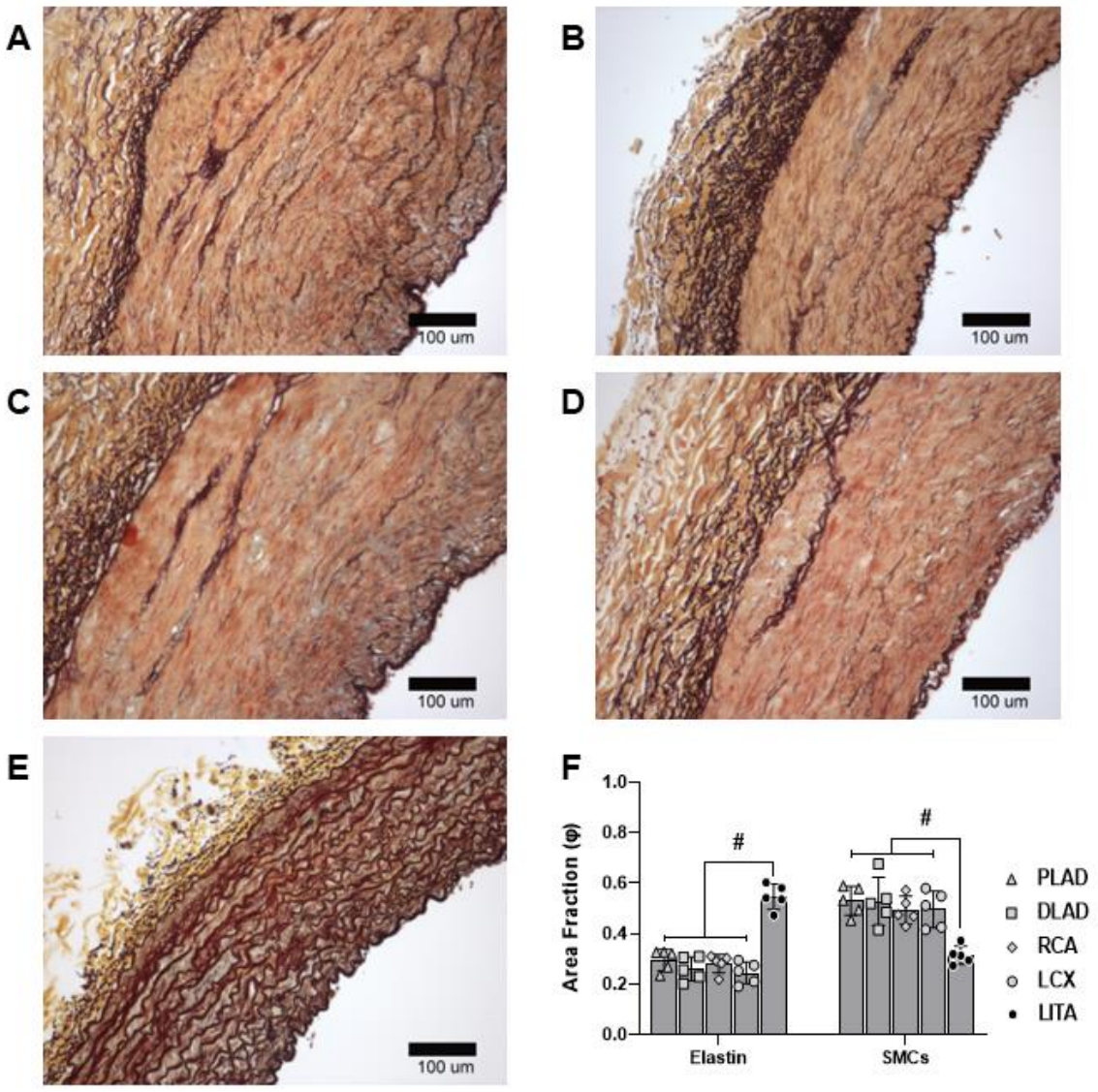

Figure 3.4 - Qualitative and quantitative comparison of arterial wall composition of Movat's Pentachrome stained cross-sections. [A] PLAD, [B] DLAD, [C] RCA, [D] LCX, and [E] the third LITA segment. [F] Quantified area fractions of elastin and smooth muscle cell dyes for all arterial sections. Statistical significance between a coronary vessel and LITA is denoted as (#) at $p<0.05$. Mean ± SD, n=5 for each vessel.

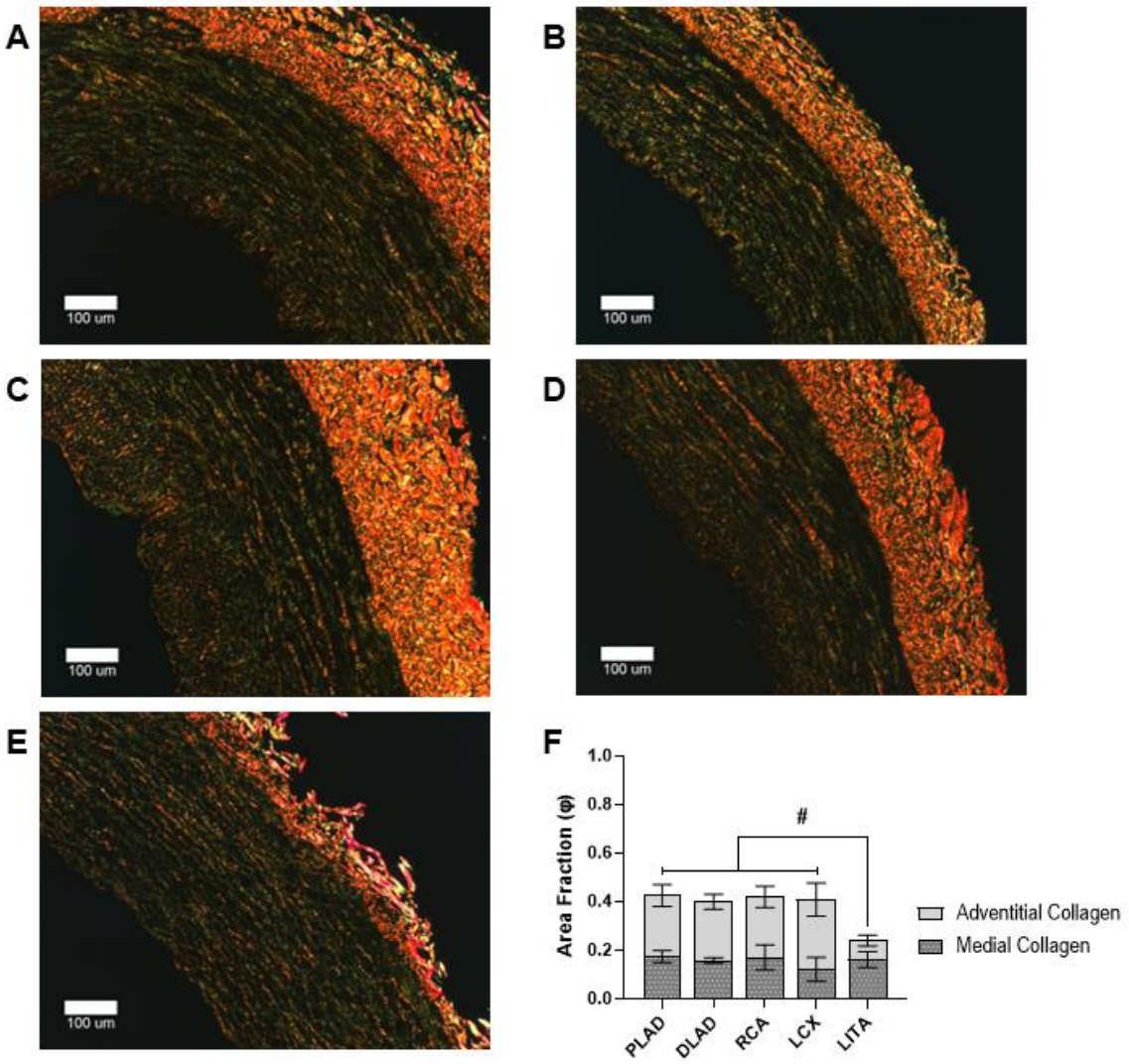

Figure 3.5 - Picrosirius Red stained cross-sections imaged through polarized light microscopy. [A] PLAD, [B] DLAD, [C] RCA, [D] LCX, and [E] the third LITA segment. [F] Quantified area fractions medial and adventitial collagen birefringence. Statistical significance between the adventitial collagen of a coronary vessel and LITA is denoted as (#) at $p<0.05$. Mean ± SD, n=5 for each vessel.

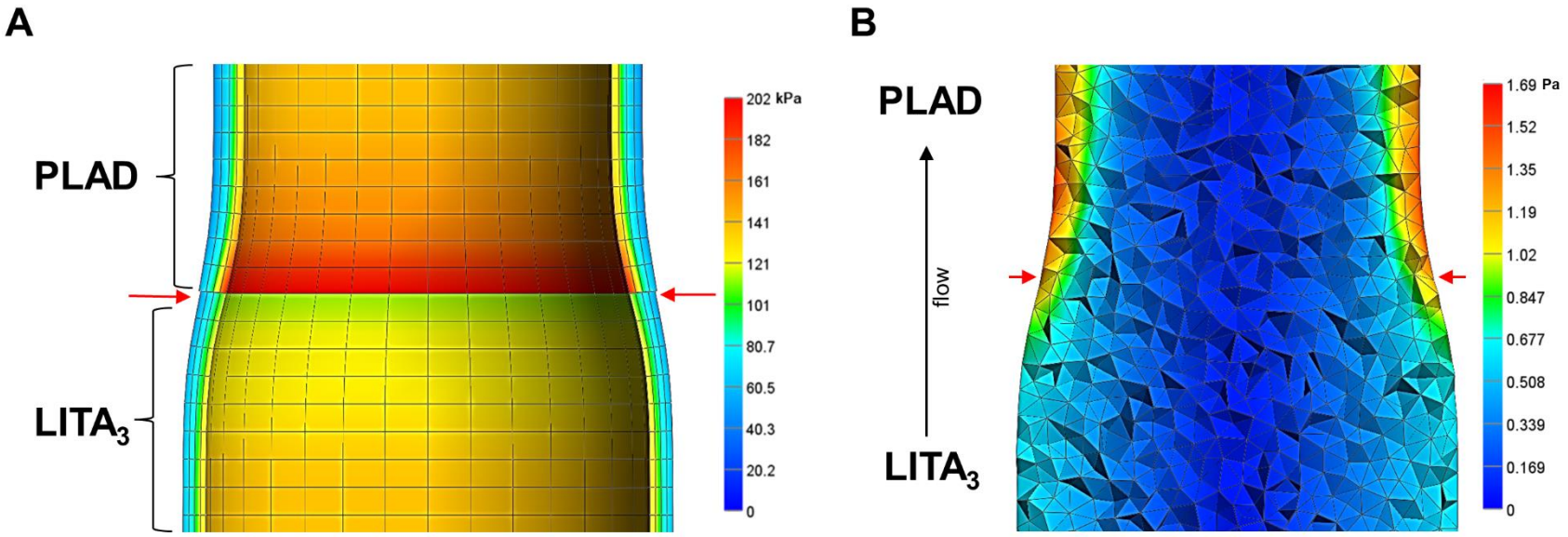

Figure 3.6 - Computational analysis of PLAD-LITA$_3$ end-to-end anastomosis. [A] Colorimetric illustration of first principal stress (σ_1) after inflation from 0 mmHg to 100 mmHg. [B] Colorimetric illustration of fluid shear stress (τ_w) at the inflated configuration. Red arrows depict the contact region representing the anastomosis.

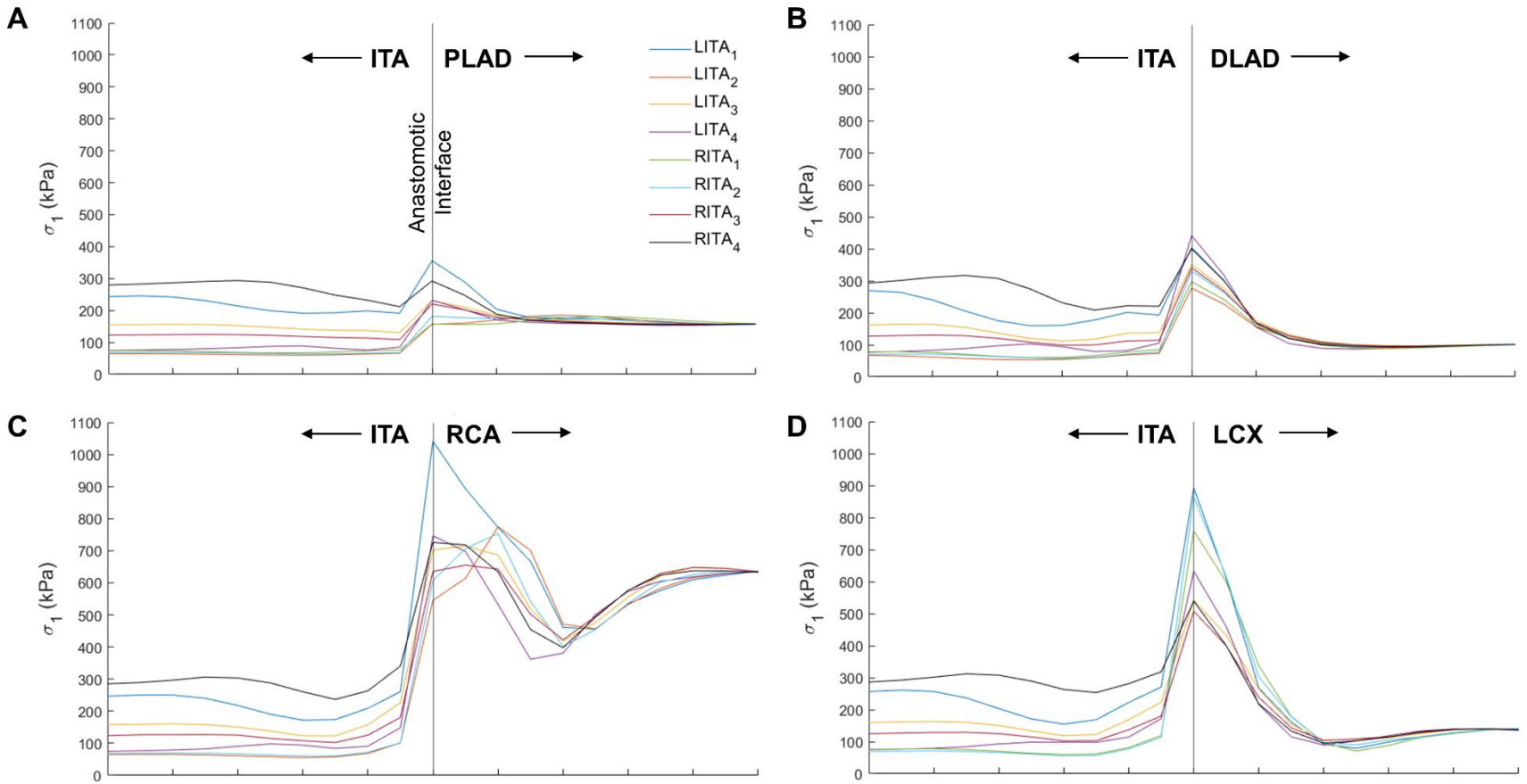

Figure 3.7 - Plots of the first principal stress (σ_1) along the anastomosis for all coronary artery and ITA combinations. The vertical line represents the anastomosis between the two vessels, while the left region of the plot represents the ITA-end, and the right region represents the coronary-end.

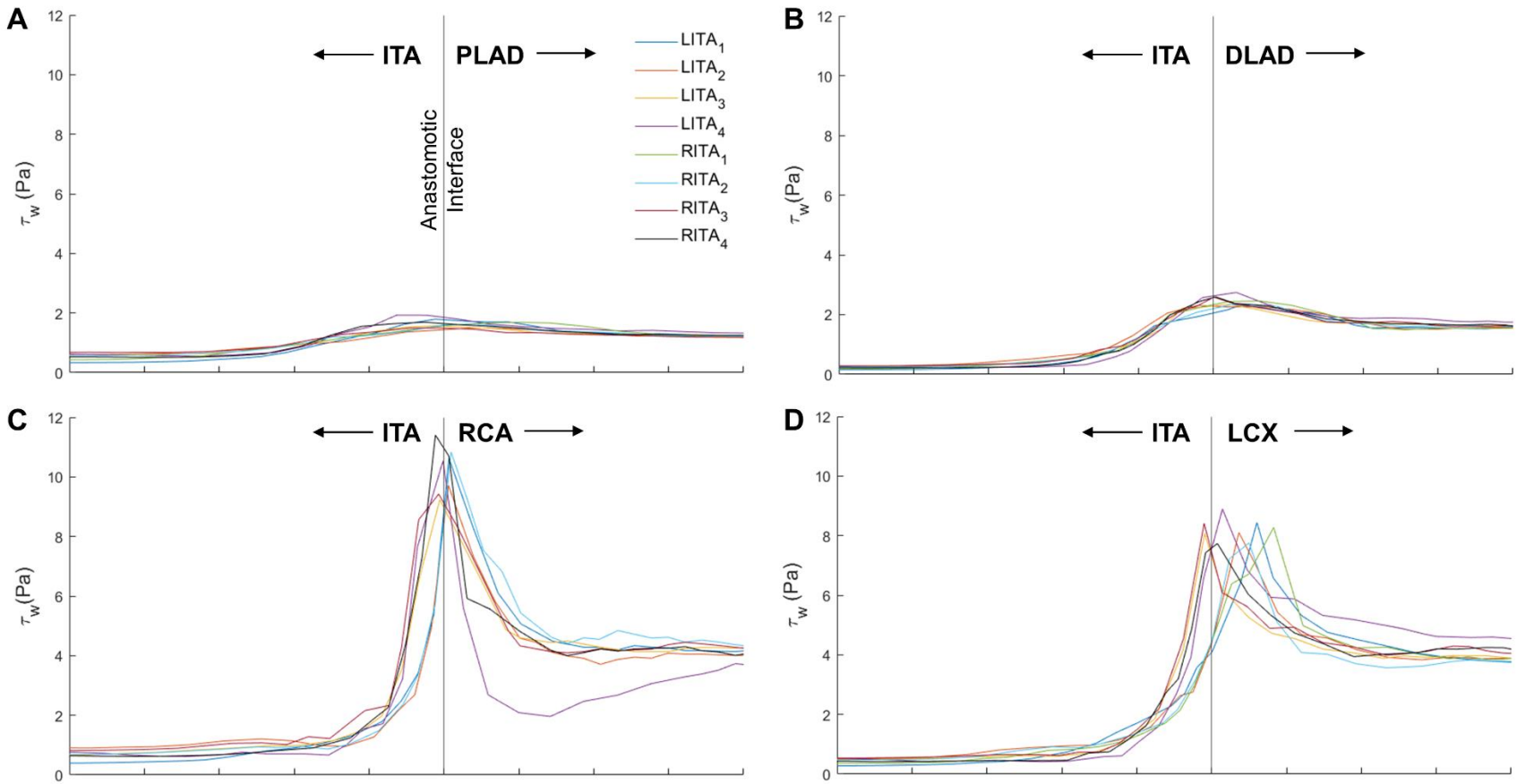

Figure 3.8 - Plots of the maximum fluid shear stress (τ_w) along the anastomosis for all coronary-ITA combinations. The vertical line represents the anastomosis, while the left region of the plot represents the ITA-end, and the right region represents the coronary-end.

CHAPTER 4

SMALL-DIAMETER ARTERY DECELLULARIZATION: EFFECTS OF ANIONIC DETERGENT CONCENTRATION AND TREATMENT DURATION ON PORCINE INTERNAL THORACIC ARTERIES [3]

[3] Kostelnik, C. J., Hohn, J. E., Escoto-Diaz C. E., Kooistra J. B., Stern M., Swinton D. E., Richardson W., Carver, W., Eberth J. F. (2022). *Journal of Biomedical Materials Research Part B: Applied Biomaterials, 110*, (4): 885-897. doi.org/10.1002/jbm.b.34969
Reprinted here with permission of publisher (Appendix A.2)

4.1 ABSTRACT

Engineered replacement materials have tremendous potential for vascular applications where over 400,000 damaged and diseased blood vessels are replaced annually in the United States alone. Unlike large diameter blood vessels, which are effectively replaced by synthetic materials, prosthetic small-diameter vessels are prone to early failure, restenosis, and reintervention surgery. We investigated the differential response of varying 0-6% sodium dodecyl sulfate (SDS) and sodium deoxycholate (SDC) anionic detergent concentrations after 24 and 72 hours in the presence of DNase using biochemical, histological, and biaxial mechanical analyses to optimize the decellularization process for xenogeneic vascular tissue sources, specifically the porcine internal thoracic artery (ITA). Detergent concentrations greater than 1% were successful at removing cytoplasmic and cell surface proteins but not DNA content after 24 hours. A progressive increase in porosity and decrease in glycosaminoglycan (GAG) content was observed with detergent concentration. Augmented porosity was likely due to the removal of both cells and GAGs and could influence recellularization strategies. The treatment duration on the other hand, significantly improved decellularization by reducing DNA content to trace amounts after 72 hours. Prolonged treatment times reduced laminin content and influenced the vessel's mechanical behavior in terms of altered circumferential stress and stretch while further increasing porosity. Collectively, DNase with 1% detergent for 72 hours provided an effective and efficient decellularization strategy to be employed in the preparation of porcine ITAs as bypass graft scaffolding materials with minor biomechanical and histological penalties.

4.2 INTRODUCTION

A major challenge confronting the field of regenerative medicine and tissue engineering is the design, fabrication, and validation of suitable scaffolds that direct the repair and regeneration of damaged tissues [124–126]. Advanced biomaterials including hydrogels, membranes, micro/nanofibers, and micro/nanoparticles have emerged as innovative platforms for tissue engineering purposes [127–129]. New generation biomaterials and novel technologies are making substantial headway into the engineering of complex tissue scaffolds. This is in part due to the ability to modulate the composition and microarchitecture of these materials to improve biocompatibility, promote desirable cellular events, and optimize degradation kinetics and mechanical properties. Advances in biomaterials are making the engineering of replacement tissues a reality; however, several hurdles remain before this technology reaches its full potential. These hurdles are particularly evident in the application of tissue-engineered blood vessels as a platform for coronary and peripheral bypass grafting procedures. With approximately 400,000 annual bypass surgeries annually in the United States alone, there is a pressing need to optimize replacement blood vessels for grafting procedures [130, 131].

Autografts are the preferred choice in small-diameter vascular bypass procedures due to their biocompatibility and lack of thrombogenicity [132]. However, they are inherently limited by the number of bypasses and any chronic pathological conditions that impact tissue patency such as atherosclerosis or diabetes. Prosthetic grafts or patches (e.g., Dacron or expanded PTFE) have been implanted in large numbers of patients over the past several decades and these are relatively effective for the repair of large arteries such as the aorta. However, these prosthetic grafts are limited for use in bypass procedures because an

increased rate of infection and thrombotic events have been detected when used as small-diameter blood vessel replacements [133, 134]. Decellularized blood vessels have gained popularity as a biomimetic scaffold by harnessing innate tissue-specific properties to direct cellular functions including differentiation and proliferation while inducing a minimal immune response [135–137]. Such scaffolds can be created from human or animal tissues and are a low-cost and readily available platform for tissue engineering. In their native form, decellularized scaffolds are mechanically-robust but extracellular matrix materials can also be solubilized and reconstituted into infinite size/shape configurations and tailored to the functional demands of the specific tissue [51, 138–140].

Effective decellularization of blood vessels can be achieved through physical, chemical, or enzymatic processes, however, each has unique limitations and disadvantages such as the presence of residual chemicals or enzymes and the destruction of essential extracellular matrix (ECM) proteins.[141–143] Chemical decellularization, for example, has been successfully achieved through the use of anionic detergents such as sodium dodecyl sulfate (SDS) and sodium deoxycholate (SDC). These homogeneously disrupting surfactants solubilize cell membranes by inducing curvature stress and thinning the hydrophobic core of the membrane [144]. Additional decellularization methodologies have combined different detergents or other chemical agents with enzymes to effectively target both the cell membrane and nuclear material [55, 136]. Enzymes including proteases and nucleases are advantageous in decellularization protocols because of their substrate specificities; however, exposure to some enzymes at high concentrations or for prolonged periods can damage collagen or significantly reduce the glycosaminoglycan (GAG) content [55, 145, 146]. These materials play a vital role in the mechanical properties of blood

vessels which are deterministic in graft procedure outcomes [10]. Likewise, the analysis of comprehensive biaxial properties (i.e., inflation-extension) from a consistent material and anatomical location is fundamental to the efficacy of this biomaterial [108] and deviations in host-graft properties lead to atherosclerotic and inflammatory promoting perturbed flow profiles, shear stresses, and stress concentrations at the anastomosis site [147].

Many tissue-engineered decellularization strategies that fail to preserve the biochemical and biomechanical properties of native tissues possess poor cell repopulation and differentiation rates [148]. Assuming that the optimal decellularized vascular graft retains properties similar to its native configuration but in the absence of immunogenic materials, the present studies were aimed at systematically evaluating the effects of anionic detergent concentrations and treatment durations on decellularization potential. Using the porcine internal thoracic artery (ITA) as a novel but well-characterized match for a graft target in the coronary circulation, the biochemical, histological, and mechanical properties of these tissues following enzymatic-detergent decellularization was analyzed to determine if there were meaningful modifications of these decellularized scaffolds. Our findings contribute to the broader field of tissue engineering and xenograft development for applications in vascular bypass grafting.

4.3 MATERIALS AND METHODS

4.3.1 Arterial Decellularization

Adult porcine ITAs were obtained from a local abattoir and transported to the laboratory in phosphate-buffered saline containing antibiotics (100 units/mL penicillin, 100 mg/mL streptomycin, 1 mg/mL amphotericin-B, and 10 ng/mL gentamicin). Due to variations in the structural and mechanical properties along the length of the porcine ITA

[108], vessels were separated into proximal and distal halves with only the proximal half used in this study. Vessels were cut into 3 cm lengths, placed into 50-mL conical tubes, and rinsed in three changes of PBS for 10 minutes each on a rotator at room temperature (20 revolutions per minute) to remove any residual blood. Vessel pieces were then incubated overnight in PBS (control group) or distilled water on a rotator at 4°C (the control sample was incubated in PBS for the duration of experimental treatments). Following overnight incubation, the samples were rinsed in PBS twice for 20-30 minutes each. The samples were incubated again overnight in DNase 1 (Roche Diagnostics cat# 10104159001) at a final concentration of 1 mg/mL in DNase digestion buffer (10 mM Tris (pH 7.4), 2.5 mM $MgCl_2$, 0.5 mM $CaCl_2$) on a rotator at 4°C. Samples were subsequently rinsed twice for 20-30 minutes in PBS. Rinsed samples were placed in a detergent solution composed of equal concentrations of SDS and SDC [149]. Detergent concentrations included: 0% SDS and SDC (hereafter referred to as 0% detergent), 0.5% SDS plus 0.5% SDC (hereafter referred to as 1% detergent), 1% SDS plus 1% SDC (hereafter referred to as 2% detergent), 1.5% SDS plus 1.5% SDC (hereafter referred to as 3% detergent) and 3% SDS plus 3% SDC (hereafter referred to as 6% detergent). Samples were incubated in the respective detergent concentrations for 24 or 72 hours at room temperature on a conical tube rotator. All solutions for decellularization contained antibiotics to mitigate contamination. Although the nuclease-detergent sequence used in our study differed from previous reports, [52, 150–152] additional experiments were performed in our lab to test DNase application before or after detergents or when omitted from the protocol (n=8 to 12 per group) [143, 149]. Our findings (Supplemental Section) revealed similar residual DNA

concentrations irrespective of enzyme-detergent order but were significantly less than when DNase was omitted from the protocol altogether.

4.3.2 DNA Quantification

Control and decellularized vessels were homogenized in DNAzol Reagent (Thermo Fisher Scientific) and the genomic DNA was precipitated from the lysate with ethanol. Then the DNA was solubilized in 8 mM sodium hydroxide. Quantitative measurements of the total DNA content were then determined by the Quant-IT PicoGreen dsDNA Assay Kit (Invitrogen), following the manufacturer's specifications.

4.3.3 Western Blot Analyses

Biochemical analyses were carried out to assess the relative loss of cytoplasmic (α-smooth muscle actin), cell surface (β1 integrin), and basement membrane (laminin) components during the decellularization protocols. Samples were pulverized in liquid nitrogen and incubated in RIPA solution (150 mM sodium chloride, 1% Triton X 100, 0.5% deoxycholate, 0.1% sodium dodecyl sulfate, 1.5 mM ethylenediaminetetraacetic acid, 50 mM Tris, pH 8.0) containing Pierce Protease Inhibitor Mini-Tablets (Thermo Fisher Scientific). Samples were incubated at 60°C for 10 minutes and were mixed by inversion three times during incubation. Samples were then centrifuged for 20 minutes at 20,000 g (4°C). Supernatants were then moved to new tubes and total protein concentration was determined with the Pierce BCA (bicinchoninic acid) protein assay (Thermo Fisher Scientific).

Proteins were separated by sodium dodecyl sulfate-polyacrylamide gel electrophoresis (SDS-PAGE) and transferred to nitrocellulose. Nitrocellulose was rinsed in tris-buffered saline containing 0.05% TWEEN 20 (TBS-T) and blocked in TBS-T

containing 5% powdered milk. Nitrocellulose was rinsed in TBS-T and incubated overnight with validated primary polyclonal antibodies against α-smooth muscle actin (Abcam, #ab5694), laminin (Abcam, #ab11575) and β1 integrin (Sigma-Aldrich, #ab1952). The α-smooth muscle actin and laminin primary antibodies were used at a dilution of 1:500 and β1 integrin at a dilution of 1:1,000 in TBS-T containing 1% powdered milk. After three washes in TBS-T, nitrocellulose was incubated in 1:10,000 HRP-conjugated anti-rabbit IgG (Sigma-Aldrich) secondary antibody for 1-2 hours. Following additional rinses in TBS-T, immunoblots were developed with the Pierce SuperSignal Western blot detection reagent (Thermo Fisher Scientific) and exposed to x-ray film. Protein standards were used to provide a reliable molecular weight estimation of the protein signals on the transferred blots. The films were scanned using Adobe Photoshop and signals were quantified using Alpha Innotech software.

4.3.4 Scanning Electron Microscopy

Samples were obtained by cutting approximately 5 mm cross-sectional segments from each vessel/scaffold. Samples were fixed in McDowell Trump's fixative for 2 hours followed by rinsing in PBS (3 x 15 minutes) and ultrapure water (3 x 10 minutes). Samples were dehydrated via a graded ethanol series as follows: 15 minutes in 35%, 50%, and 75% ethanol; 2 x 15 min in 95% ethanol; and 3 x 30 minutes in 100% ethanol. Samples were then immersed in fresh hexamethyldisilazane (HMDS) twice for 15 minutes. HMDS was decanted, and samples were left to dry overnight. Samples were then mounted to allow imaging of the vessel wall in cross-section, gold sputter-coated, and imaged on a JEOL JSM-1610PLUS/LA SEM. At least two representative regions of each sample were

imaged. The effects of experimental treatment on the generation of spaces within the samples were analyzed from SEM images using the NIH ImageJ program.

4.3.5 Histology and Immunohistochemistry

Approximately 2 mL cross-sectional slices of the treated vessels were fixed overnight at 4°C in 4% paraformaldehyde prepared in PBS. Fixed vessels were rinsed in PBS, processed for paraffin embedding, and sectioned at approximately 5 μm. Tissue sections were stained with 4',6-diamidino-2-phenylindole (DAPI) to analyze DNA content, Picrosirius Red (PSR) to assay collagen, and Verhoeff-Van Gieson (VVG) stain to assess elastic fibers. For quantitative analyses, eight random photomicrographs were taken circumferentially around the blood vessel wall. The effects of decellularization treatment parameters were quantified using the NIH ImageJ program.

DAPI Staining

The fluorescent stain, DAPI, was used to evaluate the DNA content of control and decellularized tissue sections. The histological sections were heated in a hybridization oven at 60°C for 10 minutes, deparaffinized in xylene, and rehydrated through a descending alcohol series (100% 95%, 70%). Tissue sections were rinsed twice for 10 minutes each in PBS then incubated in DAPI (1:1000 dilution) in the dark for 30 minutes at room temperature. The sections were subsequently rinsed twice in PBS for 20 minutes each. For quantitative analysis, eight random photomicrographs were taken circumferentially around the vessel wall on a Nikon E600 fluorescence microscope at an exposure time of 2.5 ms. The effects of the decellularization treatment parameters on DAPI-positive content were quantified using the ImageJ program from the NIH.

Picrosirius Red Staining

Picrosirius Red (PSR) stain was used to evaluate the vascular collagen content of control and decellularized tissue sections. Histological sections were heated to 60°C in an incubator for 45 minutes and deparaffinized using xylenes, a descending alcohol series (100%, 90%, 70%), and a brief 1-minute bath in distilled water. The sections were stained with 0.2% Phosphomolybdic Acid and then rinsed in distilled water. The sections were then stained with PSR (12 g Picric Acid, 400 mL water, 0.4 g Sirius Red) followed by incubation in 0.1 M HCL. Ascending alcohol (70%, 90%, 100%) and xylene series were used to dehydrate the sections. The sections were mounted with Depex. The stained sections were imaged and the collagen volume was determined as previously described.34

Verhoeff-Van Gieson staining

Verhoeff-Van Gieson stain was used to evaluate elastic fiber content of control and decellularized tissue sections. Histological sections were heated at 60°C in a hybridization oven for 30 minutes and then deparaffinized using xylenes and a descending alcohol series (100%, 95%, and 70%). The sections were rinsed in distilled water twice, followed by incubation with Working Elastin Stain (10 mL Hematoxylin Solution, 1.5 mL Ferric Chloride Solution, 4 mL Weigert's Iodine Solution, 2.5 mL deionized water) for 10 minutes. Following incubation, the sections were rinsed in distilled water and differentiated in Working Ferric Chloride Solution (3 mL Ferric Chloride Solution and 37 mL distilled water) for 1-2 minutes. The sections were sequentially rinsed briefly in tap water, 95% alcohol to remove the iodine, and deionized water. After this rinse, the sections were stained with Van Gieson for 1-3 minutes. They were again rinsed in 95% alcohol, dehydrated in xylene, and coverslipped. The stained sections were imaged, and the vascular elastic fiber density was determined using ImageJ.

4.3.6 Biochemical Quantification of Glycosaminoglycan Content

A dimethylmethylene Blue (DMMB) assay was used to evaluate the sulfated-glycosaminoglycan (s-GAG) content within treated ITA samples. The tissue samples were dried in glass tubes at 65°C overnight in a hybridization oven and the dried tissues were weighed. Tissues were digested with papain (Invitrogen cat# 10108014001) made in papain extraction buffer (400 mg Sodium Acetate, 200 mg EDTA, 40 mg Cysteine HCl – added to 50 mL 0.2 M NaH2PO4) overnight at 65°C. The liquid was transferred to Eppendorf tubes and centrifuged for 10 minutes at 10,000 g (4°C). Aliquots of each sample were added to DMMB Reagent (16 mg DMMB, 3.04 g Glycine, 1.6 g Sodium Chloride, 95 mL 0.1 M Acetic acid – for 1L). s-GAG concentrations were determined by comparison to a standard curve using a BioRad Benchmark Plus Microplate Spectrophotometer at 525 nm.

4.3.7 Collagen Quantification

A hydroxyproline assay was used to biochemically evaluate the collagen content within the treated ITA samples. Small pieces of tissues were dried overnight at 60°C and subsequently, dry weights were obtained. Tissues were digested overnight at 60°C with papain (Invitrogen cat# 10108014001 30 units/mg). Samples were subsequently incubated at 120°C in 4N NaOH for 15 minutes. Samples were returned to room temperature and 4N HCl was added to each sample to neutralize the pH. Chloramine-T solution (0.05 M Chloramine-T, 0.629 M NaOH, 0.140 M Citric Acid, 0.453 Sodium Acetate, 0.112 M Acetic Acid – in 74% water/26% 2-Propanol) was added to each sample and the sample was incubated at room temperature for 20 minutes. Ehrlich's Reagent (1 M DMAB in 30% HCl/70% 2-Propanol) was added and the samples were incubated at 65°C for 20 minutes.

The reaction was quenched by immersing the tubes in cool water and samples read on a BioRad Benchmark Plus Microplate Spectrophotometer at 550 nm. Hydroxyproline concentration was determined by comparison to a standard curve created from purified collagen.

4.3.8 Biaxial Mechanical Testing

The mechanical properties of the fresh, control, and decellularized ITAs were found through biaxial inflation-extension testing using a Bose BioDynamic mechanical testing device following protocols described in [108]. The tissue sections were trimmed to comply with the testing device's 10 mm maximum displacement range, mounted onto two luer-fittings, and then fixed in place with 3-0 braided sutures. Then tissues were submerged in a testing bath and perfused with 1% PBS and sodium nitroprusside (10^{-5} M) to elicit a fully passivated state [87]. The "*in vivo* axial stretch ratio" was found by axial stretching the vessel to a point that yielded a constant axial force value in response to pressurization. Every decellularized tissue sample then underwent five cycles of extension and inflation preconditioning to minimize viscous dissipation and ensuring reproducible results. For data collection, all vessels were inflated from 0 to 200 mmHg while measurements of force, axial stretch, and outer diameter were collected every 20 mmHg at the *in vivo* axial stretch ratio as well as 10% above and below that value.

Immediately following biaxial testing, a 1 mm thick ring segment was cut from the middle of the tested vessel and a cross-sectional image was captured. The residual strain in the vessel was removed by making a radial cut and allowing the tissue to equilibrate for 30 minutes in 1% PBS. An image of this zero-stress state was captured using a Canon EOS 60d and ImageJ image analysis software was used to measure the geometries of both

images. This configuration enables calculation of wall thickness H and opening angle Φ so that,

$$H = \frac{2A}{L_i + L_o} \text{ and } \Phi = \pi - \frac{L_o - L_i}{2H} \tag{1-2}$$

where L_i and L_o are the inner and outer arc lengths of the open ring segment, respectively. The cross-sectional area A was found by calculating the difference between the area within the outer wall and the luminal area of the intact ring segment before introducing the stress-relieving cut. The biaxial inflation-extension apparatus controlled the luminal pressure P and axial displacement while measuring the outer diameter and axial force F at 20 mmHg pressure increments for three axial displacements. Under the assumption of tissue incompressibility, the inner radius r_i could be found at any deformed configuration given that

$$r_i = \sqrt{r_o^2 - \frac{A}{\pi \lambda_z}} \tag{3}$$

where r_o is the outer radii and λ_z the axial stretch ratio. The axial and circumferential λ_θ stretch ratios are then easily calculated via

$$\lambda_z = \frac{l}{L} \text{ and } \lambda_\theta = \frac{2\pi\left(r_i + r_o\right)}{L_i + L_o} \tag{4-5}$$

with l and L, the deformed and undeformed lengths, respectively. The average circumferential σ_θ and axial σ_z stresses were (see also Prim et al. 2018):

$$\sigma_\theta = \frac{P r_i}{r_o - r_i} \text{ and } \sigma_z = \frac{F}{\pi\left(r_o^2 - r_i^2\right)}, \tag{6-7}$$

where P, is the luminal pressure and F the axial force. Finally, the area compliance was represented by

$$C_A = \pi \frac{\Delta r_i^2}{\Delta P} \tag{8}$$

where Δr_i and ΔP were measured around a 100 mmHg operating point.

4.3.9 Statistics

Comparisons of the histological images, SEM images, and the mechanical properties between the anionic detergent concentrations and controls were made via one-way ANOVA. Data were imported into Prism GraphPad for statistical analyses. Statistically significant differences were taken at a level of $p<0.05$.

4.4 RESULTS

4.4.1 Decellularization Efficacy

The effects of anionic detergent (SDS and SDC) concentration and treatment duration on decellularization efficiency were evaluated by staining of tissue sections with DAPI to assess DNA content (Figure 4.1). Treatment of porcine ITAs with DNase 1 followed by anionic detergents for 24 hours resulted in substantial residual DAPI-positive material in the scaffolds that were not statistically different from untreated controls (Figure 3.1A). Unlike control samples, however, the DAPI-positive material was no longer in compact nuclei form but was more diffusely organized. Anionic detergent treatment for 72 hours resulted in essentially undetectable DAPI staining (Figure 4.1B) with no significant difference between the concentrations of anionic detergent. The PicoGreen assay also failed to reveal significant differences in DNA concentration for any groups after only 24 hours (Figure 4.1E). The 72 hour treatment, however, resulted in a significant decrease in the measured DNA concentration between all treated and untreated controls (Figure 4.1F) with no significant differences between the detergent concentrations. To further evaluate

decellularization efficiency and to examine differential effects on specific tissue components (i.e., cytoplasmic, cell surface, and extracellular matrix), western blot analyses were carried out of tissue lysates following the treatment process (Figure 4.2). For these experiments, western blots were performed of representative cytoplasmic (α-smooth muscle actin), cell surface (β1 integrin), and basement membrane (laminin) proteins. Quantitative assessment was not performed due to a lack of normalization control. Despite this limitation, it was clear that the inclusion of high concentrations of an anionic detergent (2-6%) effectively removed cytoplasmic and cell surface proteins after 24 and 72 hours of treatment. After 24 hours of detergent treatment, a high concentration of laminin was still detected in the tissue lysates, but this diminished substantially following 72 hours of treatment.

4.4.2 Analysis of Scaffold Structure

Scanning electron microscopy was performed to analyze the effects of anionic detergent concentration and treatment duration on the structure of resulting scaffolds (Figure 4.3). Treatment of porcine ITAs resulted in the formation of void space or pores between extracellular matrix fibers in the tunica media. At 24 and 72 hours, the area fraction of void space within the tissue (porosity) was significantly greater in the samples treated with detergent compared to the non-detergent treated samples (Figures 4.3C and 4.3D). For the 24-hour detergent treatment, the highest doses of detergent (3 and 6%) created a significantly greater porosity when compared to the lower doses (1 and 2%). This difference was no longer apparent at 72 hours of treatment and all detergent doses were statistically the same.

4.4.3 Analysis of Extracellular Matrix Content

To assess the effects of anionic detergent concentration and treatment duration on the vascular ECM, various assays qualitatively measured the collagen, elastin, and s-GAG content. Overall collagen content was inferred by analyzing the hydroxyproline content for all experimental groups, while collagen distribution and area fraction were evaluated histologically with picrosirius red staining. There was substantial heterogeneity in the effects of detergent treatment on collagen content with both assays (Figure 4.4). Due in part to the level of variability, there was no significant effect of detergent concentration and treatment duration on the overall collagen content (Figure 4.4). Through quantitative analysis of the VVG staining, it is evident that there was no significant effect of detergent concentration nor treatment duration on elastic fiber content (Figure 4.5). Interestingly, there was a trend towards increased elastic fiber density following treatment for 24 or 72 hours with higher concentrations of detergent suggesting compaction of elastic fibers due to the removal of cells or other components. The most notable alteration to the vascular ECM was the significant reduction in s-GAG concentration with all decellularization treatments compared to the control samples (Figure 4.6). Reduction in s-GAG concentration was also seen in samples only treated with DNase 1 (0% detergent).

4.4.4 Analysis of Scaffold Biomechanical Properties

Inflation and extension biaxial tests were performed to quantify the physical characteristics of the scaffolds and used to determine how anionic detergent concentrations impacted the vascular wall mechanical properties. All specimens were tested at common axial stretches to facilitate comparisons between groups. Overall, the control and fresh vessels exhibited similar mechanical properties and the presence of detergents impacted

the slope of the stress-strain curve (stiffness) but in a concentration-independent manner (Figure 4.7). That is, the presence of anionic detergents had some effect, but no obvious trends emerged between the varying concentrations on mechanical properties. When the anionic detergent treatment duration was increased to 72 hours the tissue appeared to exhibit a more compliant stress-strain profile. Comparing the structural and mechanical properties at common loading conditions revealed a significant increase in circumferential stress and circumferential stretch for tissues treated with 1% detergent for 72 hours relative to the control group (Figure 4.8). Similarly, short treatment durations of high detergent concentrations (6% detergent) exhibited a significantly higher axial stress value in comparison to the control group. Conversely, a significant decrease in the area compliance was observed between tissues treated with 6% detergent and the DNase enzyme only (0% Det) treated sample. The area compliance value of the ITA sample treated with 1% detergent for 72 hours was elevated, albeit insignificantly, above all other samples (Figure 4.8). Data taken from cross-sectional images and stress-free ring sector images reported a statistically significant difference between the wall thicknesses of the 6% detergent sample and the fresh tissue that was biomechanically tested immediately after harvest (Figure 4.9).

4.5 DISCUSSION

Decellularized vascular xenografts present a promising platform for small-diameter tissue-engineered blood vessel replacements [53, 81]. A variety of physical, biological, and chemical methods have been used in the past to decellularize diverse tissues and organs [142, 143, 153, 154]. Yet each of these methods, although largely effective at the removal of cellular material, can negatively impact the ECM microarchitecture limiting the tissue's inherent biophysical qualities. Starting with a novel but well-characterized match for the

coronary vasculature [108] we chose the porcine ITA as a decellularization starting point and assessed the effects of varying DNase and anionic (SDS and SDC) detergents in a time-dependent manner. Our immersion-based chemical decellularization procedure retained tissue in an unloaded configuration to help minimize loading effects on the existing microarchitecture. Our findings suggest that DNase and 1% anionic detergent for 72 hours is the most effective strategy at removing cellular material while minimizing the consequences to the vessel's histoarchitecture.

The ITA composition has been characterized as an elastic and musculoelastic artery, depending on the relative distance from the heart [26, 73, 108]. Heterogeneous distribution of elastin and collagen fibers influences the vascular wall mechanics and highlights the importance of donor tissue selectivity [108, 132]. Histomechanical similarities exist between the ITA and the left anterior descending artery (LAD), with both arteries exhibiting similar compliance and a higher amount of elastin than other common autograft tissue sources [10]. This histomechanical graft-target matching plays a vital role in long-term patency. Our investigation of decellularized ITAs revealed similar histological, mechanical, and morphological properties to their native state. Xeno-bioprosthetics are favorable as a scaffold for cell repopulation due to the consistency of microstructural protein networks across mammalian species [51, 92]. Conservation of key biomechanical properties such as mean circumferential stress, mid-wall circumferential stretch, and mean axial stress across several species further supports the use of xenogeneic tissue sources as future grafting scaffolds [92].

Others have shown that low concentrations of anionic detergents can effectively remove cellular material from vascular tissue with minimal residual detergent retention.[142, 143] Analysis of the cellular content in our vessels revealed that the porcine ITAs retained DAPI-positive material even after 24 hours of treatment with high levels of anionic detergent treatment. This was undetectable when the treatment duration was extended to 72 hours. The quantified residual DNA concentrations using PicoGreen for both treatment durations align well with the DAPI image thresholding. This result supports our findings that nuclease and low anionic detergent concentration treatment for 72 hours was preferred over 24 hours for removing significant nuclear material. An acknowledged limitation of the current study is that we did not optimize the concentrations of SDS and SDC detergents independently. Moreover, our nuclease-detergent sequence was different than other studies [52, 150, 151]; however, DNase is often omitted entirely from decellularization protocols [143, 149]. Still, qualitative analysis of cytoplasmic and surface proteins confirmed that 24 hours of detergent treatment removed a large amount of cellular material while 72 hours showed a significant decrease of the cellularity of all detergent groups in a concentration-independent manner. However, extending the treatment duration to 72 hours reduced the basement membrane protein laminin in the scaffolds. This reduction in laminin may have adverse effects on the recellularization of scaffolds as vascular cells readily adhere to this protein and coating decellularized prostheses with laminin enhances recellularization [155]. Although we did not test it directly, another risk of increasing detergent concentration and time is the potential for cytotoxic detergent retention, which would limit future recellularization efficacy.

Although we performed a complete mechanical characterization via state-of-the-art biaxial testing protocols using matched tissue segments, very few of the metrics used for mechanical comparison reached statistical significance. Others have shown that decellularized arteries are significantly stiffer than native tissue through uniaxial tensile testing, but these studies do not assess how decellularization impacts the multidirectional loading of these arteries [156]. A decrease in the cellularity of these engineered tissue constructs is accompanied by a decrease in cell-ECM fiber interactions. It is noteworthy to point out that longer decellularization treatment durations resulted in more compliant stress-strain profiles relative to the control group. Others have observed that extended physical decellularization procedures can significantly reduce the maximum tensile strength and Young's modulus of small-diameter vascular tissue via uniaxial ring extension [157]. We believe the compliant response seen with prolonged detergent-based decellularization procedures (>24 hours) may be due in part to greater disruption to the ECM fiber network, decreased fiber-fiber interactions, or collagen denaturation and structural changes [142, 156, 158].

Analysis of the constituent makeup of the decellularized ITAs did not reveal significant differences in the two major load-bearing proteins, namely collagen and elastin, following anionic detergent and DNase treatments and explain the preservation of relevant mechanical metrics. However, there was a significant decrease in cellular material and s-GAG content and an inversely proportional increase in tissue porosity with detergent and DNase treatments that are consistent with other research groups [55, 145]. Retention of these ECM proteins throughout the decellularization process is crucial for maintaining tissue integrity and providing attachment points for recellularization. Although we did not

test differentially for collagen type IV compared to other types, the persistence of collagen overall and the retention of laminin at short treatment durations suggests a high potential for recellularization. We hypothesize that the recellularization process would be enhanced by the increased porosity of the tissues during culture as cells and nutrients would diffuse more readily throughout the matrix; however, the increase in porosity also presents swelling concerns and a potential site for residual detergents [141–143]. Likewise, the DNase enzyme-detergent sequence used in our study could influence the retention of residual detergents [152]. Never-the-less, it is also worth noting that the removal of constituents resulting in increased porosity has a moderate effect on the wall thickness and therefore limits the utility of the incompressibility assumption employed during biaxial testing. The porosity-compressibility relationship, therefore, needs to be further disambiguated in future studies.

Decellularized xenografts have shown potential as coronary and peripheral bypass candidates that could help alleviate donor tissue limitations. This novel tissue source was chosen based on widespread availability, relative size in comparison to human vascular tissue, and because other porcine vessels (e.g., carotids) are popular amongst xenograft studies. More importantly, the native histomechanical features closely match those of the coronary vasculature thus our optimization processes are aimed at retention of these features. In our study, short-term (24 hours) detergent treatments in conjunction with DNase failed to remove sufficient nuclear material, however, prolonged (72 hours) resulted in adequate decellularization even when using low concentrations of anionic detergents (1% detergent). Collectively these findings suggest that low detergent concentrations for

72 hours can be used in future decellularization strategies but at the cost of altered mechanical properties and laminin retention.

4.6 CONCLUSION

The combination of enzymatic and anionic detergent decellularization of porcine ITAs revealed the removal of cellular content proceeded in a time-dependent and concentration-independent manner. Significant differences in tissue composition and structure were found through a combination of qualitative and quantitative analyses of histology, electron microscopy, and biaxial mechanical testing. These differences can be used to optimize the decellularization process of xenogenic vascular tissue and may contribute to the development of an acellular scaffold used to investigate cellular repopulation and tissue remodeling.

4.7 FUNDING

This work was funded by grants from the National Science Foundation (EPSCoR OIA-1655740, CMMI 1760906) and the National Institutes of Health (R21 EB022131).

4.8 FIGURES

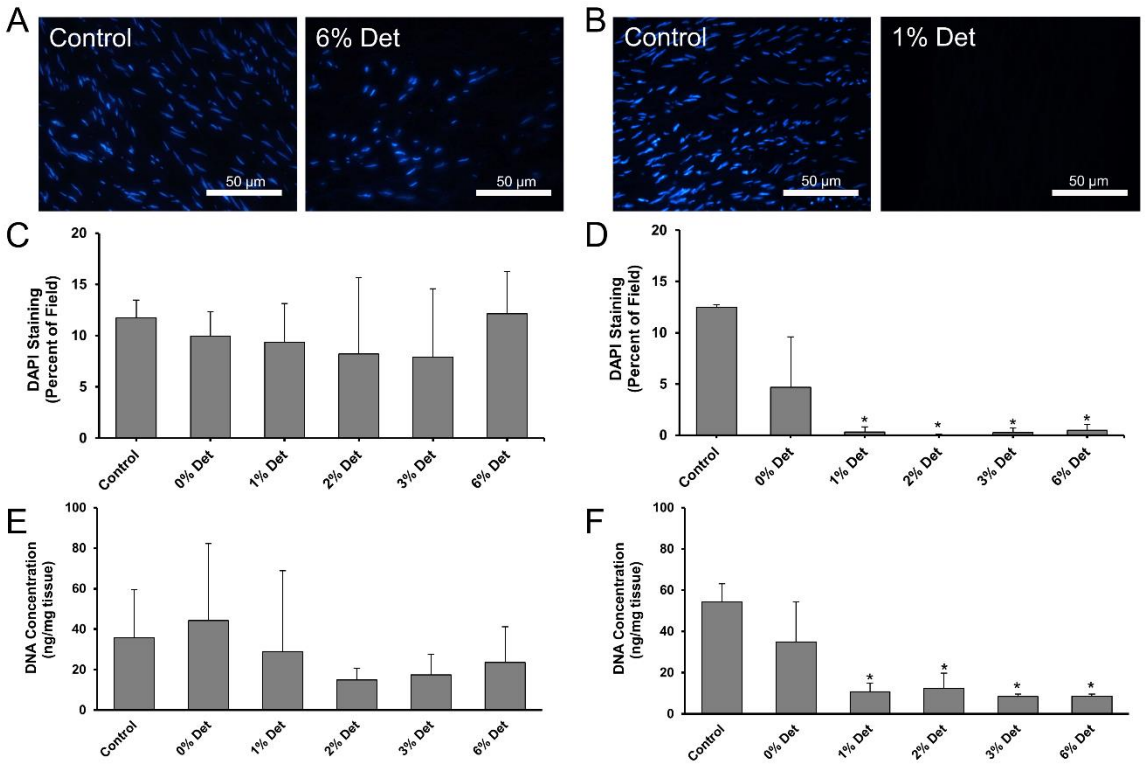

Figure 4.1 - DAPI nuclear stain and quantification of DNA content following [A] 24 hours and [B] 72 hours of anionic detergent treatment. The insets are representative images of DAPI-stained sections of control, 6% detergent-treated, and 1% detergent-treated tissues at respective time points. Area fraction quantification of DAPI positive pixels for [C] 24 hours and [D] 72 hours. Quantified DNA concentrations from the PicoGreen assays for [E] 24 hours and [F] 72 hours. Statistical significance between detergent concentrations relative to untreated controls was determined by one-way ANOVA and is indicated by (*) at $p<0.05$. Mean ± SD, n=4 for each group.

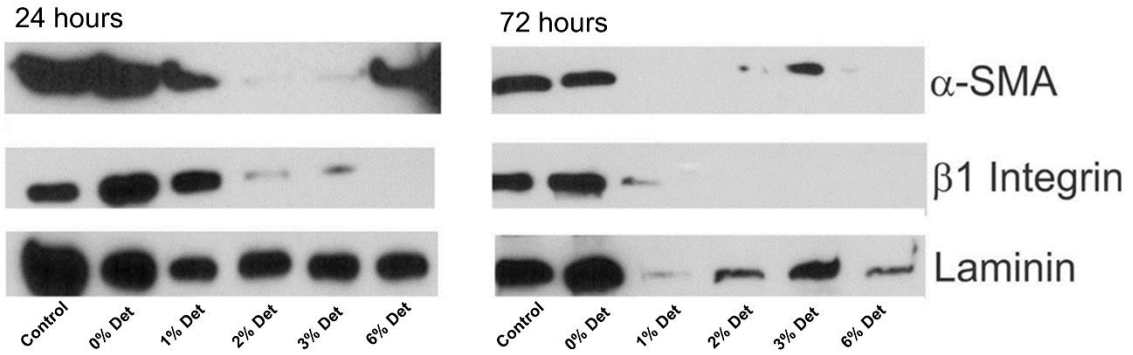

Figure 4.2 - Western blot analysis of representative cytoplasmic (α-smooth muscle actin), cell surface (β1 integrin), and basement membrane (laminin) proteins. Representative images of western blots illustrating the effects of anionic detergent concentration and treatment duration. Lanes 1 – 6 are untreated control, 0% detergent, 1% detergent, 2% detergent, 3% detergent and 6% detergent, respectively.

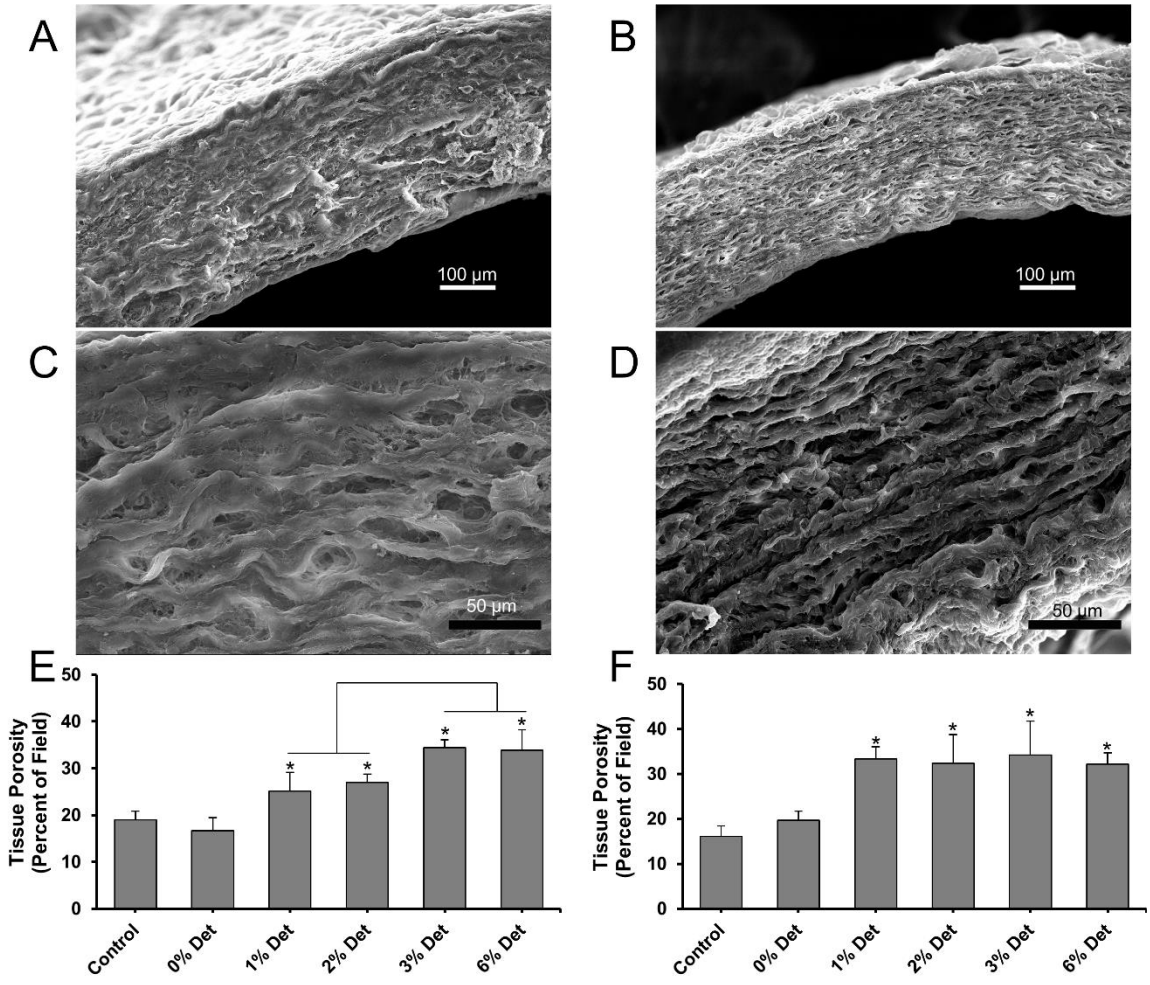

Figure 4.3 - Representative scanning electron microscopic images of the [A, C] 72-hour control sample at low and high power [B, D] 1% detergent for 72 hours at low and high power. Quantification of the total porosity in tissues after [E] 24 hours and [F] 72 hours for all anionic detergents was performed on high-powered images. Statistical significance between detergent concentrations relative to untreated controls was determined by one-way ANOVA and is indicated by (*) at $p<0.05$. Mean ± SD, n=3 for each group.

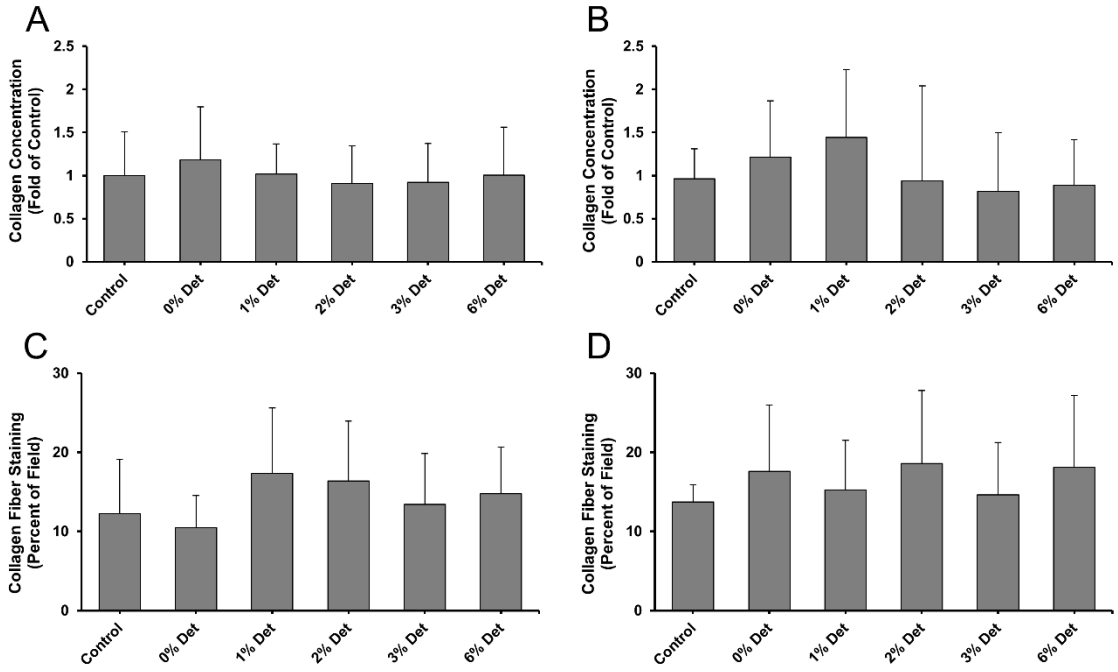

Figure 4.4 - Quantification of hydroxyproline concentrations after [A] 24 hours and [B] 72 hours of anionic detergent treatment. Collagen percent volume quantified by image thresholding of picrosirius red-stained tissue sections after treatment of [C] 24 hours and [D] 72 hours. No statistically significant differences were found following ANOVA analysis. Mean ± SD, n=5 for each group.

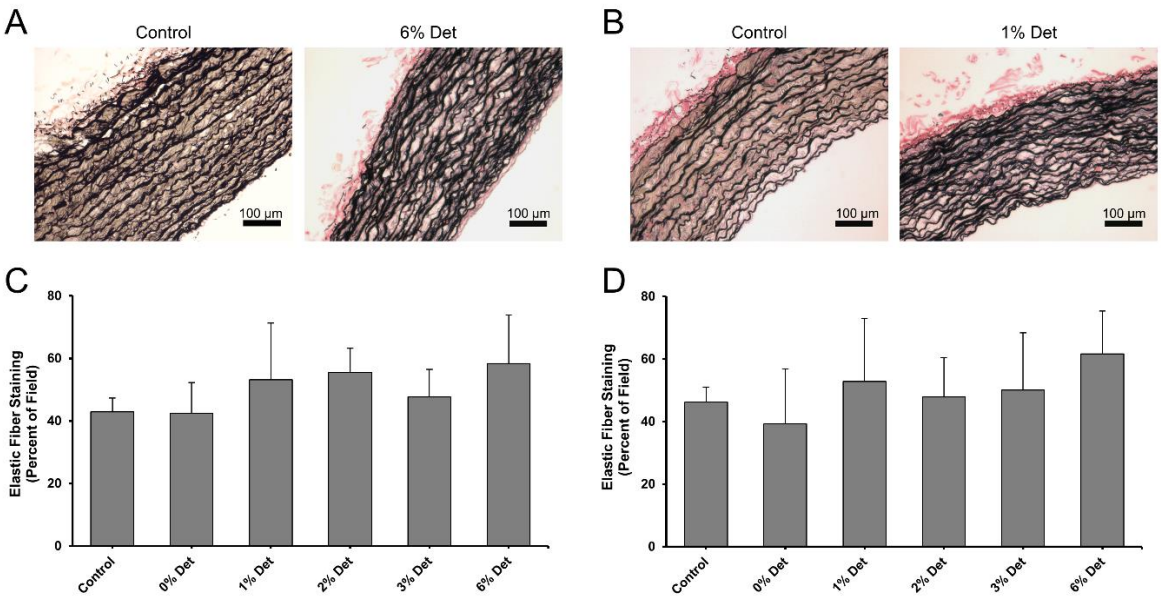

Figure 4.5 - Quantitative analysis of elastic fibers following anionic detergent treatment. Representative microscopic images of control samples, 6% detergent, and 1% detergent for [A] 24 hours and [B] 72 hours, respectively. Elastic fiber area fraction was quantified from Verhoeff-Van Gieson-stained tissue following anionic detergent treatment for [C] 24 hours and [D] 72 hours. No statistically significant differences were found following ANOVA analysis. Mean ± SD, n=5 for each group.

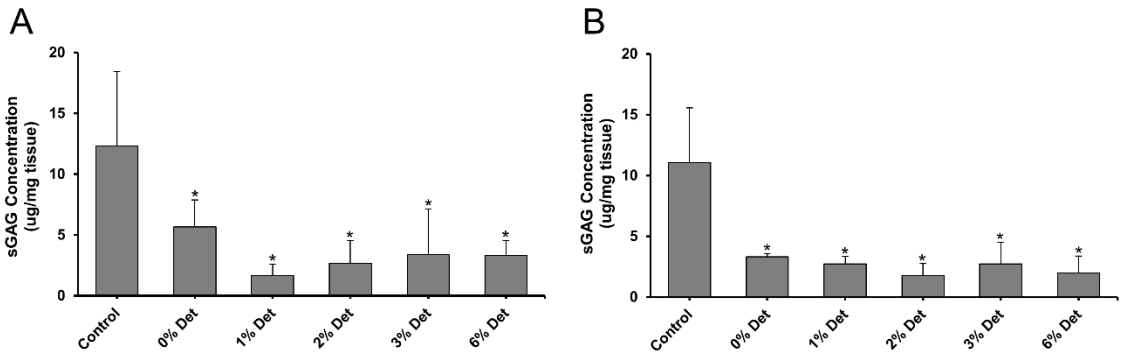

Figure 4.6 - Analysis of dimethylmethylene blue (DMMB) concentrations of all anionic detergent concentrations following [A] 24 and [B] 72 hours of treatment. DMMB concentration was indicative of the glycosaminoglycan concentration present in all tissue samples. Statistical significance between detergent concentrations relative to untreated controls was determined by one-way ANOVA and is indicated by (*) at $p<0.05$. Mean ± SD, n=5 for each group.

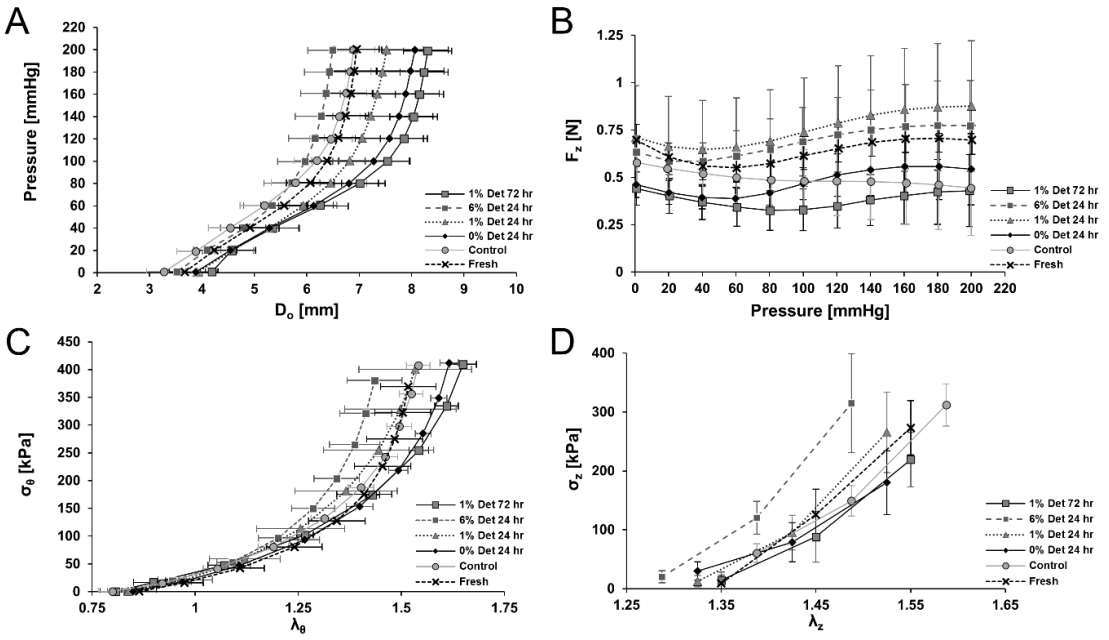

Figure 4.7 - Biaxial mechanical data for all decellularization groups and fresh porcine ITA tissue. [A] Pressure-outer diameter, [B] axial force-pressure, [C] circumferential stress-stretch all plotted at λ_z = 1.45. [D] Axial stress-stretch at 100 mmHg. Mean ± SEM, n=4 for each group.

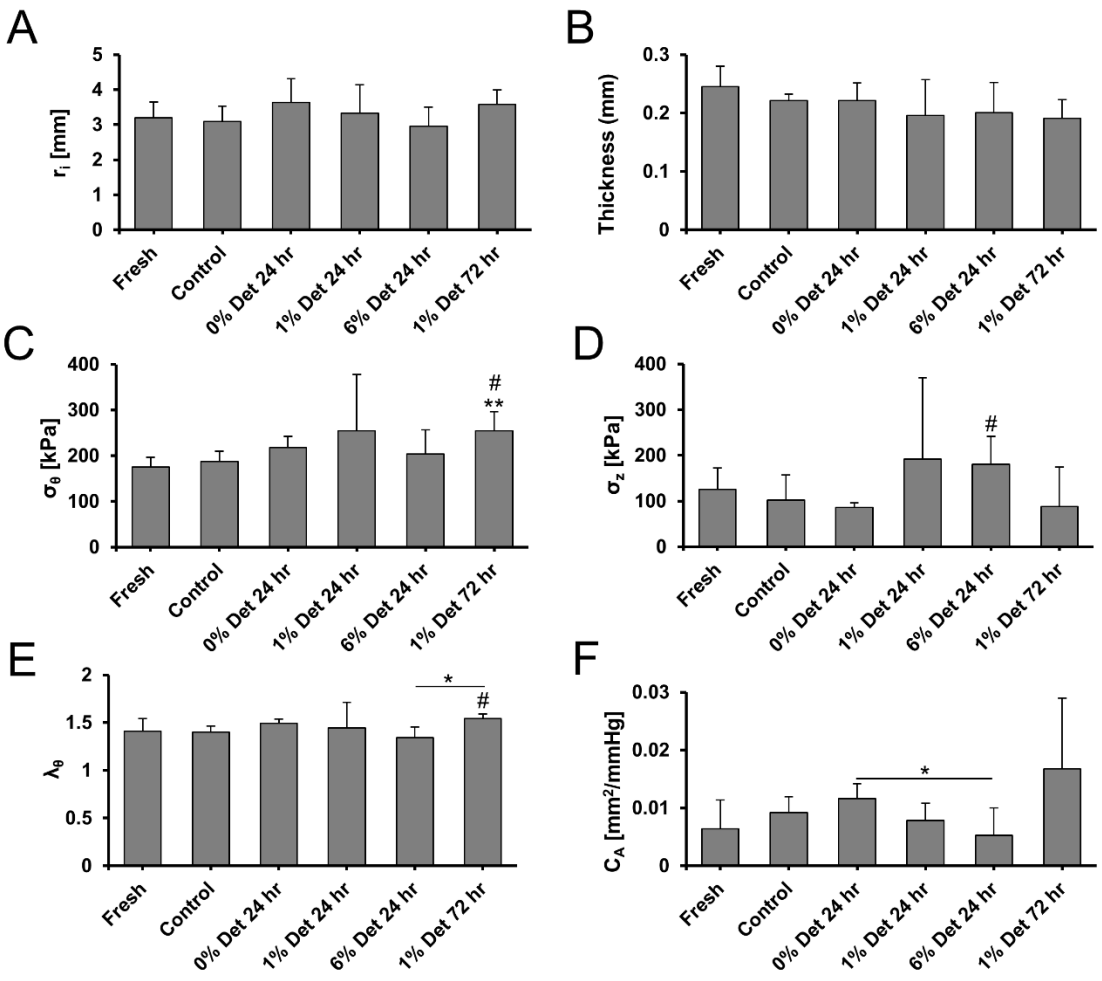

Figure 4.8 - Biaxial mechanical data of decellularized porcine ITAs plotted at common loading conditions of 100 mmHg and λ_z = 1.45. [A] Inner radius, [B] thickness, [C] circumferential stress, [D] axial stress, [E] circumferential stretch, and [F] area compliance. Statistical significance between different decellularized treatments is indicated by (*) at $p<0.05$. Statistical significance between a decellularized ITA group and the control or fresh tissue is indicated by (#) and (**), respectively. Mean ± SD, n=4 for each group.

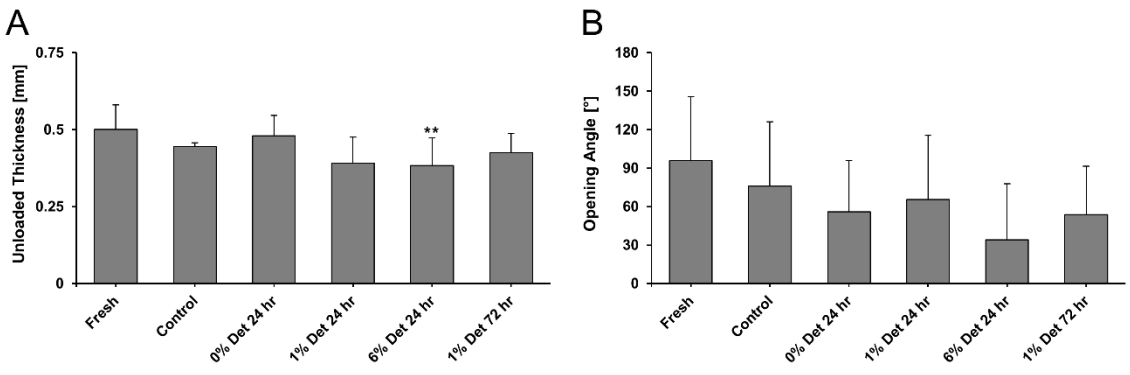

Figure 4.9 - Unloaded conditions of decellularized and fresh porcine ITAs. [A] Average unloaded wall thickness and [B] opening angle. Statistical significance between a decellularized ITA group and the fresh tissue group is indicated by (**) at $p<0.05$. Mean ± SD, n=4 for each group.

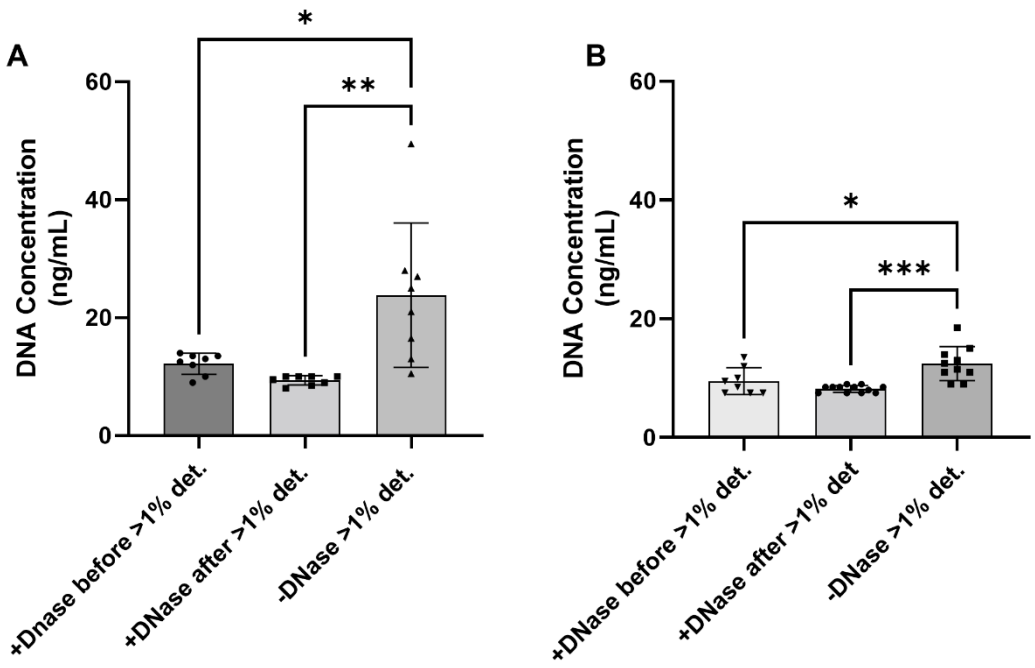

Supplemental Figure 4.10 - Quantified PicoGreen DNA concentrations for [A] 24-hour and (B) 72-hour samples treated with DNAse (+DNase) before or after detergents or when DNase was omitted from the protocol (-DNase). Statistical significance given by (*, **,***) at $p<0.05$, $p<0.01$, and $p<0.001$ respectively. Mean ± STD, n=8-12.

CHAPTER 5

COMPARISON OF ELASTOMUSCULAR ARTERY CRYOPRESERVATION STRATEGIES [4]

[4] Kostelnik, C. J., Crouse, K. J., Goldsmith, J., Eberth J. F.
To be submitted to *Annals of Biomedical Engineering*

5.1 ABSTRACT

The formation of low-temperature ice crystals can severely influence cellular and tissue microarchitecture by damaging cell membranes and extracellular matrix materials alike. Cryopreservation techniques have been developed to circumvent unwanted biological and physical consequences through controlled media exchange and regulated freezing conditions. Penetrating cryoprotecting agents (CPAs) like dimethyl sulfoxide (DMSO) replace intracellular water to minimize ice crystal growth during freezing, whereas nonpenetrating CPAs such as polyvinyl alcohol (PVA) halt ice recrystallization during thawing. Since extracellular matrix proteins and water content contribute substantially to the gross properties of all soft-biological tissues and elastomuscular arteries play a major role in bypass grafting, the consequences of cryopreservation techniques on the mechanical properties and microarchitecture of these arteries warrant further investigation. The middle region of porcine internal thoracic artery (ITA3; n=5/group) were exposed to different freezing rates (slow, controlled, flash) and long-term storage temperatures (-20°C vs -196°C) with or without cryoprotecting agents (5% DMSO + 1mg/mL PVA). Scanning electron microscopy showed that only rapidly frozen samples experienced moderate CPA-independent delamination. Although some viscoelastic changes were observed in post-thawed tests, standard biaxial mechanical data, for the most part, failed to reveal significant differences between groups. Thus, the mechanical properties do not depend on elastomuscular artery cryopreservation technique. Metabolic activity measured using the methyl thiazole-tetrazolium (MTT) assay, on the other hand, was only demonstrated in cryoprotected groups.

5.2 INTRODUCTION

The internal thoracic artery (ITA) is the preferred autologous grafting option but may not be available for patients that require multiple bypasses or a reintervention surgery, so the use of donor or xenogenic tissue sources is required [17]. However, there is minimal consistency regarding the preservation methods of tissue for these circumstances. Since extracellular matrix (ECM) proteins and water content contribute substantially to the gross properties of vascular tissues, there exists a need to investigate possible preservation techniques of elastomuscular arteries [10, 108].

The adverse biological processes that occur during the long-term storage and transportation of diverse tissues can be mitigated by lowering temperatures below 4°C [159, 160]. Unfortunately, the formation of unwanted ice crystals can severely damage cell membranes and ECM structures. Therefore, several damage-limiting cryopreservation techniques have been developed to control media exchange and regulate freezing conditions. The addition of cryoprotecting agents (CPAs) and the application of controlled rate freezing has been successful in the storage of many biological tissues and biomaterials [64, 66]. The different categories of CPAs include penetrating and non-penetrating depending on the agent's innate ability to diffuse through cell membranes [66]. Dimethyl sulfoxide (DMSO) is the most commonly used permeating CPAs because it has shown to effectively decrease the freezing temperature of intracellular water at low concentrations ranging from 5-15% [66]. Sucrose is a common non-penetrating CPA and is effective at protecting against ice nucleation in extracellular spaces [161, 162]. Recent investigations have found that antifreeze proteins (AFPs) exist in nature to protect cellular and extracellular structures during freezing and thawing [163–165]. Other researchers have

explored the use of polymers that act as synthetic antifreeze (glycol)proteins to mitigate ice nucleation during freezing and recrystallization during thawing [166–168]. Polyvinyl alcohol has been identified as a freezing stabilizer that protects membrane structures throughout freezing and thawing. The other technical factor that can influence cell and tissue recovery is the rate at which biological materials are frozen and thawed [169]. A slow freeze can result in tissue dehydration, while a rapid freeze can create intracellular ice crystals [63]. The optimal freezing rate that has shown to achieve the best post-thaw cell and tissue recovery is a controlled freeze at -1°C/min [66, 67, 170]. A combinative method of a controlled freezing rate and use of both penetrating and non-penetrating CPAs can minimize intra- and extracellular ice nucleation [171]. While freeze-thaw physical damage most commonly arises from the freezing process, the thawing rate also warrants concern because of the risk of ice recrystallization. Rapid thawing is achieved by placed the samples in a 37°C bath and has been shown to minimize the incidence of ice recrystallization [170]. Lastly, the elution of CPAs post-thaw warrant methodological consideration because many CPAs are cytotoxic above 4°C [62, 170]. Either a single-step or step-wise elution can be implemented to remove the CPAs. A step-wise elution process has been shown to minimize volume excursions thereby reducing the risk of cellular osmotic shock and subsequent lysis [62, 172].

There is little evidence identifying an optimum cryopreservation technique that minimizes damage to the key load-bearing ECM proteins of elastomuscular arteries commonly used as bypass grafts. The purpose of this study was aimed at the quantification of the mechanical, microstructural, and metabolic consequences to the ITA frozen in the presence and absence of a CPA cocktail at different freezing rates.

5.3 MATERIALS AND METHODS

5.3.1 Tissue Acquisition

The middle region of the left internal thoracic artery (LITA) were harvested fresh from 2-year-old American Yorkshire sows weighing approximately 200 kg originating from a local abattoir. The arteries were dissected under sterile conditions within 1 hour of slaughter and transported in Krebs-Henseleit Buffer (KHB) (118 mM NaCl 118, 11 mM glucose, 25 mM NaHCO3, 4.7 mM KCL, 1.2 mM MgSO4,1.2 mM KH2PO4, 1.2 mM CaCl2) with the anticoagulant heparin sodium (20 U/mL). All samples were cleared of adipose and perivascular tissue and rinsed in three changes of KHB for 10 minutes each on a rotator at 25°C to remove any residual blood.

5.3.2 Freezing and Thawing

Samples immersed in a CPA cocktail (5% DMSO + 1mg/mL PVA) were mixed under mild agitation for 10 minutes before freezing to ensure permeation of DMSO through cell membranes. The arteries were exposed to different freezing rates (slow, controlled, rapid) and storage temperatures (-20°C or -196°C). A slow freeze was achieved by placing samples in a -20°C freezer for a minimum of 24 hours. To achieve a controlled freezing rate of 1°C/min, arteries were frozen in a Mr. Frosty^{TM} apparatus filled with 100% isopropyl alcohol that was placed in a -80°C freezer for a minimum of 4 hours. After that, these samples were stored at -196°C until thawing. Arteries were rapidly frozen by immersion of the cryovials in liquid nitrogen and stored -196°C. All samples held at -196°C were placed in the vapor phase of liquid nitrogen to minimize risk of damaging the cryovials.

A rapid thawing procedure was achieved by placing the frozen samples in a 37°C water bath until no ice remained. The DMSO was eluted out of cryoprotected samples through step-wise rinses in low DMSO concentrations (2%, 1%, 0%) supplemented with the D-mannitol (0.25 M) to minimize osmotic shock [170]. The arteries frozen without CPAs were rinsed with KHB under mild agitation. To investigate the effects of long-term storage, samples from each group were held at the relative storage temperatures for at least 6 months. The same rapid thawing procedure and step-wise rinses was applied to these arteries.

5.3.3 Biaxial Mechanical Testing

All testing was performed on a Bose BioDynamic biaxial mechanical testing device. Fresh and frozen arteries from all freezing conditions and storage durations were cut into 2 cm sections, mounted onto two luer fittings, and fixed in place with 3-0 braided silk sutures. The unloaded length was measured as the distance between sutures and used to calculate experimental axial stretches. The passive mechanical behavior for all fresh and frozen arteries were capture by supplementing KHB with sodium nitroprusside (10-5 M). Samples were inflated to via applied downstream resistance and increasing the volumetric flow rate of a steady flow pump.

To minimize hysteresis and ensure reproducible results, every sample underwent five cycles of axial extension and inflation preconditioning. Inflation-extension biaxial testing was then conducted from 0 to 200 mmHg at the force-invariant axial stretch ratio (i.e., λ_z = 1.45), as well as at ±10% (i.e., λ_z = 1.35 and 1.55). A force-invariant axial stretch is that which yields a constant axial force (<200 mN change) throughout inflation.

The outer diameter, axial force, and luminal pressure were captured in triplicate for each axial stretch at pressure increments of 20 mmHg.

The cross-sectional geometry was measured from a 1 mm thick ring segment cut from an untested region of the vessel. Then the zero-stress state was measured by placing a radial cut and allowing the tissue to equilibrate for in KHB for 30 minutes. A Canon EOS 60d DSLR camera mounted to a dissecting microscope with an adapter lens (Micro Tech Lab) was used to capture images of these geometries, and ImageJ image analysis software (NIH) was used to measure metrics such as cross-sectional area (A), and the inner (L_i) and outer (L_o) arc lengths. The unloaded thickness (H) and opening angle (Φ) were then calculated from

$$H = \frac{2A}{L_i + L_o} \text{ and } \Phi = \pi - \frac{L_o - L_i}{2H} \tag{1-2}$$

Under the assumption of tissue incompressibility, the inner radius (r_i) could be found at any deformed configuration given that

$$r_i = \sqrt{r_o^2 - \frac{A}{\pi \lambda_z}} \tag{3}$$

where is the axial stretch ratio. The mean circumferential and axial stretch ratios can be calculated from

$$\lambda_z = \frac{l}{L} \text{ and } \lambda_\theta = \frac{2\pi\left(r_i + r_o\right)}{L_i + L_o} \tag{4-5}$$

with *l* and *L*, the deformed and undeformed lengths, respectively. Then the mid-wall circumferential stress (σ_θ), mean axial stress (σ_z), and mean area compliance (C_A) are

calculated from The average circumferential σ_θ and axial σ_z stresses were (see also Prim et al. 2018):

$$\sigma_\theta = \frac{Pr_i}{r_o - r_i} \text{ and } \sigma_z = \frac{F}{\pi\left(r_o^2 - r_i^2\right)},\ C_A = \pi\frac{\Delta r_i^2}{\Delta P} \tag{6-8}$$

where F is the axial force and P the transmural pressure. For compliance, Δr_i is the change in inner radius per change in pressure ΔP calculated between 100 ± 20 mmHg. Lastly, to quantify any hysteresis within each fresh and frozen sample, the absolute differences in circumferential and axial stresses between the third and first experimental trial were calculated at the force-invariant stretch ratio and 100 mmHg.

5.3.4 Scanning Electron Microscopy

All fresh and frozen arteries were cut into approximately 3 mm cross-sectional segments and fixed in 2.5% glutaraldehyde for 24 hours. These cross-sections were then rinsed in 1% phosphate buffered saline (PBS) (3 x 15 minutes) under mild agitation. All samples were then immersed in 1% osmium-tetroxide in 1% PBS for 1 hour followed by rinsing in of 1% PBS for (3 x 20 minutes) with mild agitation. The samples were dehydrated via a graded ethanol series (1 x 15 minutes in 50% and 75%, and 2 x 15 min in 95% and 100%) and immersion in fresh hexamethyldisilazane (HMDS) (2 x 15 minutes). HMDS was then decanted, and the samples were left to dry overnight. The dried ring-segments were then mounted to stubs and sputter-coated with 3 layers of gold. All fresh and frozen ring-segments were imaged at 100X magnification on a JEOL JSM-IT100 scanning electron microscope.

5.3.5 Tissue Viability Assay

The metabolic activity after freezing was qualitatively assessed through the colorimetric methyl thiazole-tetrazolium (MTT) assay. Upon thawing, all fresh and frozen arteries were cut into 1 mm cross-sections that were then immersed in sterile Moscona's solution containing MTT (0.5 M) at 37°C for 1 hour. Samples were then rinsed in sterile 1% PBS (3 x 15 minutes) under mild agitation to elute any remaining MTT. Then a Canon EOS 60d DSLR camera mounted to a dissecting microscope was used to capture an image of the whole cross-section for each fresh and frozen artery.

5.3.6 Statistical Analyses

Experimental data from biaxial mechanical testing were compared and analyzed using GraphPad Prism. To compare the biaxial mechanical data A one-way ANOVA with a two-tailed paired t-test of unequal variances was used to determine if any statistical differences existed between frozen groups and between the fresh ITA samples. Statistically significant differences were taken at a confidence level of $p<0.05$ and $p<0.001$.

5.4 RESULTS

5.4.1 Biaxial Mechanical Data

All vessels exhibited increasingly nonlinear pressure-inner radii behavior at physiological and supraphysiological pressures. Figure 5.1 reports the averaged biaxial data at the approximate force-invariant axial stretch ratio for continuous testing. All fresh and frozen ITA groups exhibited a similar profile of the inner radius throughout the entire pressure range (Figure 5.1A). Most of the frozen arteries exhibited a similar axial force-pressure relationship to the fresh control group except for the slow frozen and rapidly frozen non-cryoprotected ITA samples, which showed a larger axial force reading throughout the entire pressure range (Figure 5.1B). Of note, the 24 hours 4°C group

exhibited the smallest axial force reading for all groups. When the continuous circumferential stress-stretch data was plotted (Figures 5.1C), a stiffer behavior was demonstrated in terms of the increase in stress for a given change in stretch ratio. Most notably, the slow frozen non-cryoprotected group showed a stiffer response while the 24 hour 4°C group showed a more compliant response than all of fresh and frozen groups. The axial stress-stretch plots (Figures 5.1D) revealed a close association amongst all fresh and frozen ITA group at the force-invariant (1.45) and low (1.35) axial stretches, but experienced greater dispersion of axial stress values at high (1.55) stretches.

When compared at common loading conditions (i.e., 100 mmHg, 1.45 axial stretch ratio) no significant differences emerged between the fresh 24 hour 4°C, and all frozen groups for all in geometric and mechanical metrics (Figure 5.2). Notably, the loaded thickness values for both the fresh and 24 hour 4°C ITAs were lower, albeit insignificantly, than all frozen ITA groups (Figure 5.2B). This change in tissue thickness could be indicative of an increase in uptake of water upon loading. No differences were observed for the mechanical metrics likely due to the high degree of variance amongst samples. However, the mean circumferential stresses remained relatively constant across all group while the mean axial stresses exhibited more variability. To quantitatively assess the viscous dissipation amongst samples, the absolute difference throughout biaxial testing for both circumferential and axial stresses was plotted (Figure 5.3), the 24-hour 4°C ($p = 0.0459$), slow frozen cryoprotected group ($p = 0.0005$), controlled frozen non-cryoprotected group ($p = 0.0378$), and rapidly frozen cryoprotected group ($p = 0.0164$) exhibited a significantly smaller absolute difference in axial stress than the fresh control ITA.

5.4.2 Microstructural Analysis

Representative scanning electron microscopic images of arterial cross-sections from each fresh and frozen group are shown in Figure 5.4. The fresh, 24 hour 4°C control, slow frozen, and controlled frozen samples exhibited a confluent wall structure with no visible ice-damage. The rapid frozen ITA samples exhibited circumferential intimal-medial tears and/or delamination of the regardless of cryoprotections (Figure 5.4D & 5.4H).

5.4.3 Metabolic Activity Analysis

Representative cross-sectional images of each fresh and frozen group following incubation in MTT are shown in Figure 5.5. Purple pigmentation is indicative of metabolically active tissue, which can be seen in both the fresh and 24 hour 4°C control groups (Figure 5.5A & 5.5E). The 24-hour 4°C sample is comparable to an overnight tissue shipment on ice. The white spots found throughout the cross-sections of these samples (Figure 5.5E) is indicative that the metabolic activity of this tissue diminishes 24 hours after dissection. The only frozen group that retained purple pigmentation upon thawing was the cryoprotected sample frozen at a controlled rate (Figure 5.5C). The intensity of pigmentation is less than that of both control ITA samples which is indicative of a lower metabolic activity. The rapidly frozen cryoprotected sample only produced purple coloring along the lumen (Figure 5.5D). All other frozen groups appeared translucent white and were categorized as metabolically inactive.

5.4.4 Long-term Storage Assessment

Representative images of the microstructure and metabolic activity of long-term stored arteries is shown in Figure 5.6. Both the cryoprotected and non-cryoprotected arteries exhibited an intact vascular wall with no obvious visible damage. However, only

the cryoprotected artery contained purple coloring indicating metabolic activity after 6 months of storage (Figure 5.6D).

Mechanical data at common loading conditions (i.e., 100 mmHg, force-invariant axial stretch) for cryoprotected and non-cryoprotected arteries frozen at a controlled rate and held at -196°C for at least 6 months were plotted and compared to fresh and 24 hours 4°C ITA samples (Figure 5.7). Similarly, there were no significant differences found amongst the geometric and mechanical metrics with mean values remaining constant across groups at $p<0.05$. The lack of significant data could be due to the variance amongst samples within both fresh and frozen groups.

5.5 DISCUSSION

Optimizing a method for the preservation of donor tissues (i.e., allografts or xenografts) could aid in alleviating graft shortages and in the development of a biobank for "off-the-shelf" CABGs. Cryopreservation has been shown to minimize unwanted biological and physical effects associated with the storage and transportation of tissues through controlled media exchange and regulated freezing conditions [62, 159]. It is important to protect tissue from intra- and extracellular ice nucleation throughout the freeze-thaw process because ECM proteins and water have substantial contributions to the gross properties of all biological tissues [66, 173]. Our investigation aimed to quantify the biomechanical consequences of different freezing and transportation strategies for this tissue.

In this study, we characterized the structural, biomechanical, and metabolic effects of freezing the ITA at different rates in the presence and absence of a CPA cocktail containing both penetrating and non-penetrating agents. Our biaxial mechanical analysis

of the middle region of the left ITA following a freeze-thaw procedure surprisingly found minimal differences to mean circumferential and axial stresses regardless of freezing rate or cryoprotection. We believe that the freezing rate and cryoprotection had minimal impact on mechanical metrics because the large number of thermally, chemically, and mechanically stable elastic lamellae found in the middle ITA region maintained tissue integrity throughout the freeze-thaw process [174]. These findings support those found in a study conducted by Amin et al. (2011), who showed that mouse carotid arteries stored at 4°C for up to 28 days did not alter the pressure-diameter or pressure-force relationships [174]. In the present study, the passive mechanical response of the porcine ITA after incubation in transportation storage conditions (24-hours 4°C) was preserved with only minor changes to circumferential stress-stretch response and metabolic activity [174]. However, the revelation that fresh samples experienced larger changes in biaxial viscous stresses than frozen groups may indicate that five-cycles of preconditioning are not sufficient to achieve repeatable stress-strain behavior. Still, there is no widely agreed upon number of preconditioning cycles thus we maintained congruency with prior laboratory investigations. Our observed increase, albeit insignificant, in loaded thickness for all frozen groups within the present study could have developed from extracellular ice nucleation increasing tissue porosity thereby facilitating media flux between pressurizations throughout mechanical testing. Our finding coincide with that conducted by Venkatasubramanian et al. (2006), who showed fresh femoral arteries had more viscous dissipation throughout preconditioning in comparison to frozen arteries [65, 174]. In either case, the viscous nature and exchange of the ground substance within the extra-cellular-matrix as well as the changing protein alignment during loading/unloaded contribute to

cyclic loading changes that differ between our fresh and frozen tissue and are a reminder that at best, soft tissues demonstrate pseudoelastic behavior [24, 175].

On the other hand, intracellular ice nucleation has been indicated as the source of diminished isolated cellular recovery throughout the freeze-thaw process [176]. In the present study, preservation of the tissue's metabolic activity was only observed in the ITAs frozen at a controlled rate with cryoprotection. This closely aligns with what was seen in the literature, where the vasoactivity of the femoral artery was preserved for arteries frozen at 0.7°C/min conditions [67]. Our findings show that a controlled freezing strategy allowed for preservation of the tissue's metabolic activity even at a storage time greater than 6 months.

Although our study used biaxial testing rather than ring sections for the analysis of cryopreserved porcine ITAs, it has several limitations that warrant further consideration. First, our biomechanical analysis only focused on the passive mechanics of these arteries while capturing images from an MTT viability assay for inferences to be made on the SMC recovery and subsequent contribution to gross biaxial mechanical active-passive properties of the ITA post-thaw [87]. Additionally, all arteries were harvested from older sows with unknown nutritional and health status. Abattoir sourced tissue was chosen based on its widespread availability and candidacy as a potential source for xenografts. Despite these limitations, our comprehensive investigation of the consequences to native ITA histomechanics following cryopreservation provides key insights into the importance of CPAs and controlled rate freezing to preserve vascular tissue structure and function and provides the knowledge for further investigations of the *in vivo* performance of cryopreserved porcine ITA xenografts.

5.6 CONCLUSIONS

Our combinative investigation of the microstructural, mechanical, and metabolic characteristics after freeze-thaw processing of elastomuscular porcine ITAs frozen at a controlled rate in a cryomedium supplemented with both penetrating and non-penetrating CPAs yielded the greatest post-thaw tissue viability. Viability was partially preserved even after 6 months of storage at -196°C. Our analysis further revealed some microstructural delamination artifacts in rapidly frozen samples. Although some minor viscous changes were found in frozen samples when compared to fresh tissues, a likely indicator of the continual media flux, the overall mechanical properties were minimally affected by any of our cryopreservation techniques. The analysis of these material and biological characteristics contributes to the development of an optimum freezing strategy for porcine ITAs as potential xenografts to be used to alleviate autograft tissue shortages.

5.7 FUNDING SOURCES

This work was funded by grants from the National Science Foundation (EPSCoR OIA-1655740, CMMI 1760906) and the Koerner Family Foundation Fellowship Doctoral Student Fellowship.

5.8 FIGURE

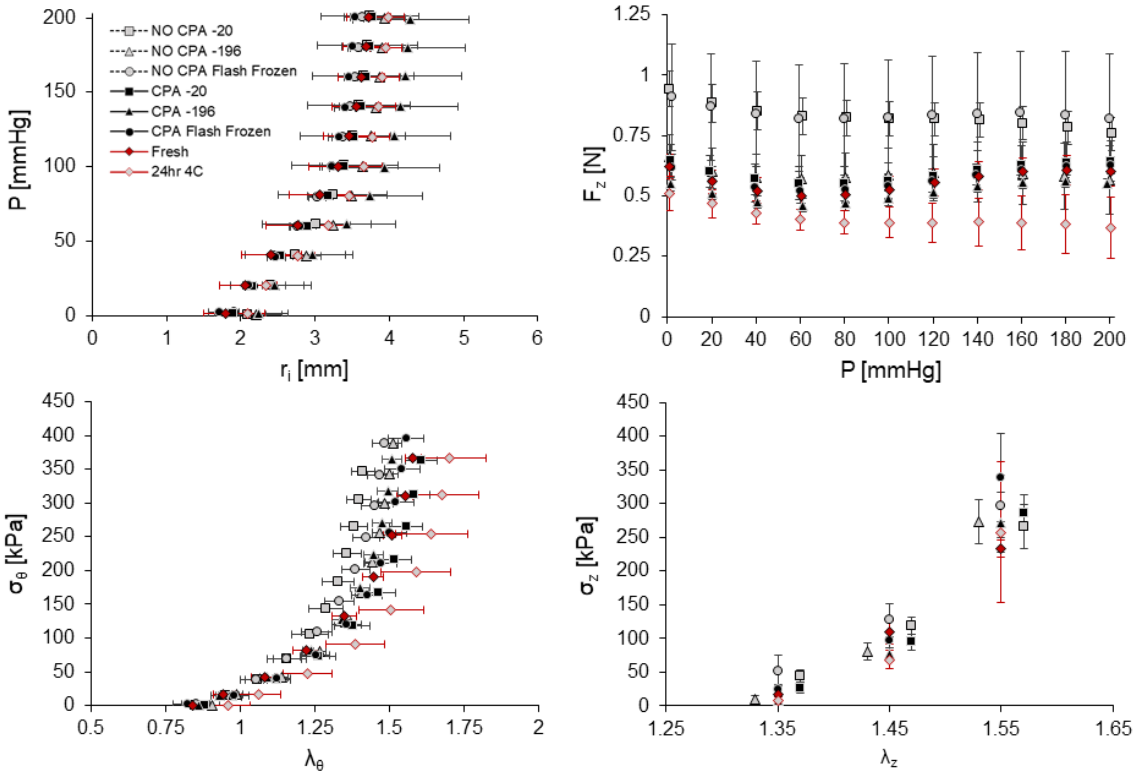

Figure 5.1 - Biaxial mechanical data for all fresh and groups of porcine ITA tissue. [A] Pressure-inner radii, [B] axial force-pressure, [C] circumferential stress-stretch all plotted at the force-invariant axial stretch and 100 mmHg. [D] Axial stress-stretch at 100 mmHg. Mean ± SEM, n=5 for each group.

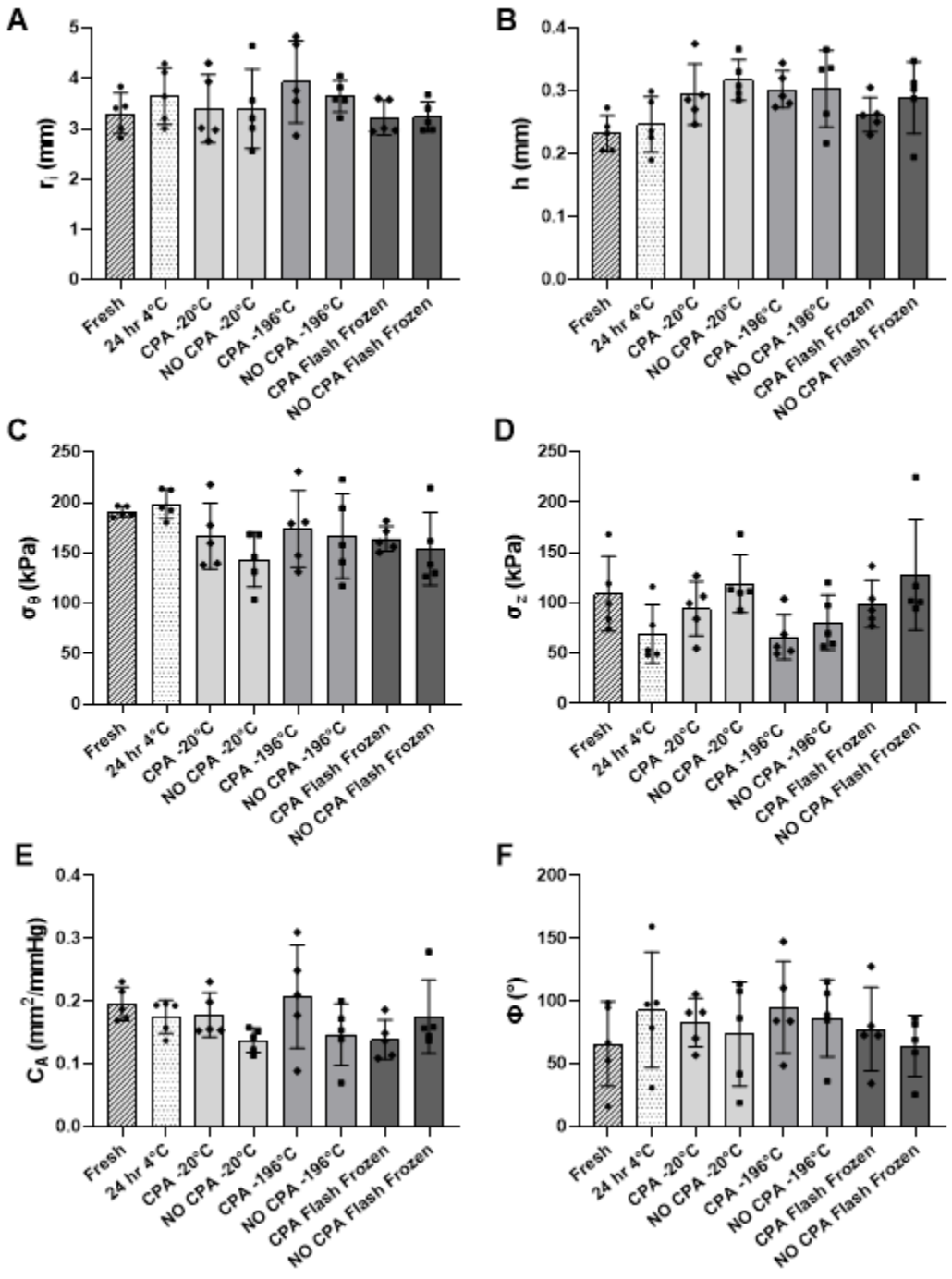

Figure 5.2 - Biaxial mechanical data of porcine ITAs frozen with or without cryoprotection at different freezing rates plotted at common loading conditions of 100 mmHg and the force-invariant axial stretch. [A] Inner radius, [B] loaded thickness, [C] circumferential stress, [D] axial stress, [E] area compliance, and [F] ring sector opening angle. Mean ± SD, n=5 for each group.

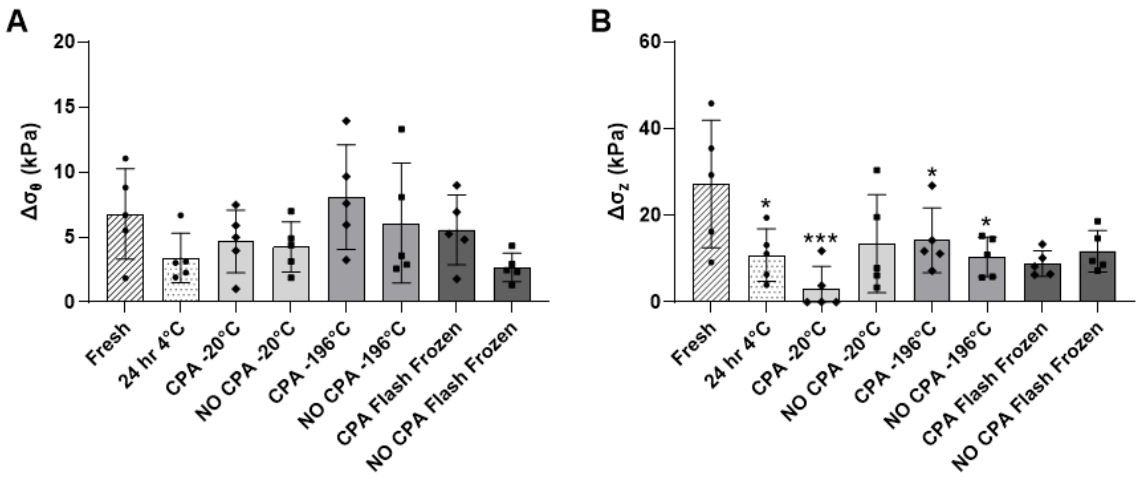

Figure 5.3 – Plots of the difference between the final and initial experimental trials of [A] circumferential and [B] axial stresses between at common loading of 100 mmHg and force-invariant axial stretch for all fresh and frozen groups Statistical significance between a frozen ITA group and the fresh tissue group is indicated by (* and ***) at $p<0.05$ and $p<0.001$, respectively. Mean ± SD, n=5 for each group.

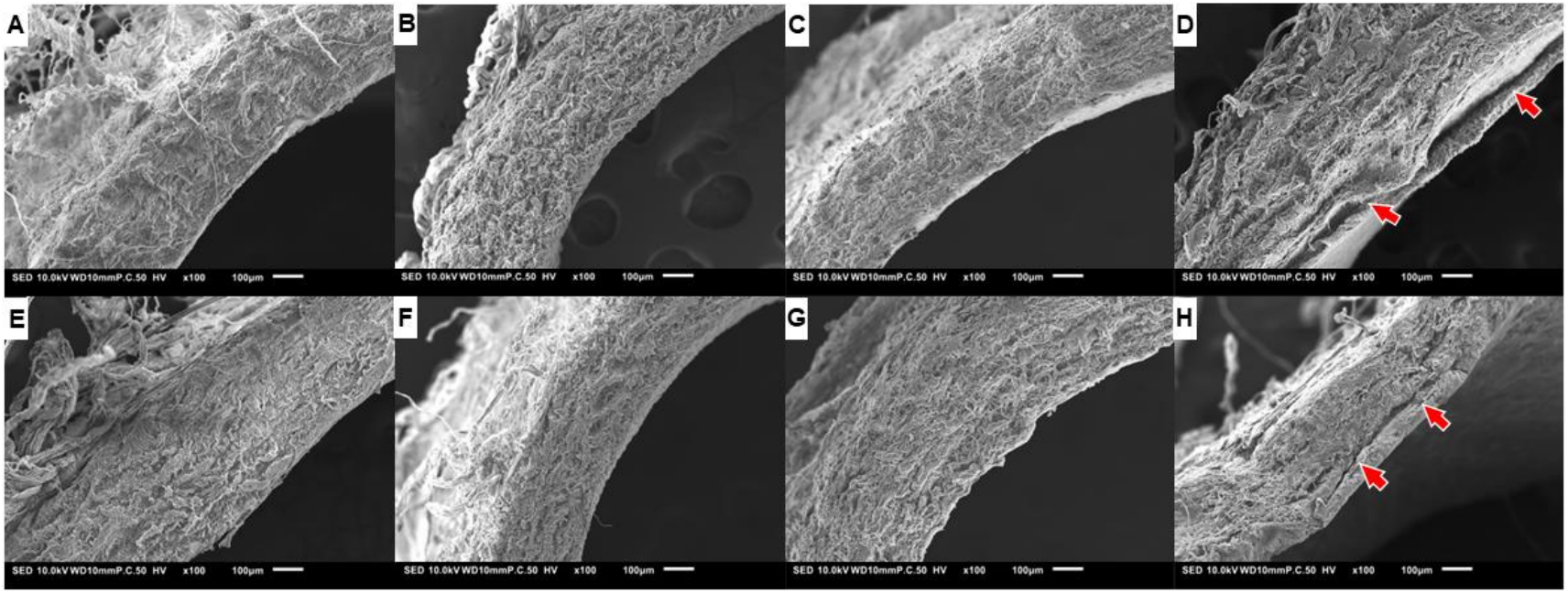

Figure 5.4 - Scanning electron microscopy images of [A] fresh, [E] 24 hours at 4°C control, [B-D] cryoprotected, and [F-H] non-cryoprotected ITA cross-sections. Cross-sectional images grouped by freezing rates illustrate [B] & [F] slow frozen ITAs held at -20°C, [C] & [G] controlled frozen ITAs held at -196°C, and [D] & [H] flash frozen ITAs held at -196°C. Tears within the vascular wall from ice crystal damage are indicated by red arrows.

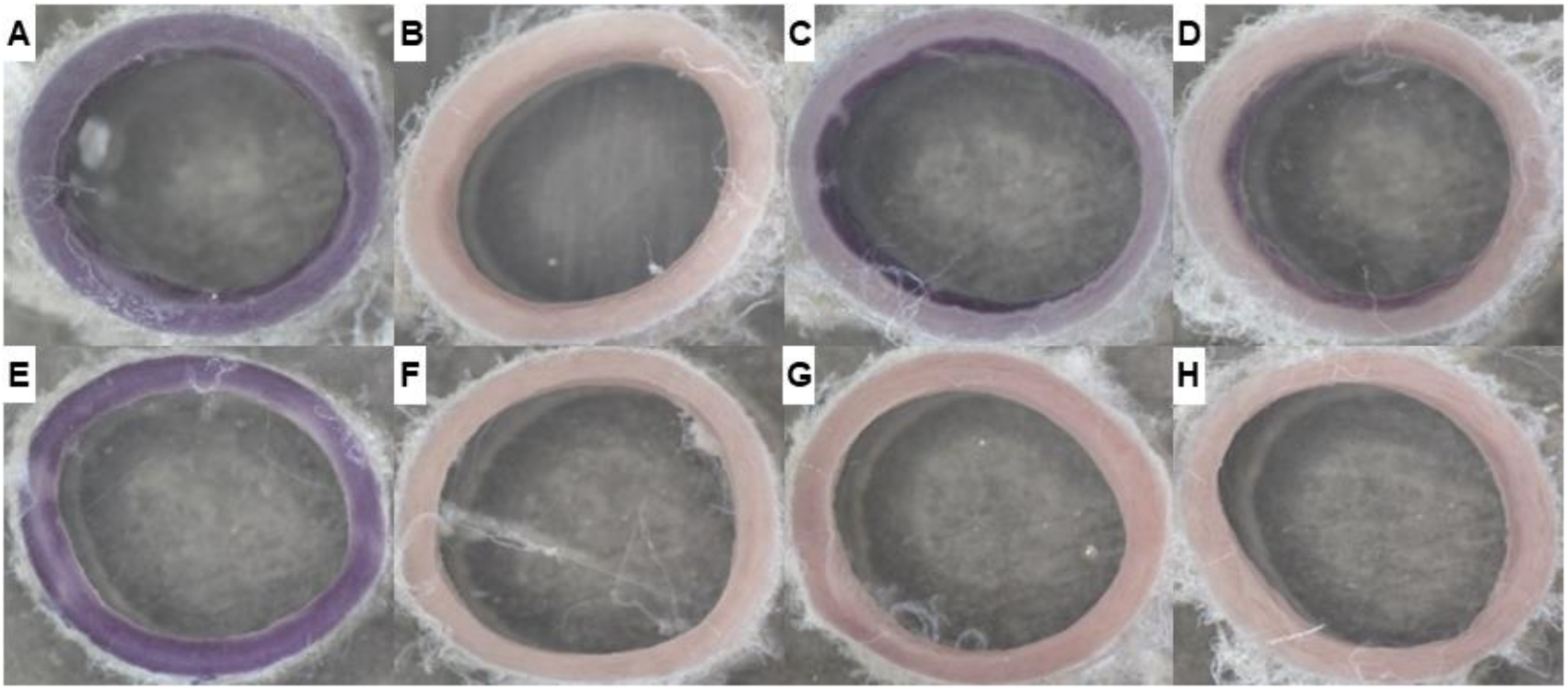

Figure 5.5 - MTT colorimetric metabolic activity representative images of [A] fresh, [E] 24 hours at 4°C control, [B-D] cryoprotected, and [F-H] non-cryoprotected ITA cross-sections. Cross-sectional images grouped by freezing rates illustrate [B] & [F] slow frozen ITAs held at -20°C, [C] & [G] controlled frozen ITAs held at -196°C, and [D] & [H] flash frozen ITAs held at -196°C. Purple hues are indicative of metabolically active tissue.

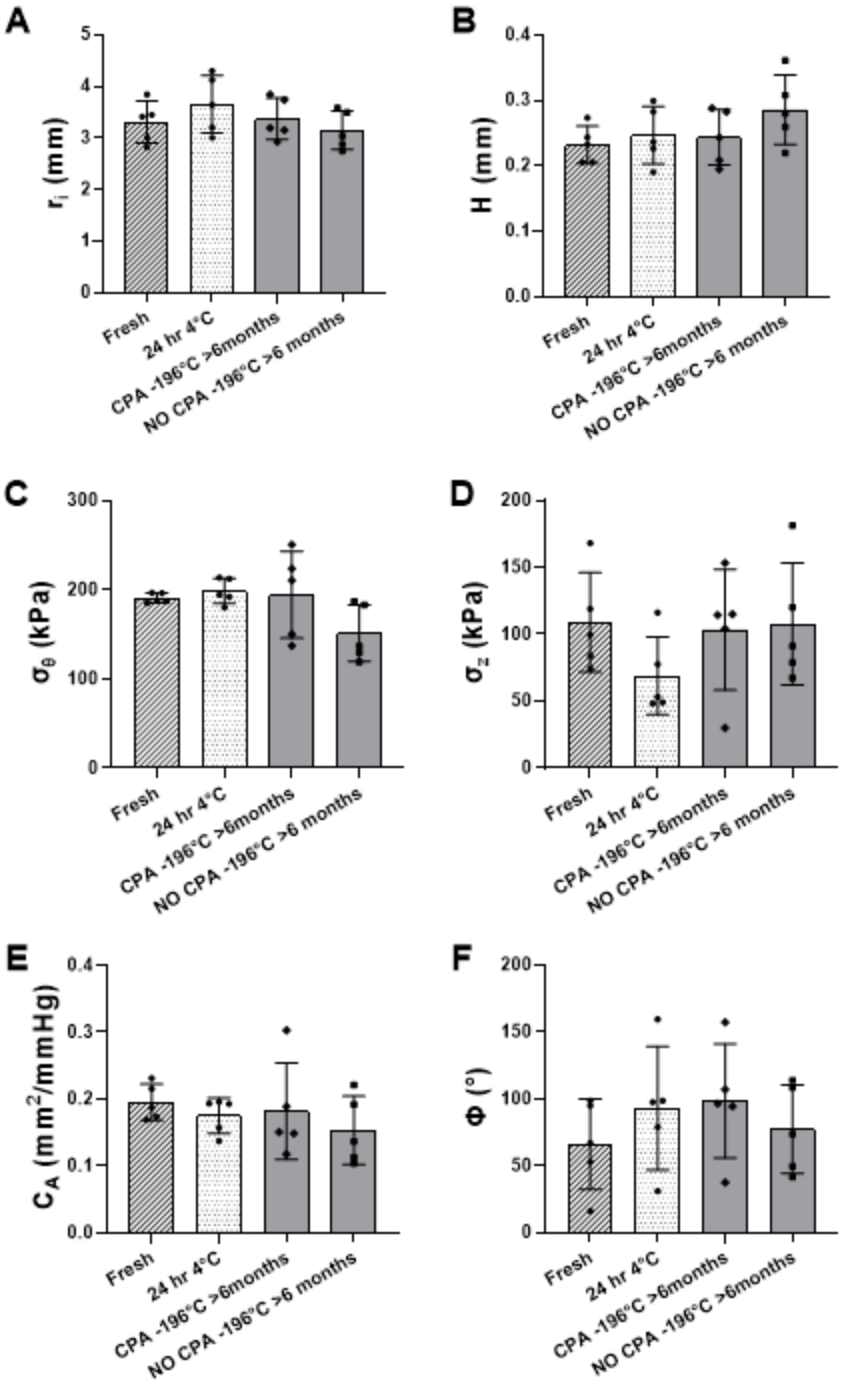

Figure 5.6 - Biaxial mechanical data plotted at common loading conditions of 100 mmHg and the force-invariant axial stretch for fresh control ITAs, 24 hours at 4°C control ITAs, and ITAs frozen with or without cryoprotection at a controlled freezing rate and held for over 6 months. [A] Inner radius, [B] loaded thickness, [C] circumferential stress, [D] axial stress, [E] area compliance, and [F] ring sector opening angle. Mean ± SD, n=5 for each group.

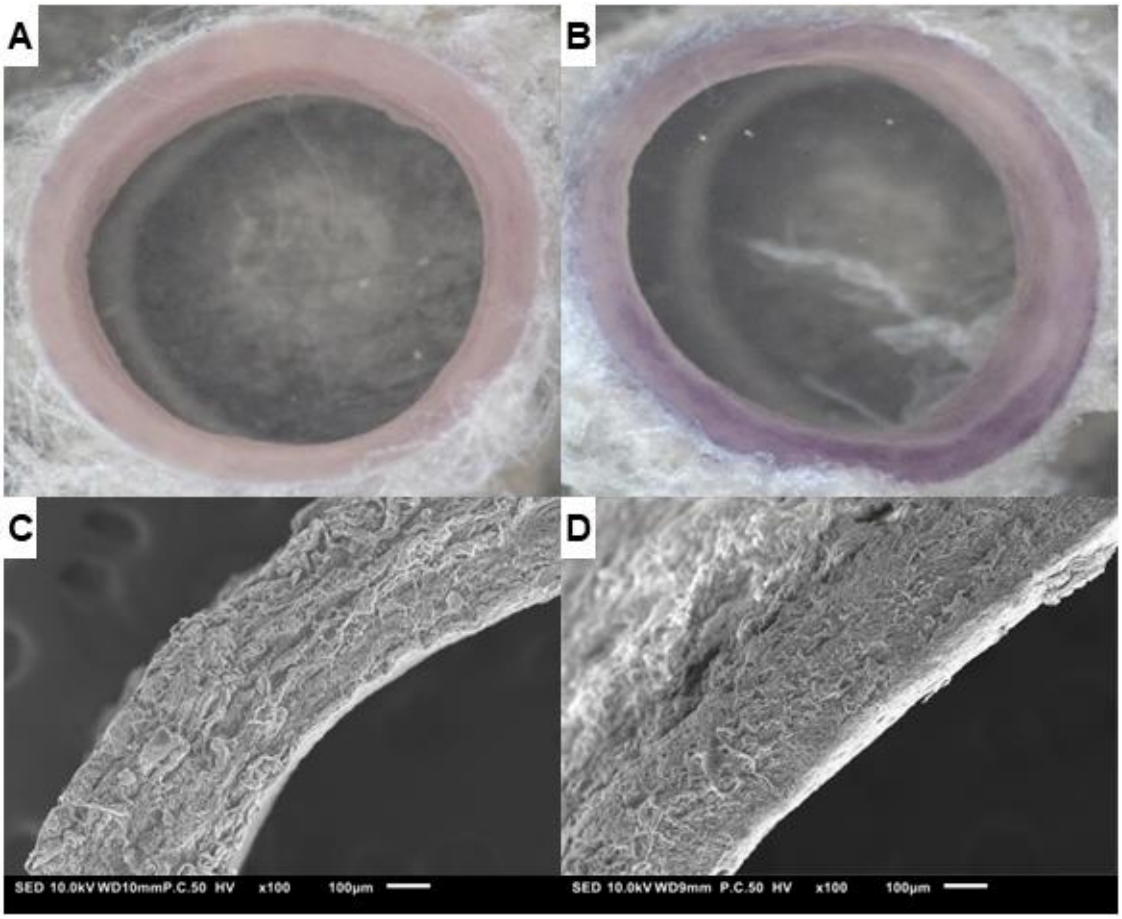

Figure 5.7 – Representative images of the MTT assay and SEM of [A] &[C] non-cryoprotected and [B] &[D] cryoprotected porcine ITAs frozen at -1°C/min and held at -196°C for over 6 months.

CHAPTER 6

CONCLUSIONS

Technological advancements and surgical guidelines have helped lower the total number of hospital discharges for primary CABG procedures, but there exists a need to improve upon the selection of graft candidates for the 6-10% of patients requiring a second surgery in the first post-operative year. Since the surgical procedure was first developed in 1968, empirical evidence has identified superior grafting candidates, anastomosis configurations, and vascular closure systems that reduce the need for reoperation. However, the incidence of CAD and the total number of CABG procedures remains high, and present clinical and economic strains necessitate the further development of surgical standards or a dependable "off-the-shelf" graft.

Clinicians have speculated the implantation of the distal region of the ITA due to the high SMC content presenting increased risk of vasospastic events upon dissection. In Chapter 2 of this dissertation, we quantified the passive biaxial mechanics of the preferred grafting arteries (LITA and RITA) at four distinct locations. We directly compared relevant mechanical metrics such as circumferential stress, axial stress, lumen area compliance, and deformed inner radius for these 8 grafting regions. Through histological image thresholding, we captured a significant shift in the aspect ratio of elastin and collagen, while the SMC and GAG content remained constant. Collectively inputting these findings into the structurally-motivated HGO constitutive model enables cross-disciplinary

implementation of our findings that describe the regionally distinct material properties of these clinically important blood vessels.

Anatomical factors such as the perivascular environment and physiological function play major roles in the development of innate material properties of arteries. Distinct differences in the histological composition and mechanical behavior observed amongst grafting and target arteries has been identified as a component of premature graft failure. The difference in histomechanical properties between the LAD and ITA has been previously studied, but it is unclear whether a particular ITA grafting region presents superior mechanical matching along a surgical interface with the LAD and the other CoAs. Thus, in Chapter 3 we built upon our findings from Chapter 2 and compared the histomechanical properties of the middle LITA segment to that of four common CABG targets arteries (PLAD, DLAD, RCA, and LCX). Here, we used the material parameters of the eight ITA grafting regions to develop 32 *in silico* finite element computational models of an end-to-end anastomosis. Computational models were necessary due to the complex anastomosis geometries not well-suited to *ex vivo* analytical approaches. Regardless, these models were used to create a mechanobiologically-motivated compatibility score to predict mechanically matched graft-target combinations. Our findings depict that the submuscular and middle regions of ITAs produced smaller solid and hemodynamic stress deviations at the anastomotic interface than the proximal or distal regions.

Allogenic and xenogenic tissue sources are used for various surgeries, but their implantation comes with serious drawbacks on the patients' quality of life. The need to remain on immunosuppressive drugs limit their overall use. Investigations of acellular donor tissue scaffolds to serve as grafting conduits show promise, but their immediate

implantation is often limited by restenosis, thrombosis, and inflammation. In Chapter 4, we investigated the biochemical and biomechanical consequences to the porcine ITA following different detergent concentrations and treatment durations for a chemical-enzyme decellularization procedure. From this work, we noticed that complete decellularization was only achieved through 72-hour treatments which only resulted in minor biomechanical changes.

Despite improved patency rates, the annual number of CABG secondary procedures warrant consideration over feasible grafting alternatives. The development of a biobank for donor or excess autologous grafting options could aid in alleviating graft shortages or in the development of a standard CABG candidate. In Chapter 5, we investigated the microstructural, mechanical, and metabolic effects to the ITA following different freezing strategies in the presence and absence of cryoprotection. From this work, we noticed that the mechanical properties of the ITA were preserved regardless of freezing rate or cryomedia. However, metabolic recovery was only observed in cryoprotected arteries frozen at a controlled rate. By understanding the freeze-thaw stresses on the ITA mechanics, microstructure, and metabolic activity, we can identify an appropriate cryopreservation strategy for the storage of CABG candidates or the transportation of samples between research institutions.

Comprehensively, the work reported herein seeks to understand and mitigate CABG failures by improving the selection and processing of potential graft tissues. Although most of the studies illustrated here are classified as biomechanics (how biological bodies respond to forces or displacements), they are all motivated by the field of mechanobiology (how loads contribute to the biological processes). The introduction of

mechanical gradients at the anastomotic interface may accelerate the development of local pathological flow and mechanobiological consequences. Yet, the mechanobiological basis for graft-host diseases and the intrinsic link to atherogenesis is not fully established and is the subject of ongoing and future work in the Eberth lab. That said, preliminary results from our *in vitro* perfusion study (alluded to in Chapter 1), show that anastomosed arteries cultured under pulsatile conditions exhibit intimal thickening after 24 hours. These findings depict that the mechanobiological consequences commonly associated with graft failure can arise even in mechanically-matched tissue combinations. Further investigation of the structural and functional responses to altered compliances within anastomosed arteries would provide evidence of specific atherogenic markers that are sensitive to mechanical mismatch.

In conclusion, the local histomechanical properties for graft and target arteries, as well as compatibility measures, can influence pathological flow conditions and adverse biological reactions within anastomoses that necessitate reoperation. Finite element models of the solid and fluid stress magnitudes at anastomotic interfaces, in conjunction with *in vitro* tissue culture investigations, can eventually be used to explain the mechanobiological contribution to premature graft failure. Advancements in decellularization and cryopreservation techniques can then be used to improve tissue characteristics that drive innovation for the improvement of CABG alternatives and storage approaches

REFERENCES

1. Ralapanawa U, Sivakanesan R. Epidemiology and the magnitude of coronary artery disease and acute coronary syndrome: A narrative review. *J Epidemiol Glob Health*. 2021;11:169–77. doi: 10.2991/JEGH.K.201217.001.

2. Virani SS, Alonso A, Benjamin EJ, Bittencourt MS, Callaway CW, Carson AP, et al. Heart disease and stroke statistics—2020 update a report from the American Heart Association. 2020. doi: 10.1161/CIR.0000000000000757.

3. Lawton JS, Tamis-Holland JE, Bangalore S, Bates ER, Beckie TM, Bischoff JM, et al. 2021 ACC/AHA/SCAI Guideline for Coronary Artery Revascularization: A Report of the American College of Cardiology/American Heart Association Joint Committee on Clinical Practice Guidelines. *J Am Coll Cardiol*. 2022;79:e21–129. doi: 10.1016/j.jacc.2021.09.006.

4. Tiwari A, Cheng KS, Salacinski H, Hamilton G, Seifalian AM. Improving the patency of vascular bypass grafts: The role of suture materials and surgical techniques on reducing anastomotic compliance mismatch. *Eur J Vasc Endovasc Surg*. 2003;25:287–95. doi: 10.1053/ejvs.2002.1810.

5. Head SJ, Milojevic M, Taggart DP, Puskas JD. Current practice of state-of-the-art surgical coronary revascularization. *Circulation*. 2017;136:1331–45. doi: 10.1161/CIRCULATIONAHA.116.022572.

6. Hillis LD, Smith PK, Anderson JL, Bittl JA, Bridges CR, Byrne JG, et al. ACCF / AHA Practice Guideline 2011 ACCF / AHA Guideline for Coronary Artery Bypass Graft

Surgery : Executive Summary A Report of the American College of Cardiology Foundation / American Heart Association Task Force on Practice Guidelines. *Circulation*. 2011;124:2610–42. doi: 10.1161/CIR.0b013e31823b5fee.

7. Rehman I, Kerndt CC, Rehman A. Anatomy, Thorax, Heart Left Anterior Descending (LAD) Artery. StatPearls Publishing [Internet]; Treasure Island (FL); 2021.

8. Chen H, Kassab GS. Microstructure-Based Biomechanics of Coronary Arteries in Health and Disease. *J Biomech*. 2017;49:2548–59. doi: 10.1016/j.jbiomech.2016.03.023.Microstructure-Based.

9. Kassab GS, Rider CA, Tang NJ, Fung Y-C. Morphometry of pig coronary arterial trees. *Am J Physiol Circ Physiol*. 1993;265:H350–65.

10. Prim DA, Zhou B, Hartstone-Rose A, Uline MJ, Shazly T, Eberth JF. A mechanical argument for the differential performance of coronary artery grafts. *J Mech Behav Biomed Mater*. 2016;54:93–105. doi: 10.1016/j.jmbbm.2015.09.017.

11. Chen H, Liu Y, Slipchenko MN, Zhao X, Cheng JX, Kassab GS. The Layered Structure of Coronary Adventitia under Mechanical Load. *Biophys J*. 2011;101:2555–62. doi: 10.1016/j.bpj.2011.10.043.

12. Keyes JT, Lockwood DR, Montilla LG, Witte RS, Vande Geest JP. Comparisons of planar and tubular biaxial tensile testing protocols of the same porcine coronary arteries. *Ann Biomed Eng*. 2013;41:1–23. doi: 10.1007/s10439-012-0679-0.Comparisons.

13. Tinica G, Chistol RO, Enache M, Leon Constantin MM, Ciocoiu M, Furnica C. Long-term graft patency after coronary artery bypass grafting: Effects of morphological and pathophysiological factors. *Anatol J Cardiol*. 2018;20:275–82. doi: 10.14744/AnatolJCardiol.2018.51447.

14. He G-W. Arterial grafts for coronary artery bypass grafting: Biological characteristics, functional classification, and clinical choice. *Ann Thorac Surg*. 1999;67:277–84. doi: 10.1016/s0003-4975(98)01207-7.

15. Gaudino M, Taggart D, Suma H, Puskas JD, Crea F, Massetti M. The Choice of Conduits in Coronary Artery Bypass Surgery. *J Am Coll Cardiol*. 2015;66:1729–37. doi: 10.1016/j.jacc.2015.08.395.

16. Green GE, Stertzer SH, Reppert EH. Coronary Arterial Bypass Grafts. *Ann Thorac Surg*. 1968;5:443–50. doi: 10.1016/S0003-4975(10)66377-1.

17. Melly L, Torregrossa G, Lee T, Jansens J, Puskas JD. Fifty years of coronary artery bypass grafting. *J Thorac Dis*. 2018;10:1960–7. doi: 10.21037/jtd.2018.02.43.

18. Goldman S, Zadina K, Moritz T, Ovitt T, Sethi G, Copeland JG, et al. Long-Term Patency of Saphenous Vein and Left Internal Mammary Artery Grafts After Coronary Artery Bypass Surgery Results From a Department of Veterans Affairs Cooperative Study. *J Am Coll Cardiol*. 2004;44:2149–56. doi: 10.1016/j.jacc.2004.08.064.

19. Gaudino M, Antoniades C, Benedetto U, Deb S, Di Franco A, Di Giammarco G, et al. Mechanisms, Consequences, and Prevention of Coronary Graft Failure. *Circulation*. 2017;136:1749–64.

20. Fitzgibbon GM, Ireland S, Kafka HP, Each AJL, Keon WJ, Hooper D, et al. The fate of coronary artery bypass grafts depends on many factors, including technical faults in harvesting, handling and fashioning the conduits; thrombosis; myointimal hyperplasia; fibrosis; and a rapidly progressing variety of atherosclerosis. *J Am Coll Cardiol*. 1996;28:616–26. doi: 10.1016/0735-1097(96)00206-9.

21. He G. Arterial grafts : clinical classification and pharmacological management. *Ann*

Cardiothorac Surg. 2013;2:507–18. doi: 10.3978/j.issn.2225-319X.2013.07.12.

22. Zhou B, Alshareef M, Prim D, Collins M, Kempner M, Hartstone-rose A, et al. The perivascular environment along the vertebral artery governs segment-specific structural and mechanical properties. *Acta Biomater*. 2016;45:286–95. doi: 10.1016/j.actbio.2016.09.004.

23. Marx R, Clahsen H, Schneider R, Sons H, Klein RM, Gulker H. Histomorphological studies of the distal internal thoracic artery which support its use for coronary artery bypass grafting. *Atherosclerosis*. 2001;159:43–8. doi: 10.1016/s0021-9150(01)00483-x.

24. Eberth JF, Shazly T. Nonlinear Mechanics of Soft Biological Materials. In: Hayenga H, Aranda-Espinoza H, editors. Biomaterial Mechanics. CRC Press; 2017. p. 25–50. doi: 10.1201/9781315152585-3.

25. He G, Yang C, Starr A. Overview of the Nature of Vasoconstriction in Arterial Grafts for Coronary Operations. *Ann Thorac Surg*. 1995;59:676–83.

26. Sahar G, Shavit R, Yosibash Z, Novack L, Matsa M, Medalion B, et al. The physiologic and histologic properties of the distal internal thoracic artery and its subdivisions. *J Thorac Cardiovasc Surg*. 2015;149:1042–50. doi: 10.1016/j.jtcvs.2014.12.028.

27. Mozafari H, Zhou C, Gu L. Mechanical contribution of vascular smooth muscle cells in the tunica media of artery. *Nanotechnol Rev*. 2019;8:50–60.

28. Mattson JM, Turcotte R, Zhang Y. Glycosaminoglycans Contribute to Extracellular Matrix Fiber Recruitment and Arterial Wall Mechanics. *Biomech Model Mechanobiol*. 2017;16:213–25. doi: 10.1007/s10237-016-0811-4.Glycosaminoglycans.

29. Humphrey JD, Eberth JF, Dye WW, Gleason RL. Fundamental role of axial stress in

compensatory adaptations by arteries. *J Biomech*. 2009;42:1–8. doi: 10.1016/j.jbiomech.2008.11.011.

30. Sabik III JF, Lytle BW, Blackstone EH, Houghtaling PL, Cosgrove DM. Comparison of saphenous vein and internal thoracic artery graft patency by coronary system. *Ann Thorac Surg*. 2005;79:544–51. doi: 10.1016/j.athoracsur.2004.07.047.

31. Sabik III JF, Blackstone EH, Gillinov AM, Smedira NG, Lytle BW. Occurrence and Risk Factors for Reintervention After Coronary Artery Bypass Grafting. *Circulation*. 2006;114:454–60. doi: 10.1161/CIRCULATIONAHA.105.001149.

32. Rao VP, Thomas CYJ. A technique for End-to-Side Vascular Anastomosis. *Arch Surg*. 1970;101:91.

33. Rickard RF, Meyer C, Hudson DA. Computational Modeling of Microarterial Anastomoses With Size Discrepancy (Small-to-Large). *J Surg Res*. 2009;153:1–11. doi: 10.1016/j.jss.2008.02.038.

34. Prim DA, Hasanian S. Perfusion Tissue Culture Initiates Differential Remodeling of Internal Thoracic Arteries , Radial Arteries , and Saphenous Veins. *J Vasc Res*. 2018;29208:255–67. doi: 10.1159/000492484.

35. Hahn C, Schwartz MA. Mechanotransduction in vascular physiology and atherogenesis. *Nat Rev Mol Cell Biol*. 2009;10:53–62. doi: 10.1038/nrm2596.

36. Stewart SFC, Lyman DJ. Effects of an Artery / Vascular Graft Compliance Mismatch on Protein Transport : A Numerical Study. *Ann Biomed Eng*. 2004;32:991–1006.

37. Ghista DN, Kabinejadian F. Coronary artery bypass grafting hemodynamics and anastomosis design: A biomedical engineering review. *Biomed Eng Online*. 2013;12:1–28. doi: 10.1186/1475-925X-12-129.

38. Samady H, Eshtehardi P, McDaniel MC, Suo J, Dhawan SS, Maynard C, et al. Coronary artery wall shear stress is associated with progression and transformation of atherosclerotic plaque and arterial remodeling in patients with coronary artery disease. *Circulation*. 2011;124:779–88. doi: 10.1161/CIRCULATIONAHA.111.021824.

39. Cunningham KS, Gotlieb AI. The role of shear stress in the pathogenesis of atherosclerosis. *Lab Investig*. 2005;85:9–23. doi: 10.1038/labinvest.3700215.

40. Gibson CM, Diaz L, Kandarpa K, Sacks FM, Pasternak RC, Sandor T, et al. Relation of vessel wall shear stress to atherosclerosis progression in human coronary arteries. *Arterioscler Thromb*. 1993;13:310–5.

41. Tomaiuolo M, Brass LF, Stalker TJ. Regulation of platelet activation and coagulation and its role in vascular injury and arterial thrombosis. *Interv Cardiol Clin*. 2017;6:1–12.

42. Chistiakov DA, Orekhov AN, Bobryshev Y V. Vascular smooth muscle cell in atherosclerosis. *Acta Physiol*. 2015;214:33–50.

43. Gimbrone MA, Topper JN, Nagel T, Anderson KR, Garcia-CardeÑA G. Endothelial Dysfunction, Hemodynamic Forces, and Atherogenesisa. *Ann N Y Acad Sci*. 2000;902:230–40. doi: 10.1111/j.1749-6632.2000.tb06318.x.

44. Lytle BW, Blackstone EH, Sabik JF, Houghtaling P, Loop FD, Cosgrove DM. The Effect of Bilateral Internal Thoracic Artery Grafting on Survival During 20 Postoperative Years. *Ann Thorac Surg*. 2004;78:2005–14. doi: 10.1016/j.athoracsur.2004.05.070.

45. Stevens LM, Carrier M, Perrault LP, He Y, Cartier R, Bouchard D, et al. Single versus bilateral internal thoracic artery grafts with concomitant saphenous vein grafts for multivessel coronary artery bypass grafting: Effects on mortality and event-free survival. *J Thorac Cardiovasc Surg*. 2004;127:1408–15. doi: 10.1016/j.jtcvs.2003.10.006.

46. Benrashid E, McCoy CC, Youngwirth LM, Kim J, Manson RJ, Otto JC, et al. Tissue engineered vascular grafts: Origins, development, and current strategies for clinical application. *Methods*. 2016;99:13–9. doi: 10.1016/j.ymeth.2015.07.014.

47. Pashneh-Tala S, MacNeil S, Claeyssens F. The tissue-engineered vascular graft - Past, present, and future. *Tissue Eng - Part B Rev*. 2016;22:68–100.

48. Mendibil U, Ruiz-Hernandez R, Retegi-Carrion S, Garcia-Urquia N, Olalde-Graells B, Abarrategi A. Tissue-specific decellularization methods: Rationale and strategies to achieve regenerative compounds. *Int J Mol Sci*. 2020;21:1–29. doi: 10.3390/ijms21155447.

49. Kajbafzadeh A-M, Khorramirouz R, Kameli SM, Hashemi J, Bagheri A. Decellularization of Human Internal Mammary Artery: Biomechanical Properties and Histopathological Evaluation. *Biores Open Access*. 2017. https://doi.org/10.1089/biores.2016.0040. doi: 10.1089/biores.2016.0040.

50. Lin CH, Hsia K, Ma H, Lee H, Lu JH. In vivo performance of decellularized vascular grafts: A review article. International Journal of Molecular Sciences. 2018. doi: 10.3390/ijms19072101.

51. Moroni F, Mirabella T. Decellularized matrices for cardiovascular tissue engineering. *Am J Stem Cells*. 2014;3:1–20.

52. Pellegata AF, Asnaghi MA, Stefani I, Maestroni A, Maestroni S, Dominioni T, et al. Detergent-Enzymatic Decellularization of Swine Blood Vessels: Insight on Mechanical Properties for Vascular Tissue Engineering. *Biomed Res Int*. 2013;2013:918753.

53. Dahl SLMM, Koh J, Prabhakar V, Niklason LE. Decellularized native and engineered arterial scaffolds for transplantation. *Cell Transplant*. 2003;12:659–66.

54. Pu L, Wu J, Pan X, Hou Z, Zhang J, Chen W, et al. Determining the optimal protocol for preparing an acellular scaffold of tissue engineered small-diameter blood vessels. *J Biomed Mater Res - Part B Appl Biomater*. 2018;106:619–31. doi: 10.1002/jbm.b.33827.

55. Partington L, Mordan NJ, Mason C, Knowles JC, Kim HW, Lowdell MW, et al. Biochemical changes caused by decellularization may compromise mechanical integrity of tracheal scaffolds. *Acta Biomater*. 2013;9:5251–61.

56. Neishabouri A, Soltani Khaboushan A, Daghigh F, Kajbafzadeh AM, Majidi Zolbin M. Decellularization in Tissue Engineering and Regenerative Medicine: Evaluation, Modification, and Application Methods. *Front Bioeng Biotechnol*. 2022;10 April:1–21. doi: 10.3389/fbioe.2022.805299.

57. Lopera Higuita M, Griffiths LG. Small Diameter Xenogeneic Extracellular Matrix Scaffolds for Vascular Applications. *Tissue Eng - Part B Rev*. 2020;26:26–45. doi: 10.1089/ten.teb.2019.0229.

58. Casali DM, Handleton RM, Shazly T, Matthews MA. A novel supercritical CO 2 - based decellularization method for maintaining sca ff old hydration and mechanical properties. *J Supercrit Fluids*. 2018;131:72–81. doi: 10.1016/j.supflu.2017.07.021.

59. Kuleshova LL, Gouk SS, Hutmacher DW. Vitrification as a prospect for cryopreservation of tissue-engineered constructs. *Biomaterials*. 2007;28:1585–96. doi: 10.1016/j.biomaterials.2006.11.047.

60. Song YC, Khirabadi BS, Lightfoot F, Brockbank KGM, Taylor MJ. Vitreous cryopreservation maintains the function of vascular grafts. *Nat Biotechnol*. 2000;18:296–9. doi: 10.1038/73737.

61. Cawston TE, Wilson AJ. Understanding the role of tissue degrading enzymes and

their inhibitors in development and disease. *Best Pract Res Clin Rheumatol*. 2006;20:983–1002. doi: 10.1016/j.berh.2006.06.007.

62. Baust JG, Gao D, Baust JM. Cryopreservation: An emerging paradigm change. *Organogenesis*. 2009;5:90–6. doi: 10.4161/org.5.3.10021.

63. Venkatasubramanian RT, Wolkers WF, Shenoi MM, Barocas VH, Lafontaine D, Soule CL, et al. Freeze-thaw induced biomechanical changes in arteries: Role of collagen matrix and smooth muscle cells. *Ann Biomed Eng*. 2010;38:694–706.

64. Bakhach J. The cryopreservation of composite tissues: Principles and recent advancement on cryopreservation of different type of tissues. *Organogenesis*. 2009;5:119–26. doi: 10.4161/org.5.3.9583.

65. Venkatasubramanian RT, Grassl ED, Barocas VH, Lafontaine D, Bischof JC. Effects of freezing and cryopreservation on the mechanical properties of arteries. *Ann Biomed Eng*. 2006;34:823–32. doi: 10.1007/s10439-005-9044-x.

66. Müller-Schweinitzer E. Cryopreservation of vascular tissues. *Organogenesis*. 2009;5:97–104. doi: 10.4161/org.5.3.9495.

67. Rigol M, Heras M, Martínez A, Zurbano MJ, Agustí E, Roig E, et al. Changes in the cooling rate and medium improve the vascular function in cryopreserved porcine femoral arteries. *J Vasc Surg*. 2000;31:1018–25. doi: 10.1067/mva.2000.103793.

68. Müller-Schweinitzer E, Grapow M, Konerding MA, Zerkowski HR. Freezing without surrounding cryomedium preserves the endothelium and its function in human internal mammary arteries. *Cryobiology*. 2005;51:54–65. doi: 10.1016/j.cryobiol.2005.04.005.

69. Chow MJ, Turcotte R, Lin CP, Zhang Y. Arterial extracellular matrix: A mechanobiological study of the contributions and interactions of elastin and collagen.

Biophys J. 2014;106:2684–92. doi: 10.1016/j.bpj.2014.05.014.

70. Benedetto U, Raja SG, Albanese A, Amrani M. Searching for the second best graft for coronary artery bypass surgery : a network meta-analysis of randomized controlled trials †. *Eur J Cardio-Thoracic Surg*. 2015;47:59–65. doi: 10.1093/ejcts/ezu111.

71. Manenti A, Roncati L, Caprili L, Fedeli C. Histological Characterization of the Internal Thoracic Artery as Preferred Conduit for Coronary Bypass. *J Mol Histol Medicial Physiol*. 2016;1:1000103.

72. Henriquez-Pino JA, Gomes WJ, Prates JC, Buffolo E. Surgical anatomy of the internal thoracic artery. *Ann Thorac Surg*. 1997;64:1041–5. doi: 10.1016/s0003-4975(97)00720-0.

73. van Son JAM, Smedts F, de Wilde PCM, Pijls NHJ, Wong-Alcala L, Kubat K, et al. Histological study of the internal mammary artery with emphasis on its suitability as a coronary artery bypass graft. *Ann Thorac Surg*. 1993;55:106–13. doi: 10.1016/0003-4975(93)90483-X.

74. Bedi HS, Sharma VK, Kler TS, Trehan N. Coronary-to-Coronary Bypass Using a Free Internal Mammary Artery: An Alternative. *Ann Thorac Surg*. 1995;59:757–9.

75. Barboso G, Rusticali F. Proximal Internal Mammary In Situ Graft and Distal Coronary-Coronary Graft. *Texas Hear Inst J*. 2000;27:70–1.

76. He G-W. Cautions on the use of distal internal thoracic artery and its bifurcations. *J Thorac Cardiovasc surgery2*. 2015;149:1050–1. doi: 10.1016/j.jtcvs.2014.12.046.

77. Baek S, Gleason RL, Rajagopal KR, Humphrey JD. Theory of small on large: potential utility in computations of fluid–solid interactions in arteries. *Comput Methods Appl Mech Eng*. 2007;196:3070–8. doi: 10.1016/j.cma.2006.06.018.

78. Holzapfel GA, Gasser TC, Ogden RW. A New Constitutive Framework for Arterial Wall Mechanics and a Comparative Study of Material Models. *J Elast*. 2001;61:1–48.

79. Ferruzzi J, Vorp D a, Humphrey JD. On constitutive descriptors of the biaxial mechanical behaviour of human abdominal aorta and aneurysms. *J R Soc Interface*. 2011;8:435–50. doi: 10.1098/rsif.2010.0299.

80. Prim DA, Lane BA, Ferruzzi J, Shazly T, Eberth JF. Evaluation of the Stress-Growth Hypothesis in Saphenous Vein Perfusion Culture. *Ann Biomed Eng*. 2021;49:487–501. doi: 10.1007/s10439-020-02582-1.

81. Fitzpatrick JC, Clark PM, Capaldi FM. Effect of Decellularization Protocol on the Mechanical Behavior of Porcine Descending Aorta. *Int J Biomater*. 2010;:1–11.

82. Roy S, Silacci P, Stergiopulos N. Biomechanical proprieties of decellularized porcine common carotid arteries. *Am J Physiol - Hear Circ Physiol*. 2005;289 4 58-4:1567–76. doi: 10.1152/ajpheart.00564.2004.

83. Hoseinikhah H, Manafi B, Zarifian A, Sobhan M, Andalibi S, Moeinipour Y, et al. Bentall Procedure with Concomitant Coronary-Coronary Bypass for Right Coronary Artery Stenosis : A Case Report. *Razavi Int J Med*. 2016;4:e37803. doi: 10.17795/rijm37803.Case.

84. Gomes WJ. The left and right internal thoracic arteries may not have equivalent histological structures. *Eur J Cardiothorac Surg*. 2014;47:941.

85. Humphrey JD. Cardiovascular Solid Mechanics: Cells, Tissues, and Organs. Springer, New York, USA; 2002. doi: 10.1007/978-0-387-21576-1.

86. He G, Ryan WH, Acuff TE, Yang C, Mack MJ. Greater Contractility of Internal Mammary Artery Bifurcation : Possible Cause of Low Patency Rates. *Ann Thorac Surg*.

1994;58:529–32. doi: 10.1016/0003-4975(94)92246-2.

87. Zhou B, Prim DA, Romito EJ, McNamara LP, Spinale FG, Shazly T, et al. Contractile Smooth Muscle and Active Stress Generation in Porcine Common Carotids. *J Biomech Eng*. 2018;140:1–6.

88. Milnor WR, Baltimore W. Hemodynamics. 1989.

89. Cheng JK, Wagenseil JE. Extracellular matrix and the mechanics of large artery development. *Biomech Model Mechanobiol*. 2012;11:1169–86. doi: 10.1007/s10237-012-0405-8.

90. Dobrin PB. The basic science of vascular disease. Futura; 1997.

91. Badylak SF. Decellularized allogeneic and xenogeneic tissue as a bioscaffold for regenerative medicine: Factors that influence the host response. *Ann Biomed Eng*. 2014. https://doi.org/10.1007/s10439-013-0963-7. doi: 10.1007/s10439-013-0963-7.

92. Prim DA, Mohamed MA, Lane BA, Poblete K, Wierzbicki MA, Lessner SM, et al. Comparative mechanics of diverse mammalian carotid arteries. *PLoS One*. 2018;13:1–18.

93. Furdella KJ, Higuchi S, Behrangzade A, Kim K, Wagner WR, Vande Geest JP. In-vivo assessment of a tissue engineered vascular graft computationally optimized for target vessel compliance. *Acta Biomater*. 2021;123:298–311. doi: 10.1016/j.actbio.2020.12.058.

94. McKavanagh P, Yanagawa B, Zawadowski G, Cheema A. Management and prevention of saphenous vein graft failure: a review. *Cardiol Ther*. 2017;6:203–23. doi: 10.1007/s40119-017-0094-6.

95. Davies MG, Hagen P-O. Pathophysiology of vein graft failure: a review. *Repr Eur J Vasc Endovasc Surg*. 2011;42 Suppl 1:S19-29. doi: 10.1016/j.ejvs.2011.06.013.

96. Dobrin PB, Littooy FN, Endean ED. Mechanical factors predisposing to intimal hyperplasia and medial thickening in autogenous vein grafts. *Surgery*. 1989;105:393–400.

97. Baguneid MS, Goldner S, Fulford PE, Hamilton G, Walker MG, Seifalian AM. A comparison of para-anastomotic compliance profiles after vascular anastomosis: nonpenetrating clips versus standard sutures. *J Vasc Surg*. 2001;33:812–20. doi: 10.1067/mva.2001.1112806.

98. Weston MW, Rhee K, Tarbell JM. Compliance and diameter mismatch affect the wall shear rate distribution near an end-to-end anastomosis. *J Biomech*. 1996;29:187–98. doi: 10.1016/0021-9290(95)00028-3.

99. Ballyk PD, Walsh C, Butany J, Ojha M. Compliance mismatch may promote graft–artery intimal hyperplasia by altering suture-line stresses. *J Biomech*. 1998;31:229–37. doi: 10.1016/s0197-3975(97)00111-5.

100. He F, Hua L, Gao LJ. A computational model for biomechanical effects of arterial compliance mismatch. *Appl Bionics Biomech*. 2015;2015. doi: 10.1155/2015/213236.

101. Eberth JF, Gresham VC, Reddy AK, Popovic N, Wilson E, Humphrey JD. Importance of pulsatility in hypertensive carotid artery growth and remodeling. *J Hypertens*. 2009;27:2010–21. doi: 10.1097/HJH.0b013e32832e8dc8.

102. Andersson M, Karlsson L, Svensson PA, Ulfhammer E, Ekman M, Jernås M, et al. Differential global gene expression response patterns of human endothelium exposed to shear stress and intraluminal pressure. *J Vasc Res*. 2005;42:441–52. doi: 10.1159/000087983.

103. Chatzizisis YS, Coskun AU, Jonas M, Edelman ER, Feldman CL, Stone PH. Role of

Endothelial Shear Stress in the Natural History of Coronary Atherosclerosis and Vascular Remodeling. Molecular, Cellular, and Vascular Behavior. *J Am Coll Cardiol*. 2007;49:2379–93. doi: 10.1016/j.jacc.2007.02.059.

104. Gomez D, Owens GK. Smooth muscle cell phenotypic switching in atherosclerosis. *Cardiovasc Res*. 2012;95:156–64. doi: 10.1093/cvr/cvs115.

105. Humphrey JD. Vascular adaptation and mechanical homeostasis at tissue, cellular, and sub-cellular levels. *Cell Biochem Biophys*. 2008;50:53–78. doi: 10.1007/s12013-007-9002-3.

106. Cavalcanti S, Tura A. Hemodynamic and mechanical performance of arterial grafts assessed by numerical simulation: A design oriented study. *Artif Organs*. 1999;23:175–85. doi: 10.1046/j.1525-1594.1999.06217.x.

107. Fonseca DA, Antunes PE, Antunes MJ, Cotrim MD. Histomorphometric analysis of the human internal thoracic artery and relationship with cardiovascular risk factors. *PLoS One*. 2019;14:1–11. doi: 10.1371/journal.pone.0211421.

108. Kostelnik CJ, Crouse KJ, Carver W, Eberth JF. Longitudinal histomechanical heterogeneity of the internal thoracic artery. *J Mech Behav Biomed Mater*. 2021;116 December 2020:104314. doi: 10.1016/j.jmbbm.2021.104314.

109. Kassab GS, Navia JA. Biomechanical considerations in the design of graft: The homeostasis hypothesis. *Annu Rev Biomed Eng*. 2006;8:499–535. doi: 10.1146/annurev.bioeng.8.010506.105023.

110. Taqueti V. Sex Differences in the Coronary System. *Adv Exp Med Biol*. 2018;1065:257–78. doi: 10.1007/978-3-319-77932-4.

111. Maas SA, Ellis BJ, Ateshian GA, Weiss JA. FEBio: Finite Elements for

Biomechanics. *J Biomech Eng*. 2012;134. doi: 10.1115/1.4005694.

112. Holzapfel GA, Gasser TC, Ogden RW. A New Constitutive Framework for Arterial Wall Mechanics and a Comparative Study of Material Models. *J Elast Phys Sci solids*. 2000;61:1–48. doi: 10.1023/A:1010835316564.

113. Azar D, Ohadi D, Rachev A, Eberth JF, Uline MJ, Shazly T. Mechanical and geometrical determinants of wall stress in abdominal aortic aneurysms: A computational study. *PLoS One*. 2018;13:1–15. doi: 10.1371/journal.pone.0192032.

114. Azar D, Torres WM, Davis LA, Shaw T, Eberth JF, Kolachalama VB, et al. Geometric determinants of local hemodynamics in severe carotid artery stenosis. *Comput Biol Med*. 2019;114:103436. doi: https://doi.org/10.1016/j.compbiomed.2019.103436.

115. Malota Z, Glowacki J, Sadowski W, Kostur M. Numerical analysis of the impact of flow rate, heart rate, vessel geometry, and degree of stenosis on coronary hemodynamic indices. *BMC Cardiovasc Disord*. 2018;18:1–16. doi: 10.1186/s12872-018-0865-6.

116. Ootaki Y, Ootaki C, Kamohara K, Akiyama M, Zahr F, Kopcak Jr MW, et al. Phasic coronary blood flow patterns in dogs vs. pigs: An acute ischemic heart study. *Med Sci Monit*. 2008;14:BR193-197.

117. Ojha M. Wall Shear Stress Temporal Gradient and Anastomotic Intimal Hyperplasia. *Circ Res*. 1994;74:1227–31. doi: 10.1161/01.res.74.6.1227.

118. Davies MG, Hagen P-O. Pathophysiology of vein graft failure: a review. *Eur J Vasc Endovasc Surg*. 1995;9:7–18. doi: 10.1016/S1078-5884(05)80218-7.

119. Yazdani SK, Farb A, Nakano M, Vorpahl M, Ladich E, Finn A V, et al. Pathology of drug-eluting versus bare-metal stents in saphenous vein bypass graft lesions. *JACC Cardiovasc Interv*. 2012;5:666–74. doi: 10.1016/j.jcin.2011.12.017.

120. Wadey K, Lopes J, Bendeck M, George S. Role of smooth muscle cells in coronary artery bypass grafting failure. *Cardiovasc Res*. 2018;114:601–10. doi: 10.1093/cvr/cvy021.

121. Row S, Peng H, Schlaich EMM, Koenigsknecht C, Andreadis STT, Swartz DDD. Arterial grafts exhibiting unprecedented cellular infiltration and remodeling in vivo: the role of cells in the vascular wall. *Biomaterials*. 2015;50:115–26. doi: 10.1016/j.biomaterials.2015.01.045.

122. Eshtehardi P, Teng Z. Protective or destructive: High wall shear stress and atherosclerosis. *Atherosclerosis*. 2016;251:501–3. doi: 10.1016/j.atherosclerosis.2016.05.018.

123. Sarkar S, Salacinski HJ, Hamilton G, Seifalian AM. The Mechanical Properties of Infrainguinal Vascular Bypass Grafts: Their Role in Influencing Patency. *Eur J Vasc Endovasc Surg*. 2006;31:627–36. doi: 10.1016/j.ejvs.2006.01.006.

124. Chapekar MS. Tissue Engineering: Challenges and Opportunities. *J Biomed Mater Res - Part B Appl Biomater*. 2000;53:617–20.

125. Ikada Y. Challenges in tissue engineering. *J R Soc Interface*. 2006;3:589–601.

126. Celikkin N, Rinoldi C, Costantini M, Trombetta M, Rainer A, Święszkowski W. Naturally derived proteins and glycosaminoglycan scaffolds for tissue engineering applications. *Mater Sci Eng C*. 2017;78:1277–99.

127. Cross LM, Thakur A, Jalili NA, Detamore M, Gaharwar AK. Nanoengineered biomaterials for repair and regeneration of orthopedic tissue interfaces. *Acta Biomater*. 2016;42:2–17.

128. Mehrali M, Thakur A, Pennisi CP, Talebian S, Arpanaei A, Nikkhah M, et al.

Nanoreinforced Hydrogels for Tissue Engineering: Biomaterials that are Compatible with Load-Bearing and Electroactive Tissues. *Adv Mater*. 2017;29:1603612.

129. Vedadghavami A, Minooei F, Mohammadi MH, Khetani S, Rezaei Kolahchi A, Mashayekhan S, et al. Manufacturing of hydrogel biomaterials with controlled mechanical properties for tissue engineering applications. *Acta Biomater*. 2017;62 July:42–63.

130. Go A, Mozaffarian D, Roger V. Executive Summary: Heart Disease and Stroke Statistics—2014 Update: A Report of the American Heart Association. *Circulation*. 2014;129:399–410.

131. Li S, Sengupta D, Chien S. Vascular tissue engineering: From in vitro to in situ. Wiley Interdisciplinary Reviews: Systems Biology and Medicine. 2014;6:61–76.

132. He GW. Arterial grafts for coronary artery bypass grafting: Biological characteristics, functional classification, and clinical choice. *Ann Thorac Surg*. 1999;67:277–84.

133. Krishnan S, Clowes AW. Dacron patch infection after carotid endarterectomy: Case report and review of the literature. *Ann Vasc Surg*. 2006;20:672–7.

134. Bachleda P, Kalinova L, Utikal P, Kolar M, Hricova K, Stosova T. Infected prosthetic dialysis arteriovenous grafts: A single dialysis center study. *Surg Infect (Larchmt)*. 2012;13:366–70.

135. Gilbert TW, Sellaro TL, Badylak SF. Decellularization of tissues and organs. *Biomaterials*. 2006;27:3675–83.

136. Gilpin A, Yang Y. Decellularization Strategies for Regenerative Medicine: From Processing Techniques to Applications. *Biomed Res Int*. 2017;2017.

137. Tapias LF, Ott HC. Decellularized scaffolds as a platform for bioengineered organs. *Curr Opin Organ Transplant*. 2014;19:145–52.

138. Cheng CW, Solorio LD, Alsberg E. Decellularized tissue and cell-derived extracellular matrices as scaffolds for orthopaedic tissue engineering. *Biotechnol Adv*. 2014;32:462–84.

139. Jones RS, Chang PH, Perahia T, Harmon KA, Junor L, Yost MJ, et al. Design and Fabrication of a Three-Dimensional In Vitro Model of Vascular Stenosis. *Microsc Microanal*. 2016;22:1766–7.

140. Yu Y, Alkhawaji A, Ding Y, Mei J. Decellularized scaffolds in regenerative medicine. *Oncotarget*. 2016;7.

141. Cartmell JS, Dunn MG. Development of cell-seeded patellar tendon allografts for anterior cruciate ligament reconstruction. *Tissue Eng*. 2004;10:1065–75.

142. Gratzer PF, Harrison RD, Woods T. Matrix alteration and not residual sodium dodecyl sulfate cytotoxicity affects the cellular repopulation of a decellularized matrix. *Tissue Eng*. 2006;12:2975–83.

143. Pu L, Wu J, Pan X, Hou Z, Zhang J, Chen W, et al. Determining the optimal protocol for preparing an acellular scaffold of tissue engineered small-diameter blood vessels. *J Biomed Mater Res - Part B Appl Biomater*. 2018;106:619–31.

144. Nazari M, Kurdi M, Heerklotz H. Classifying surfactants with respect to their effect on lipid membrane order. *Biophys J*. 2012;102:498–506.

145. Brown BN, Freund JM, Han L, Rubin JP, Reing JE, Jeffries EM, et al. Comparison of three methods for the derivation of a biologic scaffold composed of adipose tissue extracellular matrix. *Tissue Eng - Part C Methods*. 2011;17:411–21.

146. Maghsoudlou P, Totonelli G, Loukogeorgakis SP, Eaton S, De Coppi P. A decellularization methodology for the production of a natural acellular intestinal matrix. *J Vis Exp*. 2013;:1–6.

147. Tiwari A, Cheng KS, Salacinski H, Hamilton G, Seifalian AM. Improving the patency of vascular bypass grafts: The role of suture materials and surgical techniques on reducing anastomotic compliance mismatch. *Eur J Vasc Endovasc Surg*. 2003;25:287–95.

148. Ahmed E, Saleh T, Xu M. Recellularization of Native Tissue Derived Acellular Scaffolds with Mesenchymal Stem Cells. *Cells*. 2021;10:1787.

149. Liu X, Li N, Gong D, Xia C, Xu Z. Comparison of detergent-based decellularization protocols for the removal of antigenic cellular components in porcine aortic valve. *Xenotransplantation*. 2018;25:1–13.

150. Böer U, Lohrenz A, Klingenberg M, Pich A, Haverich A, Wilhelmi M. The effect of detergent-based decellularization procedures on cellular proteins and immunogenicity in equine carotid artery grafts. *Biomaterials*. 2011;32:9730–7.

151. Crapo PM, Gilbert TW, Badylak SF. An overview of tissue and whole organ decellularization processes. *Biomaterials*. 2011;32:3233–43.

152. Cebotari S, Tudorache I, Jaekel T, Hilfiker A, Dorfman S, Ternes W, et al. Detergent Decellularization of Heart Valves for Tissue Engineering: Toxicological Effects of Residual Detergents on Human Endothelial Cells. *Artif Organs*. 2010;34:206–10. doi: 10.1111/j.1525-1594.2009.00796.x.

153. Keane TJ, Swinehart IT, Badylak SF. Methods of tissue decellularization used for preparation of biologic scaffolds and in vivo relevance. *Methods*. 2015;84:25–34.

154. Xu S, Lu F, Cheng L, Li C, Zhou X, Wu Y, et al. Preparation and characterization of small-diameter decellularized scaffolds for vascular tissue engineering in an animal model. *Biomed Eng Online*. 2017;16:1–15.

155. Toshmatova M, Nakanishi S, Sugimura Y, Schmidt V, Lichtenberg A, Assmann A, et al. Influence of laminin coating on the autologous in vivo recellularization of decellularized vascular protheses. *Materials (Basel)*. 2019;12.

156. Williams C, Liao J, Joyce EM, Wang B, Leach JB, Sacks MS, et al. Altered structural and mechanical properties in decellularized rabbit carotid arteries. *Acta Biomater*. 2009;5:993–1005.

157. Schneider KH, Aigner P, Holnthoner W, Monforte X, Nürnberger S, Rünzler D, et al. Decellularized human placenta chorion matrix as a favorable source of small-diameter vascular grafts. *Acta Biomater*. 2016;29:125–34.

158. Hwang J, San BH, Turner NJ, White LJ, Faulk DM, Badylak SF, et al. Molecular assessment of collagen denaturation in decellularized tissues using a collagen hybridizing peptide. *Acta Biomater*. 2017;53:268–78.

159. Taylor MJ, Weegman BP, Baicu SC, Giwa SE. New Approaches to Cryopreservation of Cells, Tissues, and Organs. *Transfus Med Hemotherapy*. 2019;46:197–215. doi: 10.1159/000499453.

160. Chow MJ, Zhang Y. Changes in the mechanical and biochemical properties of aortic tissue due to cold storage. *J Surg Res*. 2011;171:434–42. doi: 10.1016/j.jss.2010.04.007.

161. Müller-Schweinitzer E, Ellis P. Sucrose promotes the functional activity of blood vessels after cryopreservation in DMSO-containing fetal calf serum. *Naunyn-Schmiedeberg's Achives Pharmacol*. 1992;345:594–7.

162. Starciuc T, Malfait B, Danede F, Paccou L, Guinet Y, Correia NT, et al. Trehalose or Sucrose: Which of the Two Should be Used for Stabilizing Proteins in the Solid State? A Dilemma Investigated by In Situ Micro-Raman and Dielectric Relaxation Spectroscopies During and After Freeze-Drying. *J Pharm Sci*. 2020;109:496–504. doi: 10.1016/j.xphs.2019.10.055.

163. Biggs CI, Bailey TL, Ben Graham, Stubbs C, Fayter A, Gibson MI. Polymer mimics of biomacromolecular antifreezes. *Nat Commun*. 2017;8:1–11. doi: 10.1038/s41467-017-01421-7.

164. Hasan M, Fayter AER, Gibson MI. Ice Recrystallization Inhibiting Polymers Enable Glycerol-Free Cryopreservation of Microorganisms. *Biomacromolecules*. 2018;19:3371–6. doi: 10.1021/acs.biomac.8b00660.

165. Deller RC, Pessin JE, Vatish M, Mitchell DA, Gibson MI. Enhanced non-vitreous cryopreservation of immortalized and primary cells by ice-growth inhibiting polymers. *Biomater Sci*. 2016;4:1079–84. doi: 10.1039/c6bm00129g.

166. Deller RC, Vatish M, Mitchell DA, Gibson MI. Synthetic polymers enable non-vitreous cellular cryopreservation by reducing ice crystal growth during thawing. *Nat Commun*. 2014;5:1–7. doi: 10.1038/ncomms4244.

167. Deller RC, Vatish M, Mitchell DA, Gibson MI. Glycerol-Free Cryopreservation of Red Blood Cells Enabled by Ice-Recrystallization-Inhibiting Polymers. *ACS Biomater Sci Eng*. 2015;1:789–94. doi: 10.1021/acsbiomaterials.5b00162.

168. Wang HY, Lu SS, Lun ZR. Glass transition behavior of the vitrification solutions containing propanediol, dimethyl sulfoxide and polyvinyl alcohol. *Cryobiology*. 2009;58:115–7. doi: 10.1016/j.cryobiol.2008.10.131.

169. Baboo J, Kilbride P, Delahaye M, Milne S, Fonseca F, Blanco M, et al. The Impact of Varying Cooling and Thawing Rates on the Quality of Cryopreserved Human Peripheral Blood T Cells. *Sci Rep*. 2019;9:3417. doi: 10.1038/s41598-019-39957-x.

170. Pegg DE, Wusteman MC, Boylan S. Fractures in Cryopreserved Elastic Arteries. *Cryobiology*. 1997;34:183–92. doi: 10.1006/cryo.1996.1997.

171. Solocinski J, Osgood Q, Wang M, Connolly A, Menze MA, Chakraborty N. Effect of trehalose as an additive to dimethyl sulfoxide solutions on ice formation, cellular viability, and metabolism. *Cryobiology*. 2017;75:134–43. doi: 10.1016/j.cryobiol.2017.01.001.

172. Uhrig M, Ezquer F, Ezquer M. Improving Cell Recovery : Freezing and Thawing Optimization of Induced Pluripotent Stem Cells. *Cells*. 2022;11:799. doi: 10.3390/cells11050799.

173. Pacholewicz JK, Adkins MS, Boris WJ, Gu J, Xenachis C, Klabunde RE, et al. Evaluation of cyropreserved internal thoracic artery as an alternative coronary graft : evidence for preserved functional , metabolic and structural integrity. *Eur J Cardio-Thoracic Surg*. 1996;10:20–5.

174. Amin M, Kunkel AG, Le VP, Wagenseil JE. Effect of storage duration on the mechanical behavior of mouse carotid artery. *J Biomech Eng*. 2011;133:1–6. doi: 10.1115/1.4004415.

175. Fung Y-C. Bioviscoelastic Solids. In: Biomechanics: Mechanical Properties of Living Tissues. Springer, New York, USA; 1993. p. 242–320. doi: doi.org/10.1007/978-1-4757-2257-4_7.

176. Cabrera E, Welch LC, Robinson MR, Sturgeon CM, Crow MM, Segarra A.

Cryopreservation and the Freeze – Thaw Stress Response in Yeast. *Genes (Basel)*. 2020;11:835. doi: 10.3390/genes11080835.

APPENDIX A

JOURNAL PERMISSION FOR USE OF MANUSCRIPT

Longitudinal histomechanical heterogeneity of the internal thoracic artery

Author: Colton J. Kostelnik,Kiersten J. Crouse,Wayne Carver,John F. Eberth
Publication: Journal of the Mechanical Behavior of Biomedical Materials
Publisher: Elsevier
Date: April 2021

Journal Author Rights

Please note that, as the author of this Elsevier article, you retain the right to include it in a thesis or dissertation, provided it is not published commercially. Permission is not required, but please ensure that you reference the journal as the original source. For more information on this and on your other retained rights, please visit: https://www.elsevier.com/about/our-business/policies/copyright#Author-rights

Published Journal Article

Policies for sharing published journal articles differ for subscription and gold open access articles:

Subscription articles

- If you are an author, please share a link to your article rather than the full-text. Millions of researchers have access to the formal publications on ScienceDirect ↗ , and so links will help your users to find, access, cite, and use the best available version
- If you are an author, you may also share your Published Journal Article (PJA) privately with known students or colleagues for their personal use
- Theses and dissertations which contain embedded PJAs as part of the formal submission can be posted publicly by the awarding institution with DOI links back to the formal publications on ScienceDirect ↗
- If you are affiliated with a library that subscribes to ScienceDirect ↗ you have additional private sharing rights for others' research accessed under that agreement. This includes use for classroom teaching and internal training at the institution (including use in course packs and courseware programs), and inclusion of the article for grant funding purposes
- Otherwise sharing is by agreement only
- The Published Journal Article cannot be shared publicly, for example on ResearchGate or Academia.edu ↗ , to ensure the sustainability of peer-reviewed research in journal publications.

Figure A.1 – Permission from Journal of Mechanical Behavior of Biomedical Materials to include published manuscript in this dissertation (Chapter 2).

JOHN WILEY AND SONS LICENSE
TERMS AND CONDITIONS

Oct 04, 2022

This Agreement between Mr. Colton Kostelnik ("You") and John Wiley and Sons ("John Wiley and Sons") consists of your license details and the terms and conditions provided by John Wiley and Sons and Copyright Clearance Center.

License Number	5401980551681
License date	Oct 04, 2022
Licensed Content Publisher	John Wiley and Sons
Licensed Content Publication	JOURNAL OF BIOMEDICAL MATERIALS RESEARCH PART A
Licensed Content Title	Small-diameter artery decellularization: Effects of anionic detergent concentration and treatment duration on porcine internal thoracic arteries
Licensed Content Author	Colton Kostelnik, Julia Hohn, Carlos E. Escoto-Diaz, et al
Licensed Content Date	Dec 2, 2021
Licensed Content Volume	110
Licensed Content Issue	4
Licensed Content Pages	13

Type of use	Dissertation/Thesis
Requestor type	Author of this Wiley article
Format	Electronic
Portion	Full article
Will you be translating?	No
Title	Predictions of Autograft Regional Performance and Approaches to Alleviate Graft Shortages
Institution name	University of South Carolina
Expected presentation date	Oct 2022
Order reference number	5390291307821
Requestor Location	Mr. Colton Kostelnik 3135 Monroe Street COLUMBIA, SC 29205 United States Attn: Mr. Colton Kostelnik
Publisher Tax ID	EU826007151
Total	0.00 USD

Terms and Conditions

- The materials you have requested permission to reproduce or reuse (the "Wiley Materials") are protected by copyright.
- You are hereby granted a personal, non-exclusive, non-sub licensable (on a stand-alone basis), non-transferable, worldwide, limited license to reproduce the Wiley Materials for the purpose specified in the licensing process. This license, **and any CONTENT (PDF or image file) purchased as part of your order,** is for a one-time use only and limited to any maximum distribution number specified in the license. The first instance of republication or reuse granted by this license must be completed within two years of the date of the grant of this license (although copies prepared before the end date may be distributed thereafter). The Wiley Materials shall not be used in any other manner or for any other purpose, beyond what is granted in the license. Permission is granted subject to an appropriate acknowledgement given to the author, title of the material/book/journal and the publisher. You shall also duplicate the copyright notice that appears in the Wiley publication in your use of the Wiley Material. Permission is also granted on the understanding that nowhere in the text is a previously published source acknowledged for all or part of this Wiley Material. Any third party content is expressly excluded from this permission.

Figure A.2 – Permission from Journal of Biomedical Materials Research Part B: Applied Biomaterials to include published manuscript in this dissertation (Chapter 4).